A Weckmann et al.

Review on global migration, fuel retention and modelling after TEXTOR decommission

Review on global migration, fuel retention and modelling after TEXTOR decommission

A. Weckmann
P. Petersson, M. Rubel, P. Ström
Department of Fusion Plasma Physics, KTH Royal Institute of Technology, 10044 Stockholm, Sweden

T. Kurki-Suonio, K. Särkimäki
Department of Applied Physics, Aalto University, 00076 Aalto, Finland

A. Kirschner, A. Kreter, S. Brezinsek, J. Romanzanov, P. Wienhold, A. Pospieszczyk
Forschungszentrum Jülich GmbH, Institut für Energie- und Klimaforschung – Plasmaphysik, 52425 Jülich, Germany

A. Hakola, M. Airila
VTT Technical Research Centre of Finland Ltd., 02044 VTT, Finland

ABSTRACT

Before decommissioning of the TEXTOR tokamak in 2013, the machine was conditioned with a comprehensive migration experiment where MoF_6 and $^{15}N_2$ were injected on the very last operation day. Thereafter, all plasma-facing components (PFCs) were available for extensive studies of both local and global migration of impurities – Mo, W, Inconel alloy constituents, ^{15}N, F – and fuel retention studies. Measurements were performed on 140 limiter tiles out of 864 throughout the whole machine to map global transport. One fifth of the introduced molybdenum could be found. Wherever possible, the findings are compared to results obtained previously in other machines. The review incorporates both published and unpublished results from this TEXTOR study and combines findings with analytical methods as well as modelling results from two codes, ERO and ASCOT. The main findings are:

- Both local and global molybdenum transport can be explained by toroidal plasma flow and $\vec{E} \times \vec{B}$ drift. The suggested transport scheme for molybdenum holds also for other analysed species, namely tungsten from previous experiments and medium-Z metals (Cr-Cu) introduced during various occasions.

- Analytical interpretation of several deposition profile features is possible with basic geometrical and plasma physics considerations. These are deposition profiles on the collector probe, the lower part of the inner bumper limiter, the poloidal cross-section of the inner bumper limiter, and the poloidal limiter.

- Any deposition pattern found in this TEXTOR study, including fuel retention, has neither poloidal nor toroidal symmetry.

- Fuel retention is highly inhomogeneous due to local variation of the plasma parameters – by auxiliary heating systems and impurity injection – and due to PFC temperature.

- Local modelling with ERO yields good qualitative agreement but too high local deposition efficiency.

- Global modelling with ASCOT shows high impact of radial electric field and source form on global deposition patterns, while toroidal flow has little influence. Some of the experimental findings could be reproduced. Still, qualitative differences between simulated and experimental global deposition patterns remain.

The review closes with lessons learned during this extensive TEXTOR study which might be helpful for future scientific exploitation of other tokamaks to be decommissioned.

Content

1. Introduction

For future energy production, fusion is considered a viable option due to abundant supply of raw materials needed for fusion power production, namely lithium and deuterium, and due to absence of both greenhouse gases and long-lived radioactive waste. But for fusion to be successful it must also be economically feasible. Power production increases with the volume of the fusion plasma. On the other hand, the fusion reactor itself should be as small as practically achievable for economic reasons; especially the reactor wall should be tight-fitting to the plasma to reduce material costs, e.g. for magnetic systems. This in turn would increase the interaction between the hot fusion plasma and the reactor wall, accelerating wall erosion and requiring maintenance during lengthy and expensive shut-downs. Plasma-wall interaction (PWI) is thus a key area of research within fusion plasma physics to make energy production by fusion not only possible, but also cost-efficient.

PWI is a combination of many different physical and chemical effects, varying greatly with the plasma facing material (PFM) of interest. Comprehensive literature on PWI can be found for instance in [1]. PFMs are selected mainly due to high melting point, good thermal conductivity, low erosion under plasma particle impact and chemical inertness in a hydrogen-rich environment. Behaviour under high neutron irradiation is another very important topic when considering materials to be PFMs, but is left aside in this paper because the investigated tokamak did not produce considerable amounts of neutrons during its lifetime. A comprehensive list on which qualities make a good PFM can be found for instance in [2]. No known material can fulfil the full set of requirements to become an optimal PFM. It is thus crucial to select a material whose drawbacks can be handled in a future fusion reactor. To date, the first choice for a reactor PFM is tungsten [3].

Tungsten is a high-Z material, i.e. it has a high atomic number. This results in both advantages and drawbacks. One of the major advantages is the low sputter yield of tungsten compared to lighter elements used previously as PFM, e.g. beryllium or carbon. Tungsten furthermore has a short ionisation length which is smaller than the gyro radius for singly charged tungsten in the vicinity of the wall. This leads to part-wise re-deposition of eroded tungsten back to the wall within one gyro orbit, called prompt re-deposition [4]. Both effects greatly reduce gross erosion which can be very high for lighter elements: a high sputter yield of 1% (number of sputtered particles divided by number of incoming particles) can cause gross erosion on *metre* scale in a fusion power plant [5]. Tungsten also has a low fuel retention rate, i.e. it binds only low amounts of deuterium and tritium chemically or physically, in comparison to especially carbon which forms hydrocarbons.

Drawbacks due to high atomic number are related to line radiation cooling and the shrinkage of operational space for ignition. As high-Z element tungsten cannot be fully ionised even in a 10-15 keV hot fusion plasma and is capable to radiate away substantial amounts of power – about 10% of the fusion power for a tungsten concentration of the order of 0,01% [6]. Consequently it will become ever harder to reach ignition, i.e. to heat the plasma only by the kinetic energy of the alpha particles [7]. Fusion power is reduced by the dilution effect of electrons introduced into the plasma by ionised tungsten. Furthermore, tungsten accumulates in the plasma core under certain operation conditions [8]. It is therefore of utmost economic importance for a future fusion reactor to keep once eroded tungsten out of the confined plasma region and re-deposit it back to where it came from. But where actually are high-Z impurities deposited in a fusion machine? What governs their migration to these places? And what is the substantial difference to other lighter impurities, e.g. carbon or gases injected for

plasma edge cooling?

To answer these questions numerous experiments were conducted in several tokamaks over the last decades. The most comprehensive one however was the mapping of several elements throughout a complete tokamak, i.e. the plasma-facing components (PFCs) study following the decommissioning of TEXTOR. In the following, we will describe the findings of this study concerning all elements, ranging from deuterium to tungsten, and compare them to results from other studies. We will also compare the findings to modelling on high-Z transport of eroded impurities in the plasma edge and the scrape-off layer (SOL) in TEXTOR and elsewhere. Lessons learnt from the decommissioning of a machine and the subsequent scientific exploitation will finalise the paper.

2. Experimental

In this section the machine TEXTOR is introduced where the research was carried out, followed by a description of the very last high-Z tracer experiment prior to decommissioning. We will then introduce the methods used for analysis with their advantages and shortcomings, and how the raw data was treated to retrieve the sought information. The section closes with a discussion about uncertainties.

2.1 The TEXTOR tokamak

The TEXTOR tokamak had been chosen for several reasons for this study, apart from the looming decommissioning. First, it was a machine dedicated to PWI research and offered flexible tools for transport investigation: test limiter with gas inlet [9] and monitoring spectroscopy [10], collector probe [11] [12], movable main limiters [13] and movable poloidal limiters with gas inlet. In the study described herein, the two first tools were the most important ones. A comprehensive review on PWI studies at TEXTOR can be found in [14]. The second reason to choose TEXTOR was its PFM: the tokamak was a carbon limiter machine. From the analysis point of view, carbon as PFM makes it easy to trace heavier impurities with conventional ion beam analysis (IBA) methods which were also employed in this study, and the limiter configuration results in a circular geometry of the plasma edge which suspected easier understanding of migration than in the case of shaped divertor plasmas. As will be seen later, results from the TEXTOR limiter plasma can be adapted to divertor machines, given that the plasma is quiescent.

TEXTOR was a carbon limiter machine, with a pumped belt limiter as main PFC, an inner bumper limiter, a set of poloidal limiters at top and bottom, and the possibility to insert another test limiter for exposing materials to plasma and inserting impurities in gaseous form. All these limiters will be described in detail after this general description. The machine had a major radius of 1,75 m and a minor radius usually at 0,46 m. The minor radius could be varied by positioning the main limiters in radial direction. The machine mostly operated with deuterium plasmas, and in a few cases also with protium or helium. Discharge duration was up to 8 s, with flat top duration of 5-6 s. The maximum plasma current was 800 kA [15]. Heating was possible via two neutral beam injectors (NBIs), one in co- and the other in counter-direction with respect to the usual plasma current direction. Each of the NBIs had a heating power of maximum 1,7 MW. The NBIs are described in more detail in [16] [17]. Another heating possibility was via ion cyclotron resonance heating (ICRH) by two antennae covered with stainless steel Faraday screens [18] and framed by protecting carbon limiters. An ECRH antenna was also installed, with an overall power of maximum 800 kW [19]. For glow discharge (GD) cleaning the vessel was equipped with two GD antennae. ICRH and GD antennae were mounted on a carrying torus structure called a liner, which was placed between vacuum vessel and plasma [18]. This liner was made of Inconel 625 and was insulated from the vacuum vessel. The liner served as supporting structure for ICRH antennae and main limiter. On the inner part of the torus, shielded by the inner bumper limiter, was the dynamic ergodic divertor (DED) [20]. There was furthermore a collector probe system for exposing samples to the SOL plasma [21]. The probe head could be rotated within a protective housing with aperture slits in both toroidal directions, making it possible to expose up to ten sets of samples to different plasmas without changing them manually. The set of sub-systems is shown schematically in Figure 2. A summary of machine parameters is given in Table 1.

The main PFC was a pumped belt limiter called Advanced Limiter Test Nr. 2 (ALT-II) [22]. The ALT-II limiter was sectioned in eight "blades", each equipped with a double row of 14 carbon tiles, i.e. the total number of main PFC carbon tiles was $8 \times 2 \times 14 = 224$ and the total area covered was 3,4 m². These tiles were made of isotropic graphite IG-430U except for the corner tiles (felt type carbon composite CX-2002U) [23] and mounted on an Inconel structure which was individually movable along radial direction. On the backsides of each blade there were pump ducts, in seven out of eight cases in both toroidal directions [24]. The ALT tiles were cleaned during shutdown by sand-blasting [25].

The largest PFC was the inner bumper limiter (IBL), covering the inner circumference over 120° poloidally. There were 64 tile rows in toroidal direction with 10 tiles each in poloidal

direction, yielding 640 tiles with a total area of 8,7 m². The radius of curvature in poloidal direction was 0,49 m [20], i.e. recessed from direct plasma. This detail will become important in later discussions of deposition profiles.

The poloidal limiters were situated at one toroidal position, with two arrays at top and bottom of the vessel and 2 cm behind the LCFS at the time of the experiment. Each array consisted of five "stones", semi-circular carbon bricks of 6,5 cm radius and 4,5 cm width. A gas inlet was connected to the middle top stone for gas injection. Its area was roughly 0,1 m² and hence insignificant in comparison to other limiters.

Finally, there was the possibility to insert different test limiters through a limiter lock at the vessel bottom, connected to a gas reservoir for gas injection [9] and monitored from the side by four spectroscopic systems [10]. The test limiter used in this study was a single-roof shaped graphite block, with a polished graphite collector plate on top [26].

All limiters are depicted schematically in Figure 2 while Figure 3 shows photographs of PFCs.

2.2 The MoF_6 tracer experiment

As final experiment before the decommissioning of TEXTOR a tracer experiment was conducted with MoF_6 and $^{15}N_2$ (shots no. 120964 – 121007, also including preparation and calibration shots). The aim was to create molybdenum and ^{15}N deposition patterns on the PFCs for subsequent studies when all PFCs have become available due to the decommissioning. The reason to use molybdenum instead of the actual element of interest, tungsten, was that an undetermined background of tungsten deposition from previous WF_6 injection – from a WF_6 experiment described in [27] and from spectroscopy calibration – was expected. Molybdenum background due to previous experiments with molybdenum test PFCs and due to the molybdenum concentration in the liner Inconel were deemed smaller and also more homogeneous. The reason to not use a neighbouring element of tungsten was both the small mass resolution for high-Z elements with IBA methods, as described below, and the fact that no neighbouring element can be contained in gaseous molecules at room temperature. An overview of issues related to tracer experiments and their evaluation is summarised in [28]. The discharges used were so called standard NBI discharges with 350 kA plasma current, a toroidal field of 2,25 T and 1,7 MW co-injected NBI power. Minor plasma radius was 0,46 m. Neither ICRH nor DED was used during the experiment. A discharge time line is displayed in Figure 4a.

MoF6 was injected for 1 s through the gas channel in the single-roof test limiter described

above (see also Fig. 3) during the 5 s flat-top phase of 31 discharges of 6-7 s duration. The gas injection was monitored from the side by cameras and imaging spectrometers (Acton Research Corporation, SpectraPro 500) with a filter for 395 nm to monitor FII and MoI lines at 402 nm and 390 nm, respectively. Line intensities for molybdenum and fluorine can be seen in Figure 4b.The overall amount that left the calibrated volume during these integrated 201,5 s was ca. $1,4 \cdot 10^{21}$ molecules, whereof only 40% or $5,7 \cdot 10^{20}$ molecules left the gas inlet in the vessel. This number was obtained by analysing the MoI line radiation at 390 nm and calculating the amount of injected molybdenum atoms via so called S/XB values which relate line intensity with the inward flux of atoms [29]. Signal analysis of the in-vessel pressure gauge yielded a comparable value of one third of the $1,4 \cdot 10^{21}$ molecules. It should be mentioned that such problem was not experienced with WF_6 and hence seems to be a result of the difference between MoF_6 and WF_6, most probably the higher boiling point of MoF_6. The issue is further discussed in [26].

Apart from MoF_6, also $^{15}N_2$ was injected 90° toroidally away from the test limiter. The total amount of injected nitrogen atoms was $5,3 \cdot 10^{21}$. Memory effects caused accumulation of nitrogen in the plasma and lead to two disruptions, see Figure 4c. Such memory effects were experienced before at TEXTOR [30] and also at JET [31], [32], showing that this is a common problem with nitrogen. N was hence only puffed during 22 discharges, and Helium GD cleaning was performed between every 3-5 discharges for five minutes with 300 V wall potential. The test limiter was retracted during GD cleaning. The last disruption occurred 11 shots before the end of the experiment. No memory effect could be seen for fluorine, see also Figure 4c.

After the experiment, venting and machine clearance, the first action was dust sampling as described in [33], thereafter all PFCs were dismounted and packed in plastic bags. The Inconel ALT blades were then removed for deposit scraping from backsides and neutraliser plates for later analysis. Finally, pieces from the liner were cut with a circular saw for study of this structural component as described in [34]. The PFC, liner and dust samples were then shipped to the Ångström Laboratory at Uppsala University, Sweden, for IBA studies, cataloguing and re-distribution to other laboratories.

2.3 Analysis

Most analysis was conducted with IBA at the Ångström Laboratory at Uppsala University. IBA methods were: Rutherford backscattering spectrometry (RBS), time-of-flight heavy ion elastic recoil detection analysis (ToF HIERDA, for simplicity hereafter referred to just as

ERDA), nuclear reaction analysis (NRA), and enhanced proton scattering (EPS). Electron probe micro analysis (EPMA) was conducted together with secondary ion mass spectrometry (SIMS) and EPS in RWTH Aachen University, Germany, on the catcher plate right at the gas inlet (Fig. 2e). Overall, 17% of all PFCs were examined for this study. Each of the techniques will be briefly discussed including their shortcomings with respect to the PFC analysis in this study, aiming to illustrate pitfalls for the readership.

The most widely used technique was RBS which was conducted on overall 140 tiles from ALT-II and IBL, plus further PFCs from other locations, yielding 571 points of measurement. RBS relies on the elastic backscattering of a light ion beam from a target, with both elemental composition information and depth information of the target elements encoded in the energy spectrum of the backscattered ions. Hence, in a target with many different elements, spectra become easily ambiguous and can only be interpreted with additional assumptions. We employed a $^4He^{2+}$ beam at 2 MeV hitting the target head-on, with the backscattered particles measured under 165° with a silicon detector. The maximum probing depth was around 2 μm in our case.

Evaluation was done with the SIMNRA program [35]. An example of a rather "tidy" RBS spectrum from a TEXTOR main PFC is shown in Figure 5a. Under the assumption that all elements have homogeneous depth distributions except for a surface peak or depletion, and represent all medium-Z metals by one of the heavier main constituents, nickel, identification of all elements with their substrate concentration plus their surface enrichment or depletion is straight forward.

In some cases, highly inhomogeneous elemental depth distributions make RBS spectra rather challenging for interpretation, as can be seen in Figure 5b. Another impairment results from the fact that energy resolution drops with the mass of the target elements while sensitivity rises. It is impossible to clearly discern neighbouring elements around iron, and the situation gets worse with increasing atomic number: tungsten and molybdenum as well as molybdenum and nickel are separated by mere 138 keV in the spectra (corresponding to ca. 200 nm) while carbon and oxygen are separated by 220 keV. On the other hand, sensitivity increases with atomic number squared: tungsten can be detected and quantified on ppm level while carbon amounts may only be determined to an accuracy of one or two per cent, see Figure 5c, d. This in turn means that heavy impurities deposited on light PFCs are very easy to detect and quantify with RBS.

Another important IBA method, complementary to RBS, is ERDA. The system used for the measurements in this study changed within the investigation period. Most measurements were conducted with the system described in [36], whereas an improved system described in [37] became only available in the last parts of the study. Both systems feature a ToF arrangement and hence the term ERDA is used here for convenience, meaning actually ToF ERDA. For the first system, core drilling from PFCs was necessary to obtain mountable samples, which reduced the amount of measurements conducted with ERDA due to sample preparation efforts.

In any case the principle is as follows: a (heavy) ion beam impacts under a shallow angle on the target and generates recoils from the target which then get forward-scattered into an arrangement consisting of a time-of-flight tube and an energy detector at the very end. With ERDA one is hence capable to obtain two pieces of information, velocity and kinetic energy, which can be converted into separate spectra for each element. The elemental separation for light species is extraordinary and can be used to separate different isotopes, e.g. ^{14}N from atmosphere and ^{15}N mainly from tracer experiments, up to fluorine. But as for RBS, the mass resolution rapidly drops with mass. An exemplary spectrum is shown in Figure 6.

For our measurements, an ^{127}I^{8+} beam at 36 MeV was used, with the angle between beam and target surface being 22,5° and the angle between detector and beam being 135°. The advantage of using a heavy ion beam is an increased efficiency in detecting heavy tracer elements in the sample, at the cost of reduced penetration depth. The probed depth in our case hardly exceeded 600 nm even for samples composed of mostly light elements (C, B, O). Analysis was conducted with the in-house Matlab program CONTES. The shallow angle incidence makes ERDA notoriously susceptible to surface roughness, and hence comparisons with concentrations obtained with ERDA and RBS were necessary. Details about this comparison will be given in Section 4.

With RBS one cannot probe deuterium with a helium beam, and under the heavy ion beam of ERDA hydrogen species get de-trapped from the sample within seconds [38], sabotaging accurate quantification without taking the time dependence of count rates into account. Nuclear Reaction Analysis (NRA) can be easily used instead. Here, a ^{3}He beam at 2,8 MeV was used to trigger the reaction D(^{3}He,p)^{4}He where the protons were detected with a solid state detector. Evaluation was conducted with SIMNRA. An example from a carbon PFC with deuterium is shown in Figure 7a. The spectrum contains the typical RBS steps on the low energy side, but in general the nuclear reaction peaks of ^{12}C(^{3}He,p)^{14}N with different excitation steps and of D(^{3}He,p)^{4}He dominate the spectrum. Care must be taken whenever

higher amounts of boron, ca. 20% or more, are in the sample together with low amounts of deuterium, ca. 1% or less. In that case the $^{11}B(^{3}He, p)^{13}C$ reaction may introduce non-negligible count rates within the region of interest for deuterium counts, see Fig. 7b. Such overlap was common for NRA spectra of TEXTOR samples from high-heat flux (HHF) regions where deuterium amounts were low but boron content from boronisation still could be as high as 40%. Fortunately, when boron of natural isotopic mix is used for boronisation one can easily discriminate deuterium and boron counts by fitting the $^{10}B(^{3}He, p)^{12}C$ peak that already lies beyond the region accessible by deuterium counts for a 2,8 MeV beam (also Fig. 7b). Care must be taken when natural isotopic ratios of boron cannot be assumed. Apart from that, NRA is suitable to obtain deuterium depth profiles down to 10 µm in carbon samples.

The polished carbon catcher plate (see Fig. 2e and 3a, first from the left) with roughness of 0,1 µm was treated with a different set of analysis methods. It was initially clean and only exposed to plasma in the experiment described above.

Since it should document local deposition profiles, a dense mapping was required, which called for electron beam methods. Here, EPMA was employed to measure concentrations of B, N, O, F, Ti and Mo with one point of measurement every 2 mm. Titanium was used on catcher plates at the sides of the test limiter. EPMA measurements were conducted at the technical university RWTH Aachen, Germany, with a 15 keV electron beam using wavelength dispersive spectroscopy. Close to the gas inlet (ca. 1 cm) the re-deposited film was too thick to be penetrated by the electron beam even at 30 keV. The film thickness was thus probed with SIMS at two different positions, yielding a deposited layer of up to 6 µm thickness which built up during the 31 tracer injections. SIMS is not quantitative for films with *a priori* unknown properties and cannot be employed to assess the overall amount of deposited elements, which was crucial for molybdenum. Therefore EPS at Ångström laboratory was used to quantify at least the molybdenum amount. An EPS beam consist protons of MeV range, i.e. the principle is the same as for RBS – only that for EPS the scattering from lighter elements is not elastic anymore. In our case, protons at 2 MeV were used which increases the depth range to ca. 15 µm instead of about 2 µm with ^{4}He RBS. The disadvantage is a greatly reduced energy resolution, which makes it only possible to separate light from heavy elements. EPS was thus solely used to quantify molybdenum as only heavy element on the catcher plate. The method is hence not suitable for analysis of long term samples exposed to a mixed element environment, such as normal PFCs in tokamaks, especially when depth profiles are of interest.

2.4 Uncertainties and data treatment

Uncertainties for the IBA methods described above are a combination of three effects: uncertainties in the beam current integrator whose signal is needed to ascribe the integrated amount of beam particles impinging on the sample (10% relative), uncertainties in cross-sections for the respective interactions between beam and sample atoms (around 10% relative), and statistical uncertainties (around 6%). For RBS the signal overlaps from different elements creates some ambiguity in analysis. For ERDA ambiguity arises due to roughness, and due to noise which inflicts especially trace elements with low counting rate. In both cases the error may be as high as 20% relative. Quantification can thus be trusted within $\pm 25\%$ with ERDA and RBS on ALT-II and IBL tiles. Details about surface roughness of both ALT-II and IBL tiles can be found in Figure 4 in [25]. On the test limiter with smoother surface and less impurities the ambiguity drops significantly, leaving a total uncertainty of $\pm 15 - 20\%$ for molybdenum and tungsten, respectively, for the applied IBA methods.

SIMS is not quantifiable in this study. The only error here may be attributed to the layer depth that was found with SIMS. The SIMS crater was analysed with stylus profilometry which showed inhomogeneous sputtering with height variations at the crater bottom of approximately $\pm 0,5$ μm [26].

EPMA can quantify elements with about 5% uncertainty, plus another maximum 15% due to surface roughness. In total this yields $\pm 16\%$ uncertainty for the quantification with EPMA on the graphite collector plate from the test limiter.

RBS offers advantages where ToF ERDA has disadvantages and vice versa. Hence, areal concentrations of molybdenum at same positions were compared with the two methods and yielded good agreement within the error bars. In total, the ToF ERDA results seemed to be always a bit higher than RBS. This effect was attributed to roughness and confirmed with a little roughness study of gold deposited on silicon with various roughnesses: the higher the surface roughness, the higher the measured gold concentration with ERDA, although the values measured with RBS stay constant. Hence increased sample roughness causes increased measured concentrations of heavy species for ERDA.

Adequate data visualisation was crucial in this study to understand impurity transport patterns. Interpolation was used to cast the vast and confusing amount of data points into a rather

intuitive deposition map. For interpolation radial basis functions (RBFs) were used. RBFs can approach any function $y(\vec{x})$ through sums of a certain type of function f(r) where

$$y(\vec{x}) = \sum_{i=1}^{n} w_i \cdot f(r = \|\vec{x} - \vec{x}_i\|) \quad (1)$$

with w_i being a pre-factor (weight) and $\|\cdot\|$ is a norm, usually Euclidean [39]. In this case $f(r) = r$ was used, i.e. a linear RBF, as simplest adequate function.

The deviation of $y(\vec{x})$ from measured data further away from the point of injection is within the error bars of the measured values, while close to the injection the measured areal concentration scatters very strongly. Figure 8a illustrates this point. The scatter is definitely not an artefact of the employed IBA method or the spectra evaluation but resembles how strongly tracer amounts can vary on small scale. While the cause is discussed further in Section 3, for now it is important to note that these small scale variations near the source are not accounted for in the interpolation for the following reason. $y(\vec{x})$ can be made either very accurate so that it goes exactly through every measured point, i.e. in Formula (1) n equals the amount of data points, or it can be made smooth, i.e. n is (much) smaller than the amount of data points which yields a more steady appearance at the cost of decreased accuracy, as can be seen by comparing Figure 8a (higher n) to 8b (lower n). However, reducing the smoothness below a certain value will cause the interpolation to have sharper spikes, some of which will cross zero and imply *negative* areal concentrations. Interpolations matching the data points as much as possible will hence produce unphysical features. On the other hand, the large deviation of the interpolated curves from measured values especially in regions of high deposition renders the curves inadequate for any quantification. The maps obtained from interpolation are thus used for qualitative discussion only while all quantitative analysis is founded on the actual measured concentrations.

Discussion of results and physical interpretation in the subsequent sections is often done with the aid of fitted functions to the measured data. Fitting was performed with the Python package SciPy where the fitting routine employs least square calculation for finding the optimal fit. For reasons discussed above, calculating deviations of fits from measured values are of no added value and will not be treated further.

2.5 Expected species

TEXTOR was mainly operated with deuterium and hence fuel retention is measured in the amount of deuterium in the samples. The main PFCs were made out of carbon. The machine

itself was wall-conditioned with deuterium and helium GD cleaning, and boronisation as well as siliconisation. Furthermore the liner and the ALT-II blade structure was made of Inconel 625 with composition given in Table 2. The ICRH antennae were covered with stainless steel Faraday shields. The NBI systems had beam scrapers made of water cooled copper plates. On top of that, despite GD cleaning usual impurities in vacuum systems are oxygen and hydrogen from water and residual air. These are the so-called "intrinsic" elements since they are introduced into the vessel by normal operation and maintenance. During experiments, many more elements and isotopes were introduced into TEXTOR over the course of years and decades. Table 3 lists all species together with their origin and further reading. We forestall also in this table whether the elements or isotopes have in fact been found with IBA. Apparently, most of the listed elements and isotopes are traceable, in many cases with hints or even clear links to their point of origin. This is both a good and a bad message concerning impurity transport experiments: we are able to link the place of deposition to the origin for heavier elements (around iron and heavier) years after their introduction which encourages scientific exploitation of other tokamaks' decommissioning; on the other hand, even lighter elements stay long in the vessel and make tracer experiments increasingly difficult as the "background" of leftover species gradually increases. In Section 4 it will become clearer how one can treat such background in the case of molybdenum, and how long residence times of elements in tokamaks can be turned to an advantage to develop and verify transport models.

Part I – experimental results of TEXTOR decommissioning

3. Tracer injection and local deposition

The injection of MoF_6 took place in the line-of-sight for the horizontal observation system described in [10]. Two valuable pieces of information were obtained from the recorded data: (i) the amount of overall injected MoF_6 as described previously, (ii) the radial distribution of molybdenum from the MoI line radiation. Figure 10a shows the MoI line radiation during MoF_6 injection through the test limiter, Figure 10b the cumulated intensity during one shot (no. 120975) over radius at one lateral position. It can be described adequately by a Cauchy distribution [40]

$$C(r) = A \cdot \frac{s^2}{s^2 + (r - r_0)^2} \qquad (2)$$

with 2s as full-width-half-maximum (FWHM) and r_0 as centre. A Gaussian distribution yields less satisfactory agreement. This can be understood when the gas is assumed to not form a directed jet normal to the inlet, but rather to expand isotropically. In such a case the amount of gas molecules per angle is constant and it follows for a projection on a radial line according to Figure 10c:

$$\frac{dn}{d\varphi} = const. \implies \frac{dn}{dr} = \frac{dn}{d\varphi} \cdot \frac{d\varphi}{dr} = const. \frac{s^2}{s^2 + (r-r_0)^2} \qquad \text{with } \varphi = \arctan\left(\frac{r-r_0}{s}\right).$$

Fitting parameters for the curve in Fig. 10b are: $s = 6,3\ mm$, $r_0 = 483\ mm$. The fit has been obtained directly at the lateral position of the gas inlet in Fig. 10a which shows that s in reality does not only depend on the distance of projection as implied by Fig. 10c. The maximum of MoI light by experimental values is a bit closer to the gas inlet, at $r_0 = 485\ mm$. When looking in *toroidal* direction (horizontally in Fig. 10a) 6 mm above the inlet (i.e. 12 mm below the limiter tip, or $r = 48,7\ cm$), which is roughly at the position of highest intensity, the MoI light distribution is best described by a Cauchy distribution ($s = 5,2\ mm$, $x_0 = -10\ mm$ w.r.t. the inlet) times an exponential function with 7 cm e-folding length.

Local deposition of different elements is shown in Fig. 11, together with the obtained layer thickness. The plots are based on EPMA data, combined with EPS data in the case of molybdenum. It immediately becomes apparent that most deposition takes place around the gas inlet, with molybdenum as main constituent (please note the colour bar in $10^{18} cm^{-2}$ instead of $10^{16} cm^{-2}$ for all other elements). Although only MoF_6 was injected at the indicated position in Fig. 11 (arrow), also nitrogen and oxygen could be found. Nitrogen deposition exhibits a similar pattern to molybdenum and the deposition thickness. It was most probably deposited during the discharge along with molybdenum. ERDA analysis close to the gas inlet however shows that ^{15}N/([15]N+[14]N) is below 10%, i.e. most nitrogen is not from the simultaneous ^{15}N tracer injection but in fact ^{14}N, most probably from earlier experiments and residual air in TEXTOR. Oxygen has a very high concentration only at the gas inlet itself. Titanium was mounted on the side of the test limiter as catcher plates but was only deposited in minuscule amounts on the collector plate, without any correlation to the other elements. 6% of the injected molybdenum amount was deposited locally on the collector plate.

Now the focus is on the molybdenum pattern. It has been mentioned previously that the MoI line emission in the radial, and to some extend also in the toroidal direction follows a Cauchy distribution. Notably the deposited amount of molybdenum also exhibits a Cauchy distribution, both in toroidal and poloidal direction. Fits to the EPS data are displayed in Fig.

12. As with the MoI line, the fit in toroidal direction is better for $C(x) \cdot e^{-x/\lambda}$ while in poloidal direction an unmodified Cauchy distribution suffices. Fit parameters are: $s = 4,6\ mm$, $x_0 = -0,2\ mm$, $\lambda = 15\ mm$ (toroidally) and $s = 3,9\ mm$, $y_0 = -0,2\ mm$ (poloidally). In both cases there is only a negligible constant offset of about 10^{-3} of the peak value. As can be seen from Fig. 11, the molybdenum deposition is elongated towards the upper right corner, i.e. towards the high-field side (HFS, upwards in Fig. 11) and in the direction of the plasma current (to the right in Fig. 11). Such a pattern has been recorded also for methane [41] and silane injection experiments [42] as well as for tungsten [27] (for tungsten more details below). The elongation deviates almost exactly $45°$ from the toroidal direction in Fig. 11. Taking the test limiter inclination of $20°$ into account the real value is $48°$. Hence the movement of the molybdenum atoms is equally strong in toroidal and poloidal direction. This movement cannot be explained by the magnetic field direction alone. In [41] and [42] the elongation is explained by combined SOL flow in toroidal direction and $\vec{E} \times \vec{B}$ drift in poloidal direction due to a radial electric field. For various plasma scenarios the toroidal velocity of the plasma at the LCFS is in the order of a few km/s [43], [44], [45] (without DED). The poloidal velocity of the plasma in the SOL is also around a few km/s for different scenarios, with a flow reversal at or slightly inside the LCFS [44], [45], [46] for using co NBI. More detailed information cannot be provided, considering error bars given in the publications – $\pm 5\ km/s$ toroidally and $\pm 0,7\ km/s$ poloidally [44] – and the fact that only one of the aforementioned sources (the oldest one: [43]) supplies data from the same plasma scenario. In any case all sources agree that toroidal and poloidal velocities of measured impurities are within the same order of magnitude, which is in line with the deposition profile seen in Fig. 11 for molybdenum. One cannot exclude the role of movement along field lines, i.e. in the direction of $-\vec{B}$ (to the right in Fig. 11), but this movement would also be in the order of 1 km/s for molybdenum atoms with a few eV of kinetic energy from dissociation and collisions.

There is a qualitative correlation between injected and deposited molybdenum, as can be seen from a SIMS depth profile measured 2 mm away from the gas inlet, Figure 13. The maxima in the molybdenum depth profile correspond to enhanced injection quantities, as measured by the pressure gauge at the calibrated volume of the injection system. Similar depth profiles were only found on a few other PFCs with high molybdenum concentration and less clear correlation. In all other cases the deposited layers were too thin in order to be resolved and one may assume a more or less homogeneous deposition profile further away from the impurity source, except for an eventual surface peak.

Evaluating data from a previous experiment with WF_6 [27] shows a Cauchy distribution of the deposited tungsten as well, see Figure 14. A Gaussian fit is displayed for comparison, proving that a Cauchy distribution fits the data better. The spread s is larger than for molybdenum, with $s = 7,7\ mm$. The typical elongation in the direction of plasma current and HFS was also observed, see Fig. 2 in [27], though with higher elongation in the poloidal direction than for molybdenum. The local deposition efficiency for tungsten was 1-3% [27] and hence smaller than for molybdenum.

It was previously mentioned that only about 40% of MoF_6 released from the calibrated volume eventually reached the vessel. We assumed a substantial part of the tracer gas could have decomposed in the inlet system. Therefore the test limiter was sawn up and RBS measurements were conducted along the injection channels. Both molybdenum and tungsten from MoF_6 and WF_6 injections could be detected, but only in negligible amounts. Details of the test limiter analysis are given in [26]. The rest of the inlet system was not available for analysis.

In summary, the injection of MoF_6 greatly influences the local molybdenum deposition pattern, which follows a Cauchy distribution. This has also been found for tungsten after WF_6 injection. In both cases the absolute deposition efficiency is small, only a few per cent. As will be seen in the next section, the local deposition compared to the global deposition is nevertheless substantial. Nitrogen is deposited alongside molybdenum while oxygen and fluorine are found directly at the gas inlet. The overall deposition pattern is determined by the $\vec{E} \times \vec{B}$ drift, SOL flow and possibly movement along field lines in the direction of $-\vec{B}$. Comparison with methane and silane injection shows that lighter elements tend to be more deflected in toroidal direction while heavier elements follow more the $\vec{E} \times \vec{B}$ drift, with molybdenum right in between.

4. Global transport of heavy impurities

This section focuses on the global deposition patterns of molybdenum, tungsten and medium-Z metals, all obtained from the very same RBS measurements in TEXTOR. First, molybdenum on the different PFCs will be quantified to obtain an overall material balance. The interpolated molybdenum deposition pattern will then be used to develop a transport scheme, building on the knowledge from the previous section. For later comparison with other

machines, functions will be fitted to the toroidal deposition pattern on various poloidal positions. We will also devote a few paragraphs to analytical treatment of some found deposition patterns. The transport scheme for molybdenum is then applied to the other species tungsten and medium-Z metals in TEXTOR. We finally compare the findings with global transport experiment results from other machines.

4.1 Molybdenum

Molybdenum, tungsten and medium-Z metals (chromium to copper) where measured with RBS at 571 points on plasma-facing surfaces of PFCs throughout the whole machine, see Figure 15a, with at least 3 points of measurement on each tile. For molybdenum, some points were cross-checked with ERDA for quantification. The focus is first on molybdenum. The deposited molybdenum was quantified in the following way. First we assumed a certain deposition rate to extrapolate the molybdenum found with RBS in the first 200 nm to the depth associated with the overall deposition from the experiment. This deposition rate had been measured on the ALT-II limiter to be 1-3 nm/s in previous experiments [47], [48]. Due to lack of data, the same rate was assumed also for the IBL. Then the background molybdenum concentration resulting from the liner and previous experiments involving molybdenum was subtracted. The background level was assessed from RBS and ERDA measurements on tiles dismounted from TEXTOR in 2011 (3 tiles for ALT-II, 3 tiles from IBL) and yielded a concentration of $0,8 \cdot 10^{15} \ cm^{-2}$ on the ALT-II limiter and $0,6 \cdot 10^{15} \ cm^{-2}$ on the IBL. The background subtracted RBS results were cross-checked with ERDA (also background subtracted) for 32 positions, yielding agreement within the error bars. Finally the areal concentrations were multiplied with the respective PFC areas. The results are:

1) The ALT-II limiter harbours 1-2% of the injected molybdenum on the plasma-facing sides according to RBS, and 2% according to ERDA. Deposition on the ALT-II tile backsides yields additional 0,4% of molybdenum, whereof more than half was deposited on the four corner tile backsides next to the injection point. Deposition on ALT-II backsides will be addressed again in Section 9 about global modelling.

2) On the IBL 7-10% of injected molybdenum got deposited according to RBS, and 11% according to ERDA.

3) Measurements on the poloidal limiter yields maximum 1% of the injected molybdenum (assuming 3 nm/s deposition rate). Measurements have only been

performed with RBS due to very rough, flaky deposits and unfavourable sample geometry.

4) Contributions from collector probe, the liner [34] and PFC sides are negligible.

With the locally found 6% [26], only 20% $\pm$ 5% of the injected molybdenum could be found after analysing 140 tiles from ALT-II and IBL (including tile sides close to the injection, and backsides of selected ALT-II tiles), 6 "stones" from the poloidal limiter (both top and bottom, either toroidal side) and the collector plate on the test limiter. An attempt was made to measure molybdenum in the dust from the neutraliser plates in the ALT-II pump ducts through which the vessel is pumped under operation. This measurement was conducted with PIXE because it is the IBA method available at Ångström with least dependence on sample geometry for proper analysis. Analysis of the neutraliser plate dust yields molybdenum and Inconel components in the ratio 1:20, i.e. the same ratio as in Inconel alloy. However, it may be questionable that the MoF_6 injection could cause a detectable increase of molybdenum against the continuous background level from the liner erosion at all.

In the following, details in deposition maxima positions and deposited amounts are used to elaborate a transport scheme. The global molybdenum deposition profile peaks at three positions, all roughly at the same toroidal position as the inlet, see Figure 15b. These positions are the ALT-II tiles next to the gas inlet in the direction of the plasma current, the lower part of the IBL, and the upper part of the IBL. The concentration is highest near to the test limiter, i.e. the molybdenum did not migrate a full poloidal circumference in order to get deposited. Instead we remember the discussion of the poloidal velocity and the flow reversal around the LCFS from Section 3, and combine it with the knowledge about the injection. To first approximation, the MoI line radiation resembles the radial molybdenum distribution above the test limiter after injection. We further assume the $\vec{E} \times \vec{B}$ drift to push all the molybdenum below the LCFS towards the HFS, just as has been seen on the collector plate, Fig. 11. At around the LCFS at $r = 46 \; cm$ the flow reversal takes place and the molybdenum is now swept to the ALT-II limiter. With the velocity ratio $\frac{v_{pol}}{v_{tor}} \sim 1$ (see discussion of the molybdenum pattern, Section 3) one would also expect the ratio of transport distances in poloidal and toroidal direction $\frac{\Delta d_{pol}}{\Delta d_{tor}} \sim 1$ for the molybdenum concentration peak positions on ALT-II and IBL bottom. For the IBL this is indeed the case $-\frac{25cm}{21cm} \sim 1$ – while for the ALT-II the poloidal to toroidal distance from the test limiter is $\frac{25cm}{3cm} \sim 8$. This latter disagreement can be explained by poloidal velocity variation: according to modelling in [49] poloidal velocity

in TEXTOR was higher at the poloidal position of ALT-II than at the IBL bottom (for $r = 46\ cm$), hence one would expect $\frac{\Delta d_{pol}}{\Delta d_{tor}} > 1$ which is the case here.

Apart from the difference in position of molybdenum concentration peaks on ALT-II and IBL, we must also explain the difference in molybdenum amount on ALT-II and IBL: between $\frac{7\%}{2\%} = 3,5$ to $\frac{11\%}{1\%} = 11$ times more on IBL than on ALT-II. This difference can be explained by the radial molybdenum distribution at the injection location, using radial MoI line radiation profile as rough estimate of the radial molybdenum distribution. The cumulative MoI light intensity below the LCFS is 6,5 times the cumulative MoI light intensity above the LCFS which falls comfortably within the aforementioned range. Hence, the two strong molybdenum deposition peaks at IBL bottom and on ALT-II can be explained by flow reversal. Additionally, the difference in deposited amounts on ALT-II and IBL can be explained by radial molybdenum distribution. The third peak at the IBL top has $\frac{\Delta d_{pol}}{\Delta d_{tor}} = \frac{0,6m}{1,28m} \approx 0,5$ which is still feasible with $\frac{v_{pol}}{v_{tor}} \sim 1$, keeping the aforementioned high uncertainties of velocity measurements in mind. The third peak can either result from re-eroded molybdenum from ALT-II or the IBL bottom, or is formed by residual molybdenum which passed these two places without being deposited at all. Figure 16 depicts all information merged into one transport scheme.

- After injection at the test limiter, point (0) in Fig. 16, the MoF_6 decomposes and the excited molybdenum first radiates MoI line radiation, giving us a coarse hint on the radial molybdenum distribution above the inlet.

- The part of the distribution below the LCFS follows the $\vec{E} \times \vec{B}$ drift direction at that radial position, namely clockwise when seen in the direction of the plasma current. This motion creates a local deposition profile tilted towards the HFS in Fig. 11. It also leads to the molybdenum concentration peak on the IBL bottom, point (1).

- Within the flow reversal region, i.e. within the LCFS, the $\vec{E} \times \vec{B}$ drift points in counter-clockwise direction and takes the tail of the radially Cauchy distributed molybdenum towards the ALT-II limiter, point (2). Since much less molybdenum has made it across the LCFS there is less molybdenum on the ALT-II limiter than on the IBL.

- Some molybdenum may not hit the PFCs at points (1) or (2), or gets re-eroded from there, continuing along the $\vec{E} \times \vec{B}$ drift direction either inside or outside the LCFS and settling at the IBL top, point (3).

- In toroidal direction the concentration peaks are shifted slightly by toroidal plasma and SOL flow induced by the co-NBI. The peak shifts depend on poloidal position since the plasma velocity ratio $\frac{v_{pol}}{v_{tor}}$ also depends on poloidal position. The deposition profiles decay in toroidal direction roughly exponentially, with e-folding lengths summarised in Table 4 [50]. This effect may be due to re-erosion – re-deposition steps as suggested in [4], due to radial diffusion across magnetic field lines, or both. The latter process is examined and discussed further with the ERO code in section 8. Either way, a significant broadening with e-folding lengths up to a metre has been reached after only 31 shots for molybdenum.

It will be seen later that the transport scheme sketched above can be also applied to other impurities, namely tungsten and medium-Z metals. But first we will examine four positions in more detail in the attempt to understand the molybdenum deposition patterns analytically. These four positions are: the collector probe, the IBL bottom, the IBL poloidal cross-section at the gas inlet, and the poloidal limiters.

4.1.1 Collector probe

The deposition profile on the collector probe head is the easiest one to understand. Its position is schematically depicted in Fig. 2a. Deposition took place on a range of $r = 49,5\ cm$ to $r = 54\ cm$. Exposures were either during a 1s time window of a discharge, usually around 0,5 – 1,5 s, or for a substantial part of the flat-top phase, up to 3,5 s. Deposition on the collector probe tiles were used to determine the radial molybdenum distribution in the SOL. Unfortunately only two sets of samples, one in co- and one in counter-direction, captured enough molybdenum for subsequent analysis. Hence, at least several seconds of exposure were necessary to yield amounts traceable for RBS with a sensitivity of only a few tens of ppm for molybdenum on carbon. Both sides showed an exponential decay of molybdenum concentration as one would expect for a SOL particle source with $r < 49,5\ cm$. The decay on the side facing the plasma current (and hence the SOL flow) had an e-folding length $\lambda = 11\ mm$ and had a higher concentration of molybdenum, while the side facing away from the plasma current had an e-folding length $\lambda = 29\ mm$ and about five times less molybdenum. As we have seen on the collector plate the molybdenum moved with the SOL flow and consequently $\lambda = 11\ mm$ will be assumed throughout the rest of the paper.

4.1.2 IBL bottom

Secondly, we will focus on the IBL bottom next to the test limiter, as can be seen in Fig. 2d. The idea that the $\vec{E} \times \vec{B}$ drift carried the centre part of the Cauchy distribution from the inlet towards the HFS sparked a question: could it then be possible to find a Cauchy distribution on the bottom of the IBL? We indeed found a – slightly distorted – Cauchy distribution also in radial direction at the very bottom of the IBL. First, let us look at the geometry of the plasma with respect to the IBL, see Figure 17a. Impurities move in poloidal direction with respect to the plasma centre ⊕, while the geometry we use for plotting follows the machine layout, and its centre ⊗ is likely to be off-set with respect to the plasma centre. The result is the following: as an impurity moves in poloidal direction at constant distance to the LCFS, the IBL comes closer and closer, has maximum proximity with the LCFS at the inner mid-plane and then recedes again. By basic geometry, that is the cosine rule and $\cos(180° - \vartheta) = -\cos(\vartheta)$, and considering Fig. 17a one can express the radial position $r(\vartheta)$ of the IBL surface with respect to the plasma centre as:

$$r(\vartheta) = \sqrt{\Delta^2 + b^2 + 2b\Delta \cdot \cos(\vartheta)} \qquad (3)$$

with b as IBL curvature radius and Δ as distance between the IBL curvature centre and the plasma centre, ⊗ and ⊕, respectively. ϑ starts at the outer mid-plane and continues in counter-clockwise direction as seen in the plasma current direction. Equation (3) also applies for plasma shifts away from the IBL, i.e. negative Δ. The offset of the plasma centre during this experiment varied during a discharge according to EFIT: $\Delta \sim \pm 4\ cm$. Although it is difficult to guess from the data at hand which value Δ predominantly took, one can say with certainty that it is not zero, see next sub-section. Fits in the next subsection suggest |Δ| being mainly between 2 and 3 cm.

We examined the lower side of the bottom tile along radial direction, yellow stars in Figure 18, which had much higher molybdenum concentration than the plasma-facing sides. The poloidal positions from the other examined tile fronts above (green stars in Fig. 18) were translated into radii with the help of Equation (3) in order to combine them with the measurements from the lower side of the bottom tile. The best fit to the measured data could be obtained by a distorted Cauchy distribution, i.e. multiplied by an exponential decay with $\lambda \approx 10\ mm$, see Fig. 18 red curve. Without this modification the best fit does not match in the tails of the function, see Fig. 18 blue curve.

4.1.3 IBL poloidal cross-section

If the centres of the plasma column and the IBL curvature do not coincide, i.e. $\Delta \neq 0$, the areal molybdenum concentration must vary with the poloidal angle. We know from Fig. 12b that this must be the case at the toroidal position of the test limiter, but it is also true for all other measured poloidal cross sections on the IBL.

We begin with the areal concentration as function of the intersection angle α between a circular trajectory of an impurity at $r(\vartheta)$ and the IBL surface. The intersection angle can be expressed by the cosine rule regardless of the sign of Δ, as shown in Fig. 17b and c. Knowing that the flux to an area depends on $\sin(\alpha)$ and using $\sin(\arccos(x)) = \sqrt{1 - x^2}$, one obtains:

$$\sin(\alpha) = \sqrt{1 - \left(\frac{b^2 + r(\vartheta)^2 - \Delta^2}{2br(\vartheta)}\right)^2}. \qquad (4)$$

With a function f(r) describing the radial molybdenum concentration in the SOL, the areal molybdenum concentration on the IBL in poloidal direction should be:

$$Mo(\vartheta) = Mo_0 \cdot \sin(\alpha) \cdot f\big(r(\vartheta)\big) \qquad (5)$$

with Mo_0 being a constant, f(r) a radial distribution function describing radial molybdenum distribution in the plasma edge, and r as function of ϑ. Figure 19a shows that for f(r) a Cauchy, e.g. as seen at the injection position, and an exponential function, e.g. as seen with the collector probe, one obtains comparable patterns. Depending on Δ the molybdenum concentration should either resemble a "double-hump" or a "funnel", depending on whether Δ is positive or negative, see Fig. 19b. A similar case is discussed in [51], section 25.2. Both shapes are observed in the five evaluated poloidal cross-sections: the "funnel" appears in four positions to varying degrees, the "double-hump" is observed once – toroidally on the far side of TEXTOR with respect to the gas inlet.

We will still stay at the IBL tile column at the toroidal position of the test limiter, with the focus on the plasma-facing tile sides. A comparison of $Mo(\vartheta)$ with actual values can be seen in Figure 20 for $\Delta = 2\ cm$ and $f(r) = C(r)$ (blue curve). Due to the sheath potential an impact angle smaller than ca. $1°$ is unrealistic, and setting the minimum angle to $1°$ yields the red curve in Fig. 20. $f(r) = exp(\frac{r - r_0}{\lambda})$ performs equally well (green curve). The large scatter of data comes from measurement at different positions on one tile. Obviously, not only on ALT-II the molybdenum concentration exhibits local variation.

4.1.4 Poloidal limiters

Finally, let us look at the poloidal limiters which are displayed in Fig. 2b and positioned 45° toroidally away from the test limiter. Due to their semi-circular shape, the impact angle is again a function of radius. Figure 21a displays the geometry which in combination with a radial distribution function f(r) yields the molybdenum concentration as a function of radius:

$$Mo(r) = Mo_{r0} \cdot \sqrt{1 + \left(\frac{a + \kappa - r}{\kappa}\right)^2} \cdot f(r). \quad (6)$$

$\kappa = 6,5\ cm$ is the radius of poloidal limiter curvature, a=48 cm is the radial position of the limiter tip, and Mo_{r0} is the concentration for $\alpha = 90°$. Six poloidal limiter stones were measured on both sides facing co- and counter-direction with respect to the plasma current. Each stone showed a different radial pattern with co-counter asymmetry. However, the asymmetries of all stones combined did not have a clear preference towards co- or counter-direction, i.e. there is no clear co- or counter deposition pattern. Figure 21b shows data from all stones, resembling the surface concentration of molybdenum (negative values indicate lower surface concentration than background concentration) and fits of Equation (6) with exponential (blue) and Cauchy distribution (red) as f(r). The latter has better agreement with the data. Because of the large scatter due to very rough surface and local concentration fluctuation, the agreement is only qualitative.

The attempt to analytically treat deposition patterns – in our case: collector probe, IBL bottom, IBL poloidal cross-section at the gas inlet, and poloidal limiters – requires varying effort. Only the collector probe deposition pattern showing exponential decay is clearly understandable without close consideration of the PFC geometry. Analytical treatment of semi-circular poloidal limiters is straightforward but the obtained data is very scattered because of flaking deposits. The other two cases dealing with the IBL yield better agreement between analytical expressions derived from PFC geometry and measured data. *A priori* assumptions about exponential decays and undetermined plasma shifts Δ leave some room for discussion. Yet we have been able to derive local and global transport schemes for molybdenum in accordance both with detailed analytical treatment and with the given literature.

In the following, the transport scheme will be tried on tungsten and medium-Z metals and then compared to observations in other machines.

4.2 Tungsten

Tungsten concentration was measured at the positions indicated in Fig. 15a. No attempt was made to quantify the amounts of tungsten and hence the unit to express concentration is given in parts per million, ppm, relative to other surface constituents. The deposition pattern interpolated from the measured values is displayed in Figure 22. Strongest peaks appear on the IBL top and bottom close to the poloidal limiter. We will first focus on this area.

Table 3 and Fig. 9 reveal that most of the tungsten had been introduced by experiments where a poloidal limiter coated with 0,5 mm of tungsten had been exposed to edge plasma or even acted as main limiters [52] for several hundred discharges. Their radial position had varied between a rest position 3 cm behind the LCFS (r=49 cm, > 1000 discharges) and immersion in the plasma (r=42 cm) for 1,7 s. A subset of limiter stones had been replaced after showing exfoliation. The tungsten peaks on the IBL top and bottom, just as for molybdenum, but the shift in toroidal direction is much higher than what was seen with molybdenum. Consequently, at the tungsten source it should hold: $v_{tor}/v_{pol} \gg 1$. To our knowledge there is no information available from measurements at TEXTOR about the poloidal variation of poloidal flow and drift strength. We therefore consult modelling results [49] as previously for molybdenum. According to Fig. 7 in [49] the poloidal velocity at r=46 cm is zero at the poloidal position $\theta/\pi = 0,4$ which is approximately at the top of the vessel, while at the vessel bottom the poloidal velocity is at least as big as the toroidal one. Consequently the majority of tungsten must have come from the top of the vessel: directly from the upper poloidal limiter and maybe partly from the lower limiter with tungsten revolving 2/3 of the poloidal circumference around the plasma, see Figure 23 (source A and B, respectively). However, the latter contribution cannot be significant; otherwise tungsten deposition on the ALT-II tiles would have been higher than what is observed in Fig. 22 at the toroidal position of the poloidal limiters. Hence the upper poloidal limiter must have been the major tungsten source. In [52] it is mentioned that for the upper poloidal limiter all stones had been replaced with freshly tungsten coated stones at some point during the experiment while only one stone was replaced on the lower limiter. Hence it indicates that the upper limiter experienced stronger damage which supports the previously stated point that the upper poloidal limiter must have been a stronger source of tungsten.

The next strong tungsten deposition peak appears close to the test limiter on the ALT-II limiter. There is no clearly enhanced tungsten deposition on the IBL on that place, contrary to the situation with molybdenum. Hence there must have been a tungsten exposure qualitatively different to that of the MoF_6 injection. Such an exposure seemed to have taken place multiple times with a solid tungsten or tungsten covered test limiter either at or within the LCFS [53],

[54], [55], [56], see Fig. 23 (source C). As a result the eroded tungsten moved in direction of the $\vec{E} \times \vec{B}$ drift *within* the LCFS, namely counter-clockwise towards the ALT-II limiter (plasma current in normal direction). For our MoF_6 injection experiment most molybdenum was carried with the $\vec{E} \times \vec{B}$ drift *outside* the LCFS which goes to the other direction.

In the toroidal direction all tungsten deposition peaks are smeared out more than molybdenum, most probably due to the longer residence time of tungsten impurities in TEXTOR from previous experiments. Also here a roughly exponential behaviour is observed, with e-folding lengths summarised in Table 4.

In summary the tungsten transport can be explained with the same transport scheme that we have developed in the previous section for molybdenum: transport outside the LCFS took place in clockwise direction, inside the LCFS it took place in the counter-clockwise direction. The tungsten sources were mainly either at or even inside the LCFS and hence tungsten transport mostly took place in counter-clockwise direction, see Fig. 23.

4.3 Medium-Z metals

Medium-Z metals comprise all elements between chromium and copper. The regularly applied RBS and ERDA analysis methods cannot separate them clearly, and since the sources of most of the elements (except copper) are roughly the same – Inconel liner and stainless steel structures – no effort was taken to measure them separately with other methods. Points of measurements are the same as for molybdenum and tungsten, see Fig. 15. The global deposition pattern is depicted in Figure 24a.

The first important observation is: the medium-Z deposition is not at all uniform. Consequently the liner as more or less symmetric medium-Z source (at least toroidally) cannot contribute much to the deposition pattern. All of the features must be explained by some kind of local source.

Again the strongest peak appears close to the poloidal limiters and can be associated with another poloidal limiter experiment where B_4C covered copper pieces had been tested [57]. These limiters had been exposed to SOL plasma 1 cm outside the LCFS and experienced strong unipolar arcing with penetration of the B_4C layers down to the copper substrate [58]. Subsequent investigation had shown that copper from the substrate had been lifted out of the arc craters. With unipolar arcs lifting copper from the poloidal limiter substrate through holes in the B_4C coating the copper should mainly end up around the LCFS and hence follow the

$\vec{E} \times \vec{B}$ drift towards the upper IBL, just as for tungsten. Splashing of molten copper should yield comparable copper amounts on IBL top and bottom at the same toroidal position as the poloidal limiters, which is not the case: the majority of medium-Z metals is found on the upper IBL with the same toroidal shift as for tungsten, indicating that movement with the plasma had been involved. Hence the same transport scheme as for tungsten applies, see Fig. 23, with the sources A and B, and the deposition areas 1 and 2.

Apart from the strong deposition peaking close to the poloidal limiters, there are several other areas of increased medium-Z concentration on the IBL, namely close to one ICRH antenna and to the counter-NBI injection position. Investigation of the previous IBL (1994-2003) with beta backscattering [59] already showed areas with increased metal deposition, see Fig. 24b (extracted from [59], modified and oriented as Fig. 24a). It is mentioned in [59] that the two areas (in Fig. 24b) with increased metal deposition coincide with the toroidal positions of one NBI port (at coil 7) and one GD antenna (at coil 16) and that liner damage had been observed at those positions. The areas of increased metal deposition in Fig. 24a and 24b do qualitatively coincide, disregarding the influence of the poloidal limiter in Fig. 24a. It can thus be speculated that the sources must have been the same, in 1990 and again 23 years later, which indeed is the case for at least two out of three: NBI (1986 [16]), ICRH antennae (1987 [18]), and GD antennae (no information available). This and the toroidal proximity indicate that the named subsystems are indeed the sources for medium-Z impurities found in either case. In an ICRH experiment [60] the effect of ICRH heating on SOL parameters, impurity release and hydrogen recycling had been studied, amongst others. It had been found that ICRH heating influences the SOL parameters and increases iron fluxes to the wall. It had been further noticed that at least the influence on the SOL can be observed only in the neighbourhood of the antenna, around 1 m distance. These findings are in line with studies of deposited layers at the ICRH antennae of TEXTOR where metal deposition is much higher on the antennae than on the ALT-II limiter, and the metal deposition increases during ICRH operation [61]. This can explain local medium-Z impurity deposition on the IBL near to one ICRH antenna, as seen in Fig. 24a, but it does still not explain the absence near the other ICRH antenna.

4.4 Comparison to other machines

The first example is from JT-60U where a toroidal tile section of the outer divertor was changed from the usual carbon to tungsten for two campaigns, followed by divertor tile analysis [62]. A toroidal spread of tungsten was observed on the so called outer wing, located

in the private divertor region (see Fig. 2, 8 and 9 in [62]). The tungsten was "smeared" out toroidally, with the maximum toroidally close to the tungsten source, just as for TEXTOR. The e-folding lengths are shorter though, possibly due to only two years of exposure to plasma and the different nature of the source: in JT-60U is had the form of bulk tungsten tiles which were present throughout these two years, while the source in TEXTOR was non-permanent. Obtained poloidal patterns at the toroidal position of the tungsten tiles can be interpreted as result of $\vec{E} \times \vec{B}$ drift through the private plasma from the outer to the inner divertor (see Fig. 2 and 6 in [62]) due to radial electric field [63]. This is also in accordance to findings in TEXTOR where the $\vec{E} \times \vec{B}$ drift seems to dominate poloidal transport.

The next example is from the IBL of TFTR analysed by beta backscattering for metallic depositions [64] which were later modelled [65]. The deposition profile of metals could be explained by this model that relied on the same formula as Equation 5 above (Eq. 1 in [65]). However, the deposition on the IBL was symmetric in toroidal direction with respect to the PFC periodicity (Fig. 3 in [64]) which is not the case in this study.

The last example is ASDEX-Upgrade (AUG), with a study conducted during the stepwise transformation from an all-carbon to an all-tungsten machine [66]. One part of the study was focused on the tungsten re-deposition in the divertor which can be explained due to transport along magnetic field lines: source and sink had a direct magnetic connection. This is a disagreement with results obtained in this study which shows no clear impurity transport along magnetic field lines.

Arriving at the end of this section, we note that for three impurity species – molybdenum, tungsten and medium-Z elements – deposition patterns were obtained. In all cases, the sources could be determined with some degree of certainty. A universal transport scheme applicable to all three species has been developed, based on plasma flows and $\vec{E} \times \vec{B}$ drift. The obtained insights do often agree with findings from two other machines, although in case of AUG disagreements remain. The transport scheme does furthermore not explain deposition patterns of recycling impurities, as will be seen in the following two sections about the impurities nitrogen and fluorine, and the plasma species deuterium.

5.   Global transport of light impurities

5.1 Nitrogen

^{15}N was seeded simultaneously with MoF$_6$, but 90° toroidally away from the test limiter, see Fig. 9 (light blue). During the experiment there was a clear memory effect visible, with a consecutive built-up of higher and higher nitrogen amounts in the plasma, see Fig. 4c. Such behaviour is known from previous injections [30].

Overall $5,3 \cdot 10^{21}$ ^{15}N atoms were introduced during 22 pulses, whereof a maximum of 26% were found again. The local deposition profile of nitrogen is shown in Fig. 11, which is very similar to the molybdenum deposition profile although the nitrogen source was at a completely different position, indicating deposition alongside molybdenum. Averaging over all measured points, the N/Mo ratio is about 0,16. Absolute amount of nitrogen deposited on the test limiter was negligible, $4 \cdot 10^{19}$ atoms, which was mostly ^{14}N. Only about 10% of the nitrogen was ^{15}N, resembling maximum 1‰ of the injected amount of ^{15}N. This value and all the following ones are an upper estimate because ^{15}N had been introduced into TEXTOR before and, unlike the case for molybdenum, no background estimate was available. On global scale nitrogen deposition on the ALT-II and the IBL were studied. The deposition in toroidal direction is shown in Figure 25 for both limiters. On ALT-II the deposition peaks at two positions: close to the test limiter due to deposition with molybdenum, and on a misaligned blade due to a few millimetres increased distance from the plasma and hence lower heat flux onto the limiter surfaces. The total amount deposited on the ALT-II limiter is $3 \cdot 10^{20}$ atoms or maximum 5,7% of the injected amount. On the IBL the ^{15}N deposition does not correlate with any other deposited species investigated in this study. For two investigated poloidal rows there was no clear deposition behaviour like the one in Fig. 19 and as observed for molybdenum. The total amount deposited on the IBL is ca. $1,1 \cdot 10^{21}$ atoms or maximum 20,6% of the injected amount. The ratio between the total amounts found on IBL and ALT-II is $3,6 \pm 1$ whereas the ratio between the PFC area of IBL and ALT-II is 2,6. Hence a preferred deposition of nitrogen on more remote PFCs (as the IBL) is likely, yet not significant when considering the uncertainty.

5.2 Fluorine

Fluorine was introduced into TEXTOR at several occasions in the form of hexafluorides through the test limiter, see Fig. 9 (dark green). Hence as for ^{15}N, the numbers given here with respect to the fluorine released during this study are upper estimates since information about background fluorine is missing.

The overall amount of released fluorine during this study was six times the amount of released molybdenum, i.e. $3,4 \cdot 10^{21}$ atoms. A great distinction to nitrogen is the absence of a memory effect, i.e. fluorine levels did not build up during the discharges, as can be seen in Fig. 4c and in [27]. This may be due to the high chemical reactivity of fluorine which may have caused quick and effective removal of fluorine in a carbon wall machine, e.g. by hydrofluorocarbons. Locally, fluorine was deposited only directly at the gas inlet, see Fig. 11, hence there was no clear co-deposition with molybdenum despite their simultaneous release at the same position. The total amount of locally deposited fluorine was $1 \cdot 10^{19}$ atoms or 0,3% of the injected amount.

The deposition on ALT-II and IBL in toroidal direction is illustrated in Fig. 25. As for nitrogen, fluorine deposition on the ALT-II limiter peaks close to the test limiter and on the misaligned blade. The total amount of fluorine deposited on ALT-II is $2,3 \cdot 10^{20}$ atoms or maximum 6,8% of the injected amount. On the IBL fluorine deposition does not correlate with any other species analysed in this study, just as nitrogen. Consequently measurements along poloidal direction did not yield a behaviour like the one described in Fig. 19. The total amount of fluorine deposited on the IBL amounts to $4,2 \cdot 10^{20}$ atoms or maximum 12,4% of the injected amount. The ratio between fluorine amounts on IBL and ALT-II is $1,8 \pm 0,5$ and is hence significantly smaller than the ratio between limiter areas, i.e. the deposition of fluorine took place preferentially on ALT-II.

Deposition of nitrogen and fluorine is similar on the main PFC, see Fig. 25a, while exhibiting differing behaviour on the more remote IBL, see Fig. 25b, and locally on the test limiter, see Fig. 11. Qualitatively, co-deposition seems to play a larger role for both elements than deposition on lower temperature PFCs, as can be seen from the peak heights at 0° and 110° toroidally in Fig. 25a. The behaviour regarding recycling is different, with nitrogen showing a clear memory effect while fluorine does not, see Fig. 4c. Remarkably, the amount of recovered light elements is in the same order of magnitude as the heavy ones but with a steady decrease towards higher atomic numbers – [15]N: 26%, F: 19%, Mo: 10-20%, W: 7-14% [27].

5.3 Comparison to other machines

The first example is from AUG. Previous experiments with ^{15}N in AUG yield high concentrations of nitrogen close to the point of injection, plus co-deposition with simultaneously injected [13]C [67]. Overall 10% of injected nitrogen had been found in the

experiment after analysis of 35 tiles and assuming toroidal symmetry. Just as in this study, large variations have been found on limiter tiles – in that case an ICRH antenna limiter. Deposition had been smaller in divertor regions with high heat flux in [67], agreeing with findings in this study where ^{15}N levels were an order of magnitude higher on the misaligned blade. The areal concentrations found in [67] and in this study are comparable for ALT-II (TEXTOR, Fig. 25a) versus divertor (AUG, Fig. 3 in [67]), and IBL (TEXTOR, Fig. 25b) versus ICRH antenna limiter (AUG, Fig. 2 in [67]).

The second example is from JET. In JET the amounts of not recovered, i.e. remaining nitrogen was found to be around 70% with carbon wall [31] and around 50% with ITER-like wall [32]. Shot-wise increase in nitrogen levels was observed in both experiments, just as in this study. For completeness, in [32] it is mentioned that the memory effect was not as severe with ITER-like wall, i.e. metal wall, than with carbon wall. In this study, only PFCs were taken into account for ^{15}N balance and hence the amount of overall ^{15}N remaining in TEXTOR after the final discharges is likely higher than the found 26%. Hence, both in JET and TEXTOR a considerable fraction of introduced nitrogen was not recovered.

6. Global fuel retention

The deuterium content in the sample was measured with NRA, using ^{3}He at 2,8 MeV, yielding a 10 µm detection range. This was in most cases sufficient to probe all the deuterium in the samples. Measurement was conducted on 43 tiles in 94 points, see Figure 26a. The interpolated fuel retention map is shown in Fig. 26b.

The most important and most apparent result is the strong variation of deuterium concentration on different PFCs, but also within one PFC. Assumption of toroidal symmetry is clearly not justified. Instead, fuel retention experiences strong variation throughout the machine just as any other element previously discussed, yet for different reasons. Before addressing the details we will list the main findings.

- Deposition on the ALT-II limiter, i.e. the main PFC, is homogeneous with an areal deuterium concentration of $3,8 \cdot 10^{17}$ cm^{-2}. The misaligned blade experiences an eleven times higher fuel retention due to its slightly increased distance from the plasma.

- Deposition on the IBL shows strong toroidal and poloidal asymmetry in fuel retention. This is both due to overall higher deuterium concentration in some areas, but also due

to varying layer thickness, as will be seen in Section 6.2. On average the areal deuterium concentration is $3,2 \cdot 10^{18}$ cm^{-2}, i.e. eight times higher than on the ALT-II.

The combined inventory on these two PFCs is thus ca. $3 \cdot 10^{23}$ deuterium atoms or 1g of deuterium.

6.1 Fuel retention on ALT-II

On ALT-II the fuel was deposited in the first 1-2 μm, even on the misaligned blade which simply exhibited a much higher concentration peak, see Figure 27a. The deuterium fraction in these layers was usually between 2 and 6%, and 14% on the misaligned blade. One investigated tile exhibited thick metallic debris on parts of its surface which had large influence on fuel retention and deuterium depth profile: the deuterium is retained even beyond the range of 10 μm with a remarkably homogeneous fraction of 4-7% of the debris, see Fig. 27a. The debris itself is mainly carbon despite its metallic appearance. Fig. 27b shows the detected deuterium concentration at different points of measurement on the tile with debris. Deuterium concentration along poloidal direction was also analysed on ALT-II, see Fig. 27c. With respect to the error bars the poloidal fuel distribution is rather flat, in stark contrast to what has been observed in previous fuel retention studies of ALT-II [48]. However, this can be explained by the selection of tiles: the tiles analysed in this study were from regions with small differences in incident flux, see Fig. 27d (adapted from Fig. 4 in [23]) while the tiles studied in [48] might have come from a region with stronger flux gradients. It is hardly possible to resolve the flux imposed fuel retention pattern even with the amount of data points available in this study because the spatial resolution of measured points in this study is far below the flux variations expected from [23]; hence the interpolation pattern in Fig. 26b does only show variations on large scale. Bearing this in mind, the amount of retained fuel on ALT-II may be larger than anticipated above, yet the overall figure hardly changes because of the much higher fuel retention contribution from the IBL, see next section.

6.2 Fuel retention on the IBL

Fuel retention on the IBL is more complicated for the following reason. Contrary to the ALT-II tiles the IBL tiles were never cleaned and have hence accumulated a decade of fuel

retention history which cannot be linked to specific events.

Thickness of deuterium containing layers on the IBL are up to 8-9 µm with most of the deuterium in the upper half of the layers, but in some cases also with non-negligible contributions from deeper layers, see Figure 28a. Please note the difference between two tiles spaced only ca. 15 cm apart, i.e. 444 and 446 (for positions please see Fig. 28c). Deuterium is depleted in the topmost 1-2 µm on all tiles. D/C ratios in the order of 0,01 – 0,1 indicate that the IBL surface was heated up to at least 700 K under plasma impact [68]. At positions with high fuel retention the deuterium levels are usually elevated over the whole depth range, proving that fuel retention has been built up continuously. Areas with low fuel retention consequently have an overall shallower deuterium depth profile. This means that the cause of the inhomogeneous fuel retention pattern had to be either permanently present over the IBL lifetime or regularly occurring. Such possible causes are: (i) plasma heating by NBI and ICRH, influencing the SOL and thus the fuel retention behaviour; (ii) local release of impurities, e.g. at the poloidal or test limiter position, and thus increase of co-deposition; (iii) inhomogeneity of wall conditioning methods such as GD cleaning, or boronisation and siliconisation with deuterated molecules. We will now investigate each of these possible causes (i) – (iii).

Cause (i): auxiliary heating

Auxiliary heating systems can influence fuel retention in two ways: first, they represent local impurity sources for limiter materials (carbon limiters at the ICRH antennae of TEXTOR) and metallic impurities (NBI scrapers, ICRH Faraday shields) for co-deposition of deuterium; second, local heating of the SOL by just a fraction of the wave power can increase PFC temperature and trigger release of deuterium. Both effects have been found in [60] where ICRH leads to increase of iron flux and temperature in the SOL. This temperature increase was found to be highest at r=49 cm (Fig. 6 in [60]), i.e. the radial position of the IBL, and locally restricted (ca. 1 m) which explains local deuterium depletion on the IBL near the ICRH antennae in Fig. 26b. Lessons learnt from ALT-II analysis shows that temperature seems to influence fuel retention more than co-deposition, leading to an overall negative effect of ICRH on local fuel retention and thus explaining the drop of deuterium concentration on IBL next to the antennae. This is in line with previous examinations of both deposits [61] and dust in the vicinity of ICRH antennae [33]. Depth profiles from two tiles are plotted in Fig. 28a (tiles 71 and 76, see Fig. 28c for positions).

NBI heating increases the density and particle flux in the SOL, but not so much the

temperature [69]. Hence, contrary to ICRH the NBI should *increase* fuel retention in the wall. Assuming *a priori* that this effect is also local, the observed higher fuel retention along the co-NBI injection path can be explained. The counter-NBI was not used as regularly which explains asymmetry between the two NBI positions.

Cause (ii): co-deposition by impurity release

Deposition both at the poloidal limiter position and the test limiter position is enhanced for high- and medium-Z elements, see Sec. 4. It is thus likely that eroded carbon from the very same limiters behaved similarly and got deposited on the IBL toroidally close to both limiter positions as well. This should manifest itself on enhanced amount of particle deposition. Indeed, when analysing width of surface peaks as indicators for impurity particle flux one can observe the following trend: higher fuel retention coincides with wider surface peaks, see Fig. 28b. This trend only holds on the IBL, proving yet again that PFC temperature is more important for fuel retention than co-deposition. However, on the IBL where temperatures are lower, co-deposition can enhance fuel retention considerably. A depth profile of the tile closest to the test limiter is shown in Fig 28a (tile 400, see Fig. 28c for position).

Cause (iii): inhomogeneity of wall conditioning methods

Amongst others, homogeneity of wall conditioning by carbonisation in TEXTOR has been investigated in [70] and was shown to be inhomogeneous. On average, carbon films are thicker close to the GD antennae than further away (Fig. 38 in [70]). Toroidal inhomogeneity exists also for boronisation [71]. Since there exists no symmetry of fuel retention either with respect to the GD antennae or the gas source of diboride, asymmetry in wall conditioning did not seem to play a major role in fuel retention pattern development.

6.3 Comparison to other machines

The first example is from investigation of the carbon IBL in TFTR [72]. The thickness of deposits was similar with up to ca. 10 μm. Deuterium concentration varied both poloidally and toroidally, ranging from 3 to $60 \cdot 10^{17}$ cm^{-2} which is comparable to what was found in this study. Comparing Fig. 1 and 2 in [72] shows that areas with high amount of deposition (in this case metals) had also high amount of fuel retention. The biggest disagreement is found in the deuterium depth profiles which do not exhibit surface depletion in [72]. Furthermore the maximum D/C ratio in TFTR exceeded 0,2 while it was maximum 0,12 in this study.

The second example is from JT-60U where retention from different hydrogen isotopes was studied in the divertor [73]. A linear relationship between fuel retention and deposited layer thickness was found which varied with position. A similar trend was also observed in this study at TEXTOR, yet only on the IBL. (H+D)/C ranges from 0,02 up to 0,13, hence the ratios found in JT-60U in [73] and in TEXTOR in this study are of the same order. Depth profiles exhibit deuterium surface depletion for the first 0,1 μm instead of 1 μm as found in this study.

The last example is from Tore Supra (now WEST after changing the PFM from carbon to tungsten) where the fuel retention of the main PFC in a time interval of 2002-2007 was studied [74]. In contrary to the main PFC in this study, the ALT-II limiter, the D/(D+C) fraction was an order of magnitude higher than for TEXTOR in this study. It should be mentioned here that Tore Supra operated with actively cooled main PFC. The depth profiles found in Tore Supra were qualitatively similar to those found in this study (see Fig. 3a in [74]), with deuterium depletion in the first 1-3 μm followed by a concentration peak, running out in a tail of decreasing deuterium concentration. Depth profiling in [74] yielded a good agreement between machine operation and depth profiles.

Analysis of fuel retention in TEXTOR shows large variation along both toroidal and poloidal direction, in accordance with findings from other machines. These variations are attributed to variations in deposition layer build-up and local plasma parameter variations, especially due to auxiliary heating systems and local particle sources. Quantitatively, we find lower deuterium concentration even on the receded IBL compared to other machines which is attributed to higher and quicker deposition layer build-up as compared to TEXTOR. Yet the fuel retention is in the same order of magnitude. Qualitatively, there is a disagreement in depth profiles: in some machines, surface depletion is seen, in others not.

Part II – modelling

7. Local modelling with ERO

Modelling of tracer injection and local deposition was undertaken with the Monte Carlo code ERO described in [75]. MoF_6 from this study and WF_6 from the study in [27] were modelled in [76]. No data on molecular dissociation of the two hexafluorides was available. Instead the ionisation of impurity atoms was adapted so the simulated line emission matched the observed one, see Fig. 2 and 3 in [76]. From helium beam measurements during the WF_6 injection

experiment the radial SOL profiles of T_e and n_e were available, showing exponential decay $(T_e(LCFS) = 30\ eV, T_I(LCFS) = 60\ eV, \lambda_T = 40\ mm;\ n_e(LCFS) = 5 \cdot 10^{12} cm^{-3}, \lambda_{ne} = 30\ mm)$. These profiles were used for modelling of both species since the plasma parameters were similar. Plasma parameter studies were also conducted on T_e and n_e where the values named above yielded best qualitative agreement with respect to the obtained deposition patterns. As impurities, 5,2% carbon and 1% oxygen were assumed. Enhanced re-erosion of deposited impurities was necessary to obtain quantitative agreement, as is frequently observed in such kind of combined experiment-modelling efforts. On top of that, it was assumed *a priori* that for each heavy impurity (Mo or W) six fluorine ions return to the test limiter surface.

The modelled deposition pattern of molybdenum yields an elongated shape along the SOL flow in toroidal direction and the $\vec{E} \times \vec{B}$ drift roughly in poloidal direction (the 3,6° deviation due to the poloidal magnetic field is neglected), just as in the experiment. A comparison between best modelled and experimental molybdenum deposition profiles on the test limiter is given in Figure 29a and b, using a tenfold increased re-erosion factor of molybdenum in order to obtain a similar net deposition efficiency of 6%. Without any increase the re-deposited molybdenum in the simulation is 56%, i.e. ten times higher than in reality, with a too pronounced tail, see Fig. 29c. A possible reason for such enhanced re-erosion of molybdenum is the fact that is was partly embedded into a matrix of lighter atoms, which increases re-erosion yields [77].

For tungsten, the same problem concerning quantification was observed in the model. Here, without any further assumptions the tungsten deposition efficiency was 26% instead of the experimentally observed 1%. With sputtering by fluorine and enhanced re-erosion factor of 20 the modelled deposition efficiency dropped to 3%. The toroidal deposition profiles of both ERO modelled and experimentally measured tungsten on the test limiter are shown in Fig. 29d. The ERO profile is divided by 3 due to its three times higher tungsten concentration. The qualitative agreement is nevertheless remarkable.

Modelling of both molybdenum and tungsten locally with ERO, and from previous efforts in modelling ^{13}C and Si deposition [78], [79] the local transport seems to be reasonably well understood. Even the missing dissociation data for exotic molecules like MoF_6 or WF_6 can be compensated by careful adjustment of dissociation coefficients in the modelling when spectroscopic information of the injection is available. What remains an area of active research since years is the correct quantification. Results published in [79] suggest that the

substrate might considerably influence re-erosion yields, which is in line with the ERO modelling results presented here, and with findings in [77].

8. Modelling of diffusion effects on global patterns with ERO

In Section 4.1 an approximately exponential decay of molybdenum concentration was observed on ALT-II, see Fig. 8a. Two explanations were offered above for the exponential decay: re-erosion – re-deposition steps, and diffusion across field lines. The latter has been investigated with ERO modelling and will be presented in this section.

Plasma parameters as in the previous section were used, adding also toroidal flow of 1×10^4 m/s, a perpendicular diffusion coefficient of D = 0,2 m^2/s in accordance with [2], [80] and a grazing incidence angle of the magnetic field onto the PFC of 0,01°. The sound velocity for the chosen plasma parameters was 5×10^4 m/s. For parameter studies, a ten times lower diffusion coefficient was modelled as well. The simulation environment is shown in Figure 30a. One million particles were simulated. We chose a charge state of Mo^{5+} because the ionisation potentials for several times charged molybdenum (Mo^{4+}: 46 eV, Mo^{5+}: 55 eV, Mo^{6+}: 69 eV) are comparable to the plasma temperature a few centimetres inside the LCFS where the simulation volume is located. In the experiment the tracer was injected radially into the plasma and then carried further along toroidal and poloidal direction for several decimetres up to metres before deposition. The details of injection are omitted in this simulation – the source is thus simplified to be 3 cm above and 3 m in front of the PFC with molybdenum ions moving toroidally. The huge distance between source and PFC allows for diffusion to take place. The PFC in the simulation resembles an exaggerated ALT blade with 6 m length. No re-erosion was considered in order to monitor the impact of diffusion on molybdenum deposition only.

The resulting toroidal deposition patterns are displayed in Fig. 30b, both showing exponential decay. For D = 0,2 m^2/s the e-folding length is 15 cm which is close to the experimentally observed value of 12 cm on the ALT-II in toroidal co-direction, see Tab.4. The deposited amount of molybdenum was 84% of the injected amount without re-erosion. For D = 0,02 m^2/s the e-folding length is 130 cm with 60% deposition efficiency. Hence, the experimentally observed diffusion coefficient value of 0,2 m^2/s in TEXTOR gives good agreement with what is seen in the experimental deposition patterns on ALT-II along toroidal direction, but not on the IBL. Furthermore the deposition efficiency in the simulation is more

than an order of magnitude higher than the observed one.

A possible explanation would be the following. On the main PFC re-erosion – re-deposition steps hardly occur because of the intense PWI which re-erodes most molybdenum without significant (permanent) re-deposition. However, on the IBL the PWI is more benign and re-erosion – re-deposition can take place, broadening the diffusion-smeared deposition profile further by around a factor of 5.

9. Global modelling with ASCOT

The Monte Carlo code ASCOT [81] can be used to model a whole tokamak with full 3D geometry. Information on the background plasma has to be provided in order to calculate migration of minority species, in this case molybdenum. This information was mainly taken from previous discharges conducted with the same or similar engineering parameters and comprises: radial profiles of electron and ion temperature and density [43] [76] [82] [83], toroidal plasma rotation profiles [43] [44], magnetic field profiles (EFIT output from the MoF_6 experiment discharges). The plasma itself was assumed to be pure deuterium. Together with quasi-neutrality this yields $n_e = n_i$. Temperature and density profiles were assumed to have parabolic shape. Figure 31 displays comparisons between profiles used in ASCOT and experimental values from the sources given above.

As markers, Mo^+ ions were introduced into the simulation environment which is displayed in Figure 32. The full gyro orbits were followed for 2 ms in the case of test runs, and 10 ms in the case of full simulations. Longer simulation times were not necessary as deposition of more than 90% of the markers happened well within 10 ms. In the following, test cases are denoted with lowercase Latin numbers while full simulation cases are denoted with uppercase Latin numbers.

The ASCOT model was first checked with a number of test runs to assure proper treatment of the Mo ions and the physical effects acting upon them. This was done by toggling different physics packages [PROPER DESCRIPTION?] of ASCOT on and off, and simulating the deposition regarding only the "activated" physics within 2 ms simulated real time. A simple point source was assumed for the markers at r = 48 cm, i.e. 1,3 cm above the real inlet position, with Mo^+ at an energy of 1 eV. The point source position thus coincides roughly with the MoI intensity maximum seen with spectroscopy in the experiment. Following cases were analysed and compared: (i) no interactions, i.e. gyrating movement along field lines

only, (ii) atomic processes only, i.e. ionisation and recombination by background plasma, (iii) Coulomb collisions only, i.e. momentum and energy transfer by collisions with background plasma species, (iv) both atomic processes and Coulomb collisions. The obtained deposition profiles are displayed in Figure 33. In Case (i), deposition is only local on the collector plate which intersects the magnetic field line at the point source, Fig. 33a. The length scale of the deposition pattern is thus in the order of the gyro radius which is around 0,6 mm. In Case (ii), changing ionisation status varies the gyro orbits, plus neutralisation makes it possible for the markers to change field lines. The result is a broadened deposition profile in the order of the ionisation length, hence a few millimetres, but still completely local on the collector plate, see Fig. 33b. Coulomb collisions enable a more effective change of field lines, plus the change of kinetic energy. Case (iii) thus displays a broader deposition profile than in Case (ii), and for the first time deposition takes place on global scale, i.e. on the IBL bottom, see Fig. 33c. In the last Case (iv), atomic processes and Coulomb collisions are combined, leading to deposition on collector plate, IBL, ALT-II limiter and the liner, see Fig. 33d. The local deposition pattern is not influenced greatly, whereas the global deposition changes dramatically by combining atomic processes and Coulomb collisions. However, the deposition in Case (iv) takes place close to the field line going through the point source, as can be seen in Figure 34. Within the simulated 2 ms, about half of the markers got deposited in all four cases, most of them locally on the collector plate. In Case (iv) a considerable fraction of the markers reaching the ALT ended up on the limiter backside. This modelling finding was checked experimentally by RBS measurements on ALT tiles and could be confirmed.

Full simulations were conducted for a number of cases, varying the nature of the source (point source versus radially extended source), and toggling radial electric field (and hence the $\vec{E} \times \vec{B}$ drift) as well as toroidal plasma rotation on or off. The different cases are listed in Table 5. The following trends were discovered with point source.

- Without electric field (Cases I and II), 64% of all markers end locally on the collector plate while the rest gets deposited on liner (20%) and IBL (5-6%) along the magnetic field lines. ALT-II receives only negligible deposition: ca. 1%. The toroidal rotation has some effect on deposition patterns but not on deposition efficiency of the different structures and PFCs. Case I is illustrated in Figure 35a.
- With electric field (Cases III and IV), considerably less markers end up locally, only around 20%. More than half of all markers are swept to the HFS and get deposited

right below the IBL. The two large limiters, IBL and ALT-II, in total receive only 1% of all markers. The deposition efficiency is unaffected by the electric field and is still at 21%. The deposition patterns are almost identical, hence the toroidal flow has no influence whatsoever. Case IV is illustrated in Figure 35b.

The agreement between simulation and experiment is *better* for Cases III and IV, both with respect to deposition efficiencies and obtained deposition patterns – but it is *not satisfactory*: deposition efficiencies on IBL and ALT-II are far too low while it is too high for the collector plate (local deposition); the simulated deposition pattern lacks two out of three deposition maxima present in experimental results, compare Fig. 15b and 35b. One key aspect in explaining the experimentally observed patterns was the radial molybdenum distribution displayed in Fig. 10b. Therefore, the simulations were repeated with radially extended source at different marker starting energies, 1 and 10 eV (Case V and VI). Remarkably, the starting energy did not have any effect on the deposition pattern, which is displayed in Fig. 35c for the 1 eV case. The extended source results in deposition mainly taking place at the bottom of the IBL, just as for Cases III and IV, but more outspread in toroidal direction. Deposition efficiencies for the extended source are close to experimentally found deposition efficiencies: 0,9% on the ALT (1-2% in the experiment), 8,2% on the IBL (7-11%) and 7,8% locally (6%). These numbers should however be treated with care since especially for the global deposition on ALT and IBL the deposition patterns do not resemble reality.

In summary, the following findings were made with the ASCOT simulations.

- Qualitatively, Case III and IV (with electric field and point source, with and without toroidal flow) match the experimental findings best. In the other cases, most of the markers were deposited in the wrong places. However, their quantitative agreement is poor: globally, the deposited areal concentration is a factor 10-12 too small.
- Quantitatively, Case V and VI (with radial electric field, toroidal flow and extended source) perform best, with deposition efficiencies agreeing with experimental values when taking the measurement uncertainties into account. Here the qualitative agreement is poor: the deposition pattern does not at all resemble reality.
- The following experimentally observed deposition features could be reproduced: deposition of molybdenum on the ALT backsides, very high deposition on the IBL bottom (also around the tile corner), local deposition profile stretching to the HFS due to $\vec{E} \times \vec{B}$ drift. Additionally, the shape of the deposition pattern on the IBL bottom could be reproduced, see Figure 36.

- The following features could *not* be reproduced: high deposition peak on ALT close to the source, deposition peak at the IBL top.
- Most of the markers ended up right below the IBL, i.e. not on the PFCs.

Summarising all the modelling outcomes a

Part III – overall scientific decommissioning, recollection and conclusions

Mapping a whole tokamak has brought to light a series of practical suggestions in case such an undertaking is to be repeated for another device. Due to the unique nature of the scientific exploitation of the TEXTOR dismantling, lessons were learned as analysis and evaluation proceeded which sometimes caused delays and setbacks. These can be avoided in the future. The next two sections focus on practical tips and suggestions for improvement to any scientist who engages in scientific exploitation of a tokamak. Note though that each machine is different and application of the following hints may need adaption. Finally, we recollect main findings and conclude.

10. Lessons learned from TEXTOR mapping

Knowing the history of a machine is a key element to set up a tracer experiment: (i) intrinsic and introduced elements and their source positions must be known; (ii) background concentration must be known for all elements of interest at the location of interest because toroidal symmetry can never be assumed *a priori*; (iii) well characterised and documented plasma scenarios must be used in order to be able to explain migration, especially in devices which are about to be decommissioned since re-measuring will not be possible. For later analysis, bear in mind how thick the deposited layers during the experimental period will become and whether they will be fully measurable with PFC analysis methods at hand. The impurity source must be monitored to understand patterns in the vicinity of the source, i.e. on neighbouring PFCs up to a few decimetres away: (i) detailed PFC geometry must be known; (ii) particle distribution after injection must be known, e.g. by monitoring line radiation; (iii) as many local parameters as possible must be known, amongst others electric and magnetic field, drifts, flow directions, temperatures and densities, diffusion coefficients. For optimal PFC selection for *ex situ* analysis, bear the following in mind: (i) magnetic field line topology, including field ripple which may cause large local differences in particle flux and hence deposition or retention (see Fig. 27d); (ii) drift directions, especially for the $\vec{E} \times \vec{B}$

drift; (iii) bulk plasma flows, bearing in mind radial (and maybe poloidal) variations. Depending on which structures one wants to see, one has to select tiles and points of measurement accordingly. Global migration takes places in length scales of metres, differences in particle flux due to field ripple and plasma position can give variations on decimetre to centimetre scale, and shadowing causes variations on millimetre scale. In any case, no symmetry of whatsoever nature can be assumed *a priori* for impurity migration studies, neither for impurity deposition profiles nor SOL parameters next to perturbing sub-systems such as auxiliary heating systems and gas injection limiters.

Modelling activities in conjunction to impurity migration experiments are highly encouraged since even in a well diagnosed device not all necessary information can be retrieved for analytical understanding. Another great benefit of modelling is the possibility to change plasma parameters at will or switch physical effects on and off, in order to understand their influence on migration and deposition patterns. This flexibility of modelling should however be handled with care, since with enough free parameters any modelled deposition profile can be brought into agreement with experimental results.

In general it is difficult to reach quantitative agreement between modelling and experiment. For local transport one may be able to explain discrepancies with re-erosion yields. For global transport it is very difficult to pinpoint the causes of qualitative and quantitative discrepancies with certainty. With the presented results, we attempted to study the influence of the most important parameters: radial electric field and the resulting $\vec{E} \times \vec{B}$ drift, toroidal plasma rotation, source form. While introducing the radial electric field had the highest *qualitative* impact on the deposition pattern, the change from point source to radially extended source had the highest *quantitative* impact on the deposition efficiencies of different PFCs.

If modelling activities are foreseen, they should start as soon as possible after first results are available. Not only does it take time to set up the environment for modelling and hence an early start can save time, but also first modelling results may give hints on where additional experimental results are needed in order to prove or refute a certain hypothesis. Secondly, detailed modelling – and interpretation of results – may crave information which has not been anticipated and may not even be available in published form. It then has to be retrieved from unpublished sources most possibly on site (laboratory notes, CAD drawings, staff members experience and remembrance). This must be done as soon as possible, especially for a decommissioned machine where invaluable (undocumented) information based on personal experience may become unavailable due to staff retirement.

11. Suggestions for improvement and further studies

Even meticulous PFC study and tracer quantification leaves a substantial gap in the particle balance for any tracer element, hinting at the fact that probably only the minority of injected tracers is deposited on PFCs. Archiving particle balance in tracer experiments is thus still unclaimed and calls for holistic studies, including pumps, ducts, ports and other receded wall elements which are non-uniformly covered with all kinds of deposits [34]. In the light of global ASCOT simulation results, very much emphasis should be given to structures intersecting the $\vec{E} \times \vec{B}$ drift direction.

From the overall TEXTOR study, a range of open questions remains: (i) the role of magnetic field ripple and hence variations in local particle fluxes, which may have caused an underestimation of fuel retention on ALT-II, and which might explain local variation of areal molybdenum concentration on ALT-II near the gas inlet; (ii) heating systems as (local) sources of metallic impurities and their influence on local fuel retention which has been discussed only qualitatively here; (iii) deposition profile broadening due to diffusion and re-erosion – re-deposition, whose importance is seen both in experiment and modelling but which are hard to distinguish from each other with certainty.

For the ASCOT simulations themselves, parameter studies remain where physical quantities are varied to estimate their importance on (simulated) transport. Also, re-erosion should be included into the simulations. Both points may be addressed in the near future.

12. Conclusion

The complete studies on TEXTOR wall components and on local and global high-Z transport have been reviewed in recent publications and complemented by hitherto unpublished data. Extensive modelling, both on local and global scale, has been carried out to deepen the understanding of obtained deposition patterns. In some cases, analytical treatment of the found deposition profiles was possible by considering the PFC geometry, the particle distribution at the source and the flow patterns. In the field of PWI research, the following milestones and major conclusions could be reached:

- For the first time, results from tiles of all PFCs and liner pieces were stitched together to obtain a complete material migration pattern including deposition profiles and efficiency.

- About 20% of all molybdenum tracer species released during the very last TEXTOR experiment could be found by analysing molybdenum concentration in 570 points on 140 wall tiles (16% of the total number) throughout the whole machine.

- Several features of the determined deposition patterns could be explained analytically by basic consideration of PFC geometry, SOL physics and radial particle distribution at the source. The radial marker distribution at the source together with the $\vec{E} \times \vec{B}$ drift and toroidal plasma flow define the relative marker deposition efficiencies on PFCs.

- A transport scheme was derived from molybdenum deposition and knowledge about drift and flow directions, which is also applicable to other species, namely tungsten and medium-Z metals (Cr – Cu) introduced into the plasma in previous experiments and through continuous machine operation.

- For the first time, a full machine fuel retention map was obtained, based on 94 measurement points throughout the whole machine. It exhibits a poloidally and toroidally asymmetric retention pattern, due to auxiliary heating systems, PFC distance to the plasma and local deposition rate variation e.g. through impurity injection. Due to the large distances between analysed points, only features with decimetre length scale or higher could be resolved.

- Local simulations show very good qualitative agreement with experimental results. Quantitative differences could be overcome by enhanced re-erosion yields.

- Global simulations show the high importance of diffusion coefficients, $\vec{E} \times \vec{B}$ drift and the source form (point source versus radially extended source). However, achieving qualitative and quantitative agreement remains a huge challenge.

Nitrogen injection for edge cooling has resulted in a noticeable memory effect during the last TEXTOR experiment. This has been in accordance with lessons learned from other machines. Maximum 26% of the injected ^{15}N could be found again on all PFCs. Fluorine from the injected MoF_6 did not produce a memory effect, also in accordance with observations from other experiments. Maximum 19% of the injected fluorine could be found again on all PFCs.

In summary, the study took the effort of several years, many weeks of beam time and another year in total for several modelling approaches. It proves that scientific exploitation of a decommissioned tokamak is a major research project in its own right. However, the gained knowledge is very valuable and difficult to obtain otherwise. We thus encourage similar projects in conjunction with the decommissioning of other medium-size tokamaks in the future.

13. Acknowledgements

Figure 1: photograph of the TEXTOR interior and pictorial key to in-vessel components. The red arrow indicates the MoF6 injection point just behind the Inner Bumper Limiter. View is in direction of the magnetic field under normal configuration.
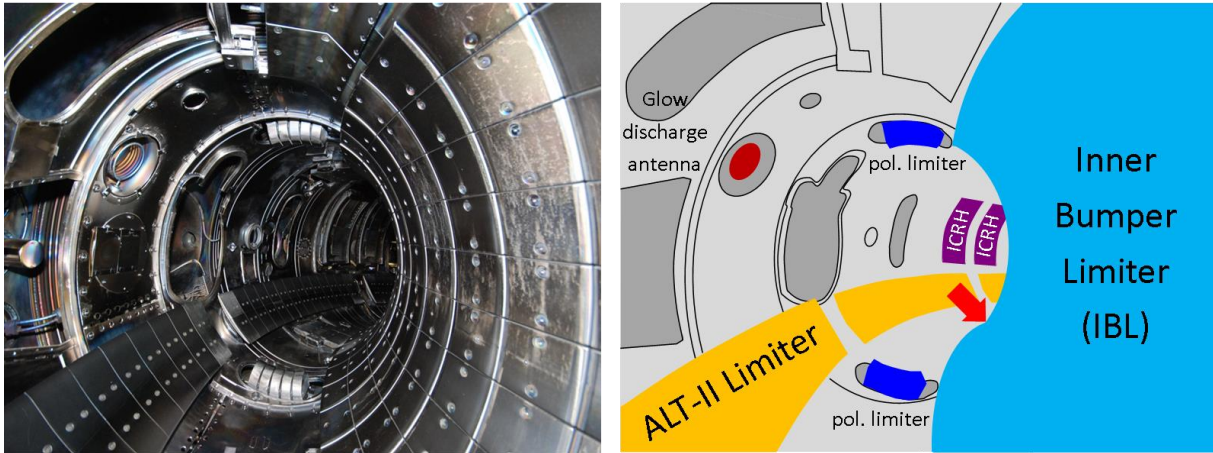
Figure 2: Centre: TEXTOR cutaway drawing, showing the most important subsystems –
transformer (turquoise), liner shell (orange), NBI boxes (transparent grey), ICRH antennae
(purple), injection system and test limiter (red), spectroscopy port for injection monitoring
(green, "View") – as well as the plasma current (yellow arrow) and toroidal magnetic field
(red arrow) for normal configuration as in this experiment. Details of the PFCs and wall
probes are displayed in exploded-view drawings: a) collector probe (grey) with carbon catcher
plates (black stripes) shielded by a tantalum cap (dark red); b) poloidal limiter (top part, dark
blue) with individual five "stones"; c) one ALT-II main limiter blade with Inconel carrier
(orange) and individual tiles (dark grey); d) IBL tile column with ten tiles (light blue), two of
which are shown in detail (pay attention to the corners of the uppermost and lowermost tiles);
e) test limiter with injection channel and catcher plate (light red). Colour online.
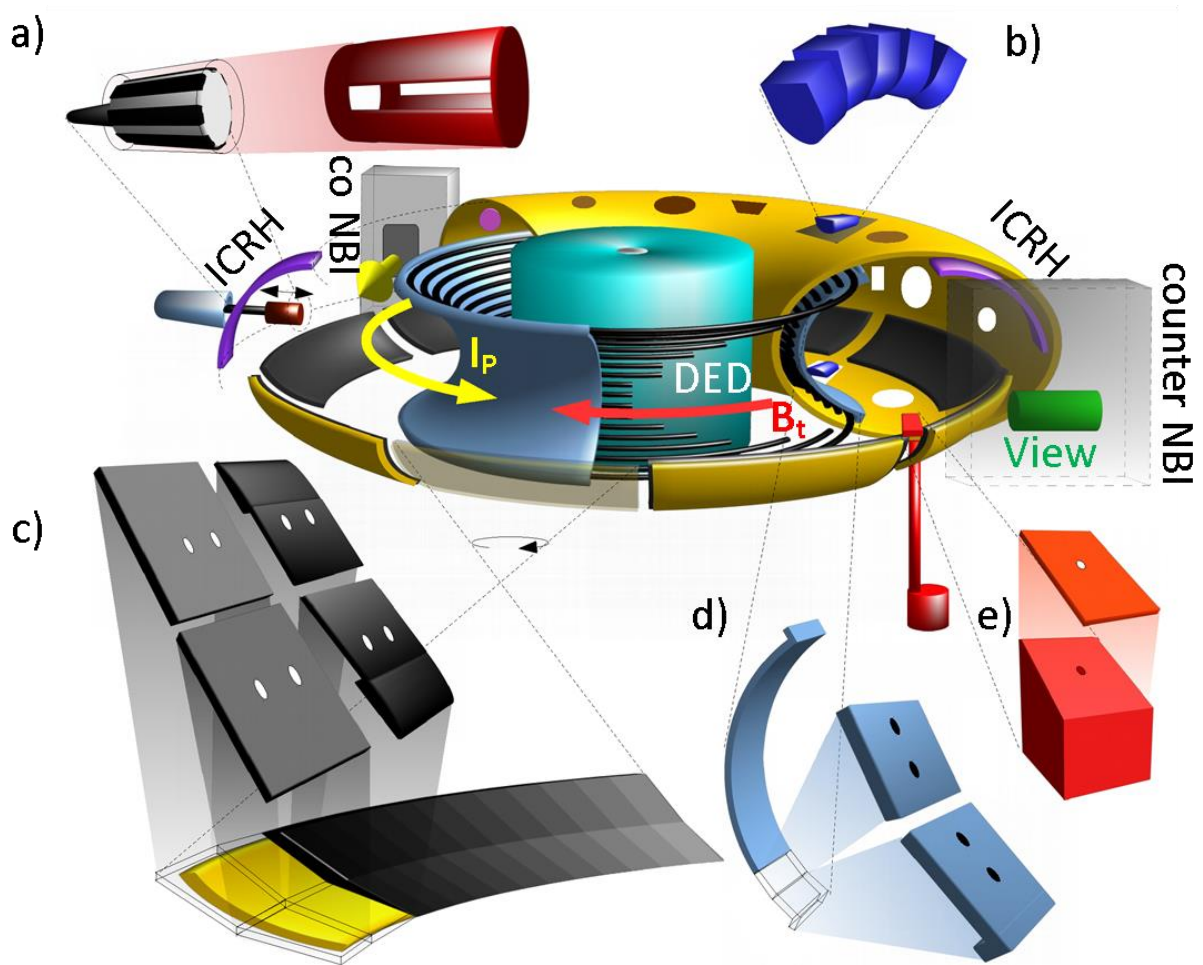
Figure 3: Photos from a) PFCs – test limiter (plasma current direction indicated by yellow arrow), ALT-II tile, IBL tile and poloidal limiter "stone" (f.l.t.r.) – and b) ALT-II Inconel support structure (backside) with neutraliser box. Please note the colourful deposits on PFCs and support structures alike, as well as thick flaking deposits on the poloidal limiter stone and the neutraliser plates.
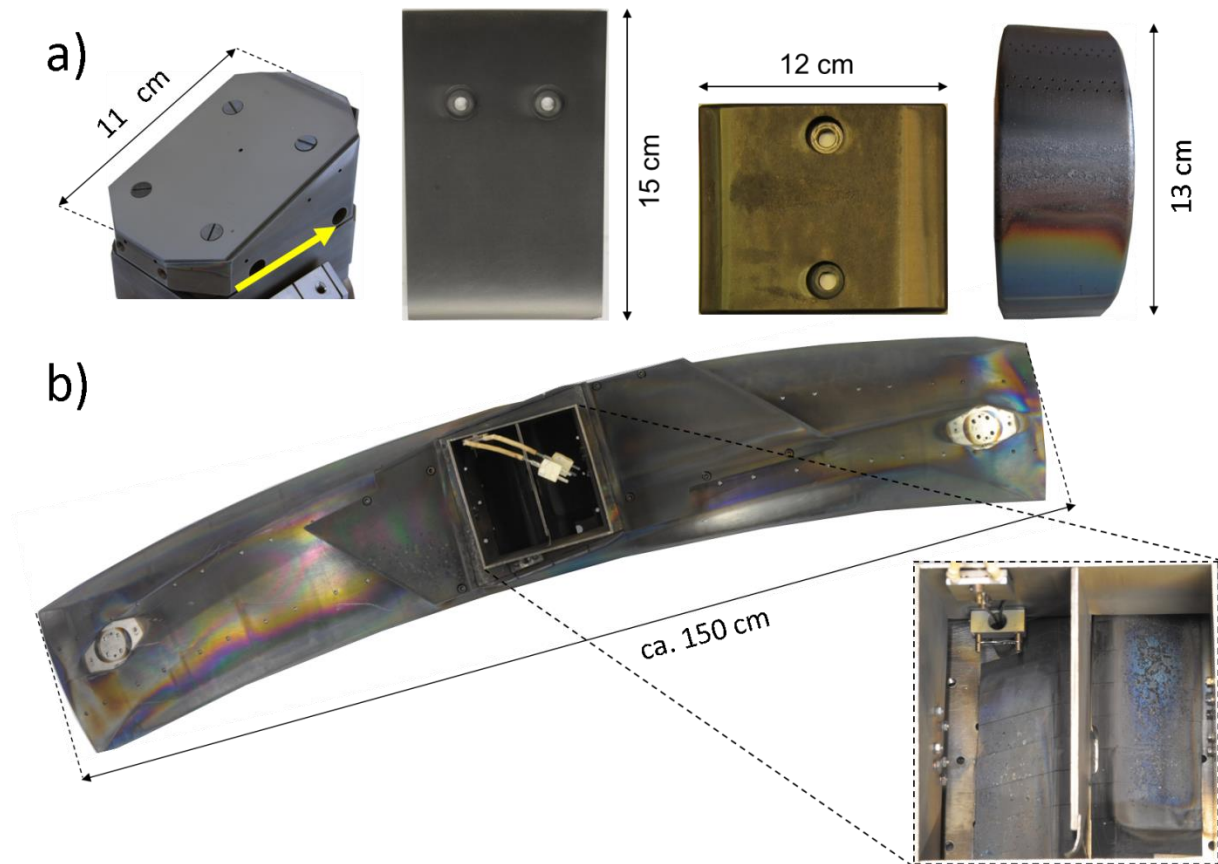
Figure 4: a) discharge time line, b) liner radiation of Mo and F at the inlet, c) ^{15}N and F core VUV signals showing memory effects of ^{15}N but not for F. Please note the disruption at shot number 120999 (black solid line).
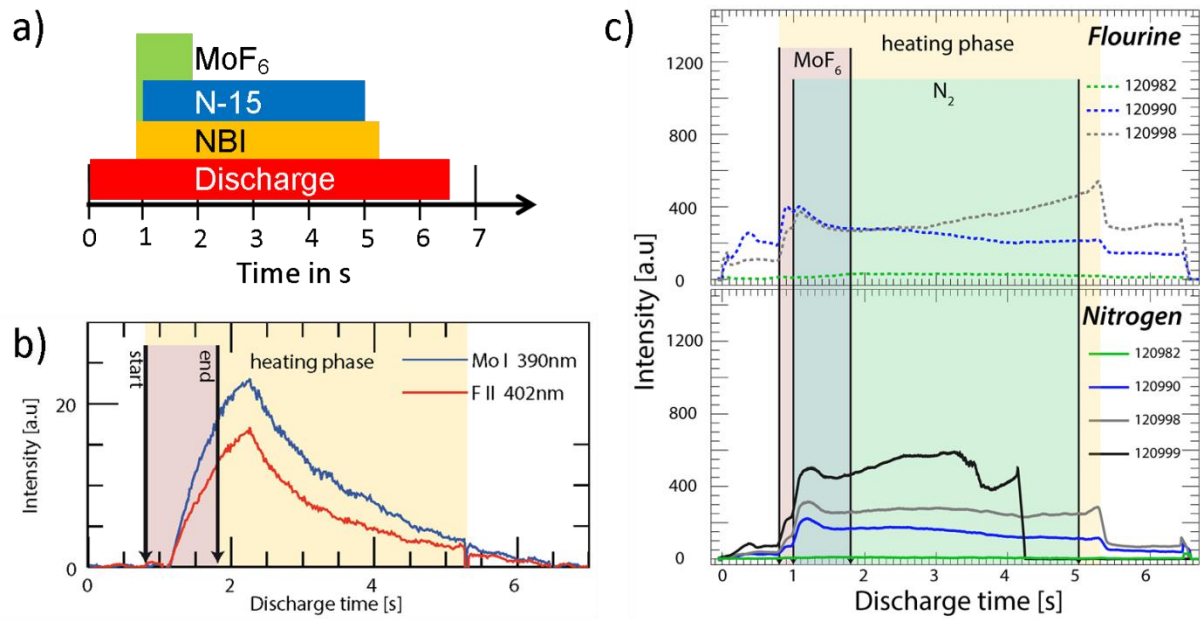
Figure 5: RBS spectra. a) Spectrum from an ALT-II tile with homogeneous depth profiles and five well separated elements, fitted with SIMNRA. b) Spectrum from another ALT-II tile, with many features and most probably inhomogeneous depth profiles. The amount of features in the spectrum makes it hard to interpret. c) SIMNRA simulation of a B+C target – 10 counts correspond to roughly 1% for C. d) SIMNRA simulation of a C+W target with same beam particles times steradian as in c) – 10 counts correspond to roughly 50 ppm for W. Beam in all figures: [4]He at 2 MeV.
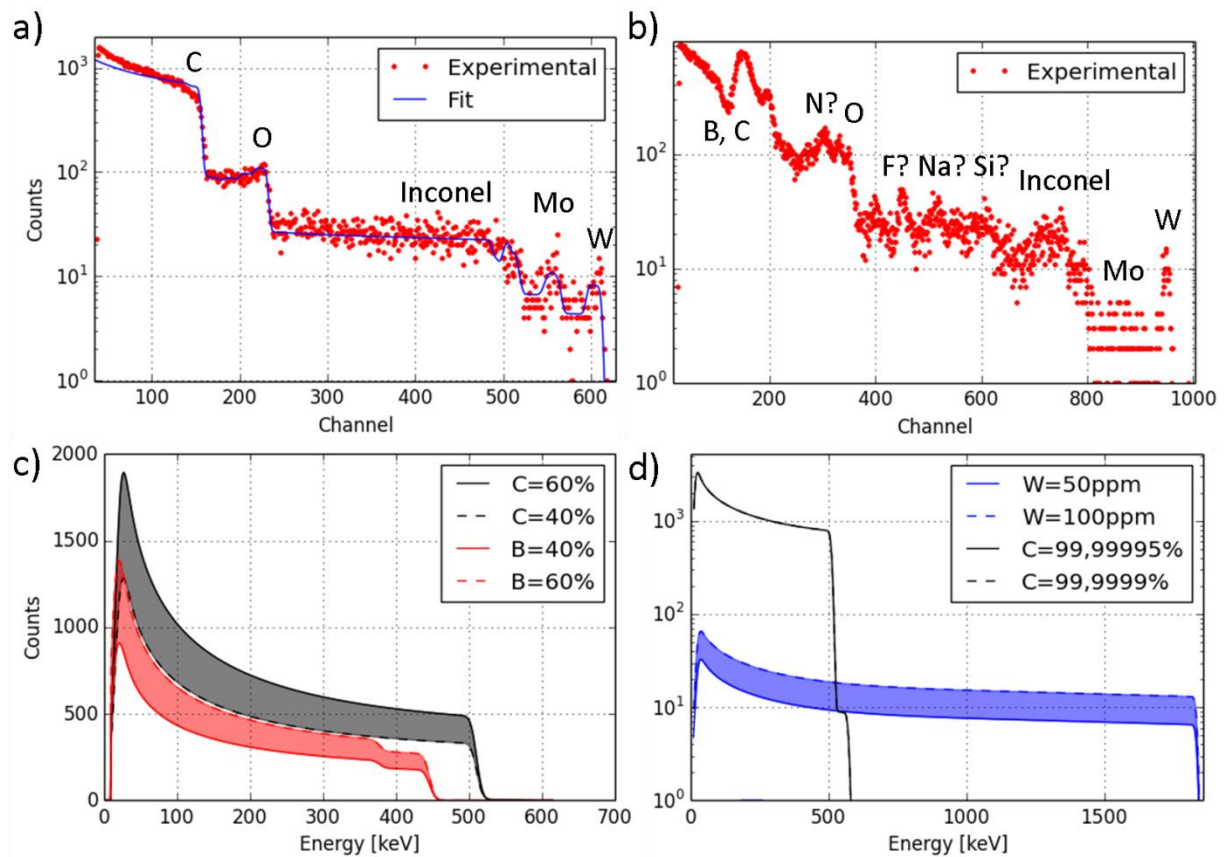
Figure 6: ToF ERDA spectrum of a TEXTOR tile, showing the composition of the top 5-600µm with mainly B, C and O. All element counts are accumulated in separated parabola. Please note the isotopic resolution for low-Z elements (here: H and D, ^{10}B and ^{11}B).
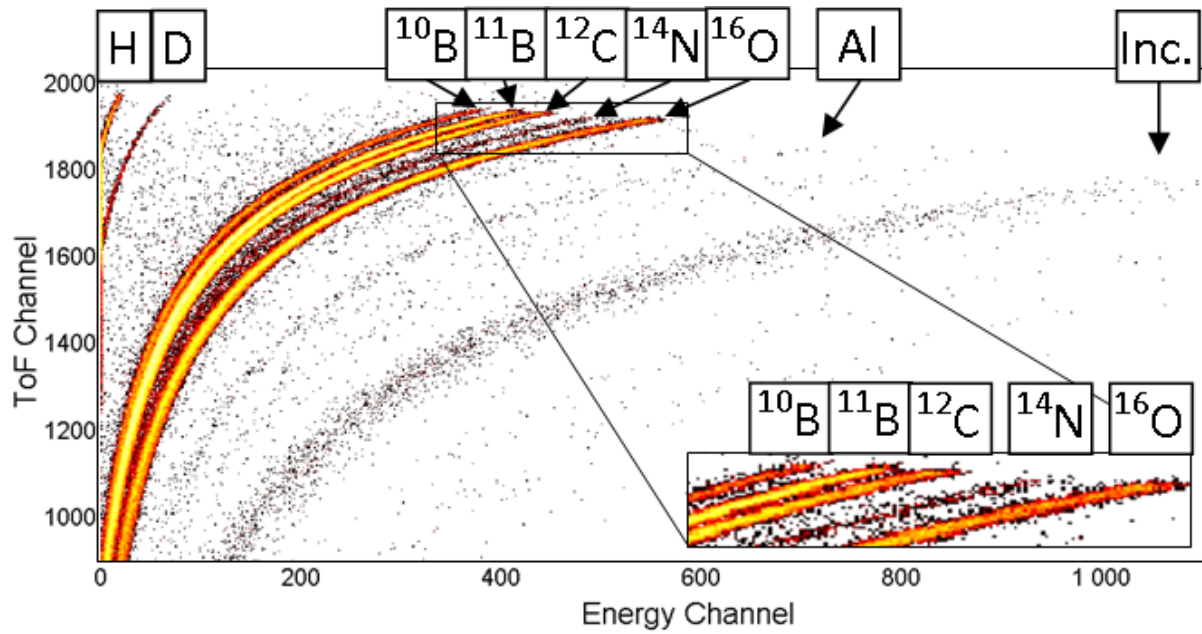
Figure 7: NRA spectra obtained with SIMNRA; a) – experimental spectrum from an ALT-II tile with mostly carbon and surface deuterium signal; b) – simulated spectrum of a homogeneous sample with 79% carbon, 20% boron (natural isotopic composition) and 1% deuterium, showing the overlap of deuterium signal from greater depth and boron-11 signal (beam in both figures: ^{3}He at 2,8 MeV).
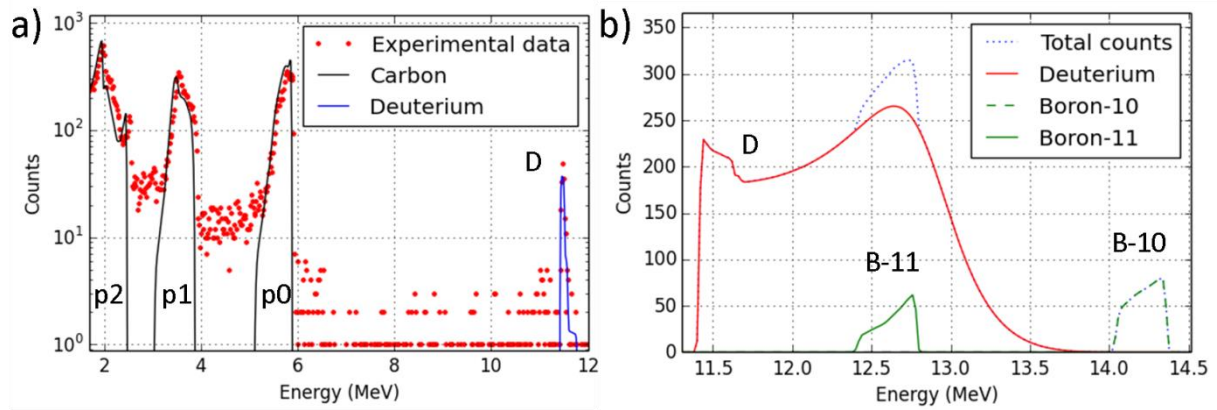
Figure 8: a) Comparison of measured points (dots) with error bars and interpolation (red line) of the areal molybdenum concentration on the ALT-II limiter of TEXTOR along toroidal direction (values from upper part, poloidally); b) as in a), only with $320 \times$ higher smoothness.
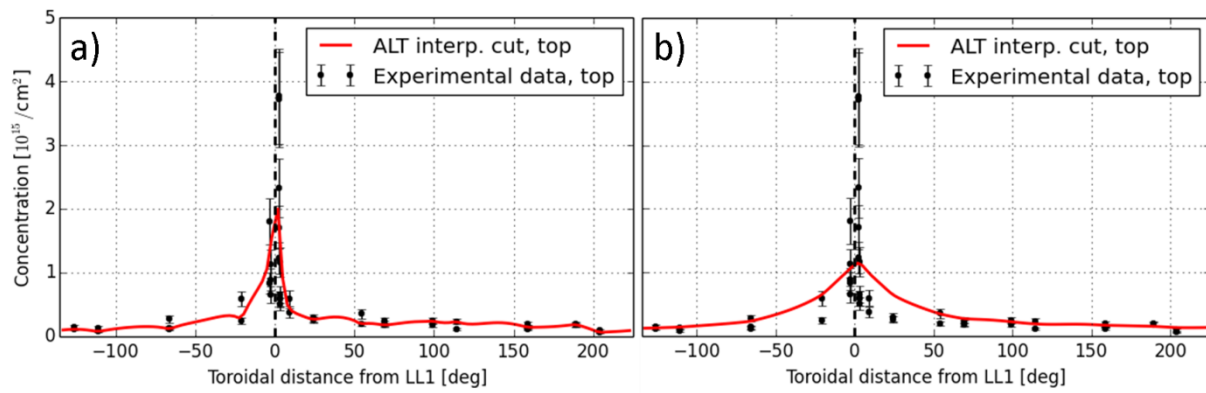
Figure 9: schematic drawing of element sources in TEXTOR which will be relevant for later discussion – top view. The same orientation will be used in later interpolation maps.
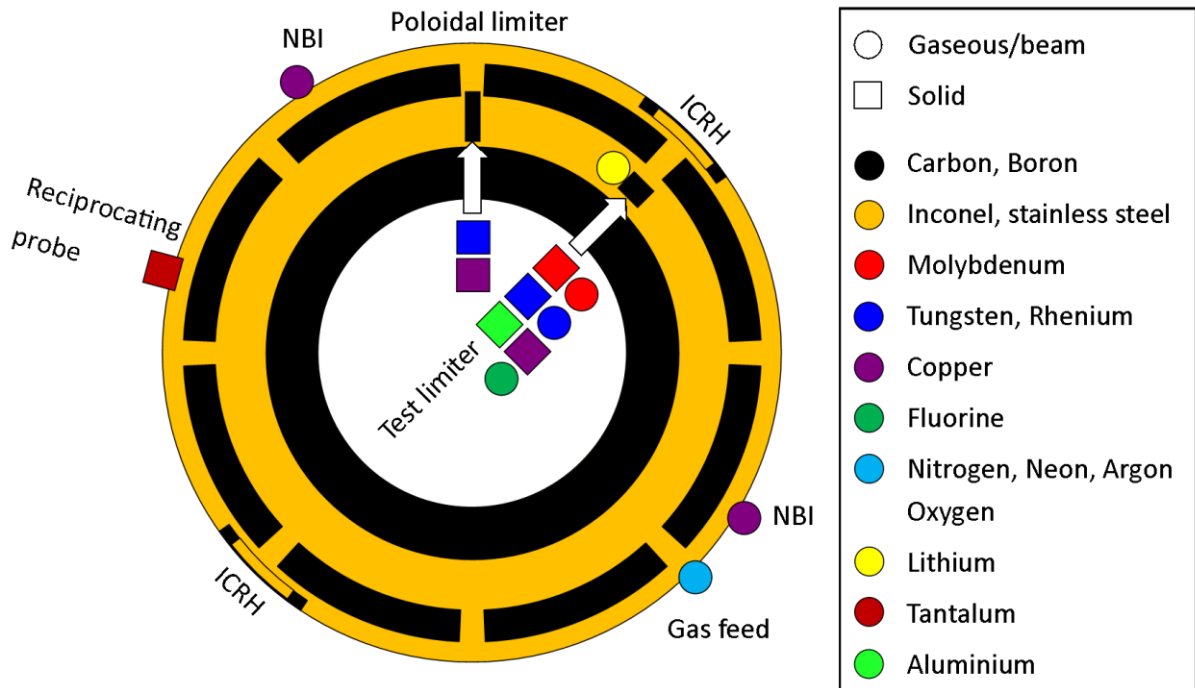
Figure 10: a) Spectroscopic image of the MoI line radiation summed over all frames in shot no. 120975; b) measured MoI line intensity (black, taken from Fig. 9a at the red vertical line) and fitted by a Cauchy distribution (red); c) isotropic point source, yielding a Cauchy distribution whenever the particle amount is projected on a vertical line at some distance s.
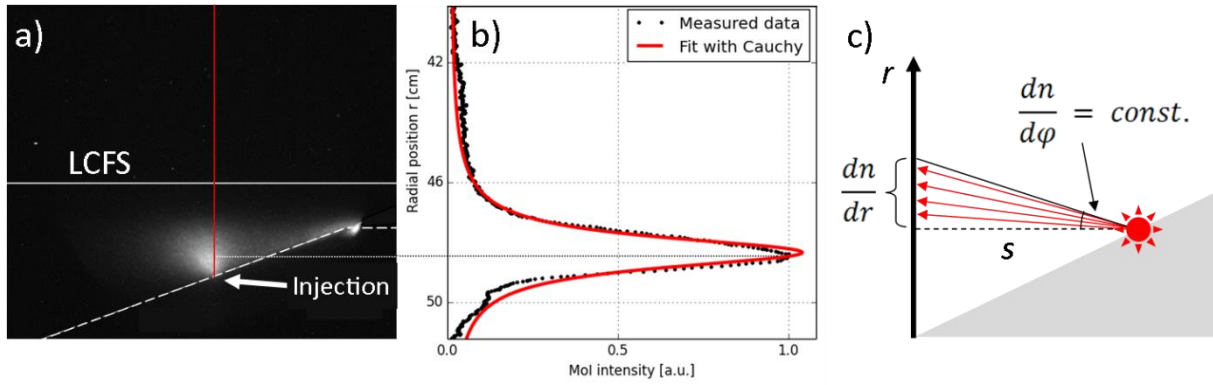
Figure 11: deposition patterns on the collector plate on top of the test limiter, showing deposition thickness and the areal concentrations of molybdenum, nitrogen, fluorine, oxygen and titanium. The arrow indicates the position of the gas inlet. The plasma current goes from left to right, i.e. the limiter tip is to the right (see also Fig. 2a), and the inboard side is to the top.
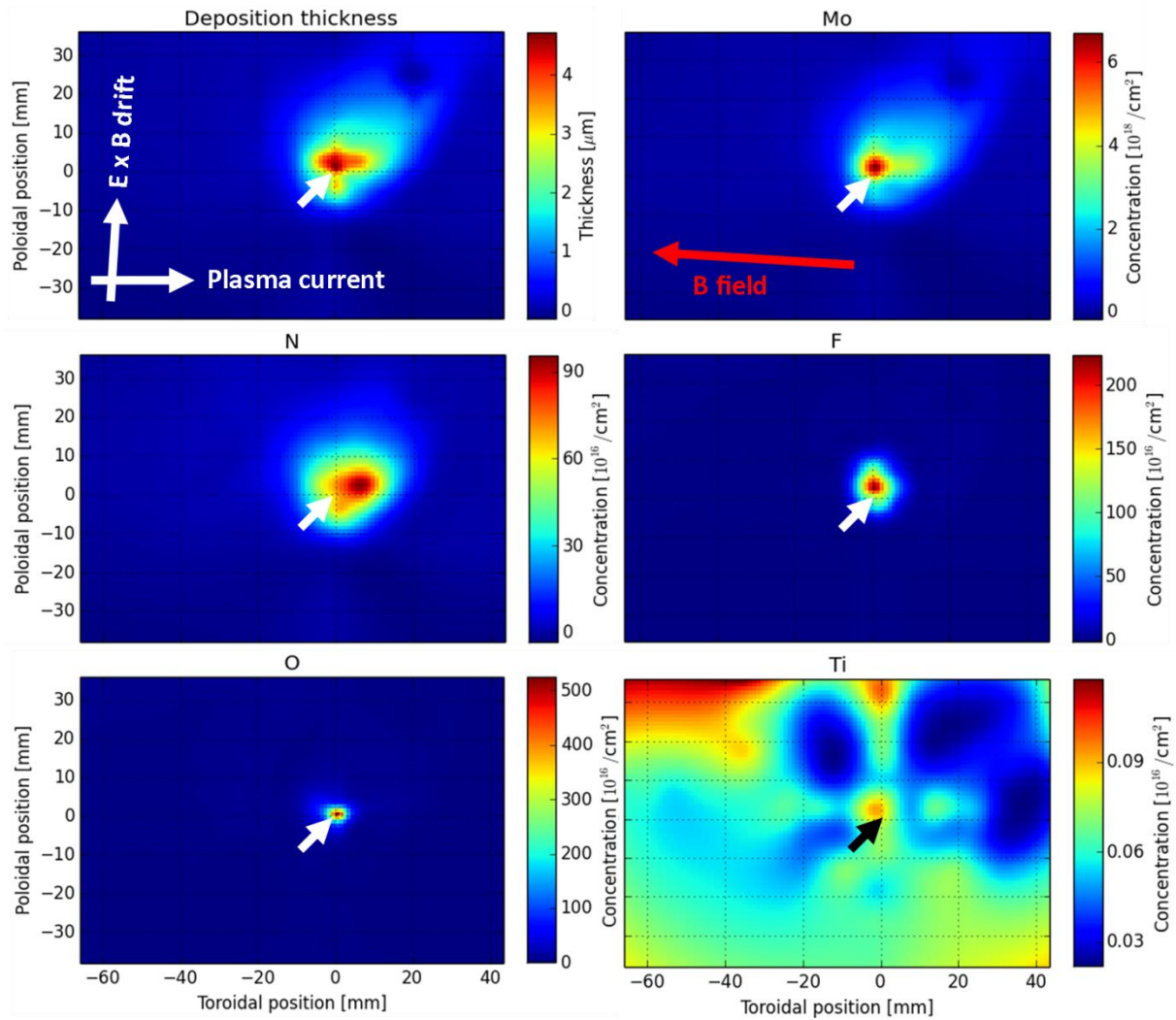
Figure 12: molybdenum concentration on the collector plate in toroidal and poloidal directions, resembling the same distributions as for the MoI line radiation. Experimental values are from the EPS measurements only due to their higher reliability close to the gas inlet at (0|0).
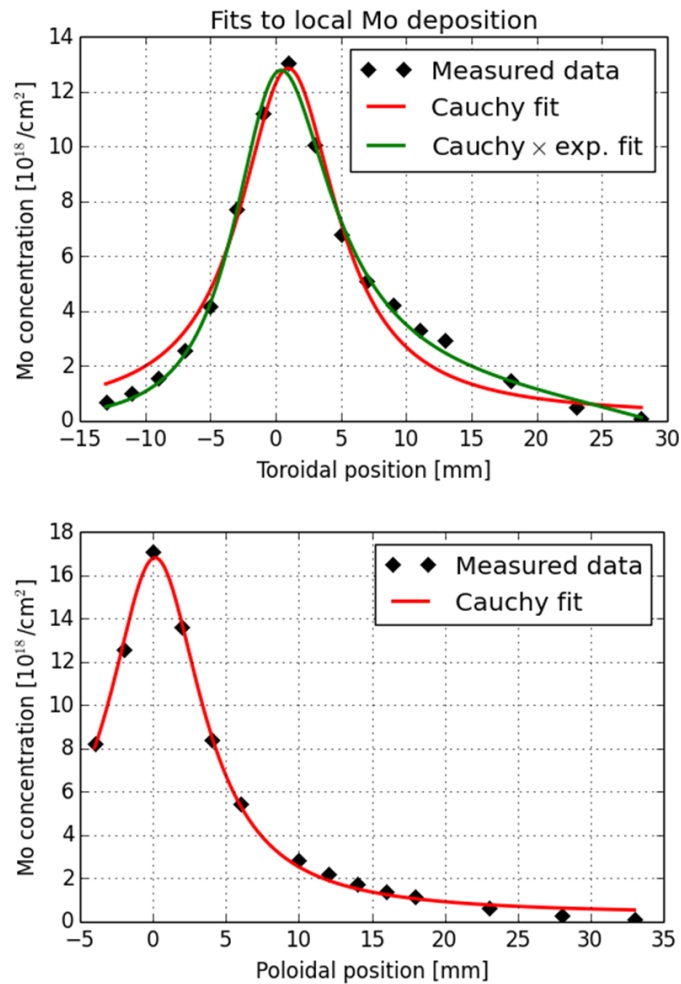
Figure 13: SIMS measurement on the collector plate close to the gas inlet – a) depth profile of the sputtered craters, b) depth profiles of Mo and C (other elements are omitted here), c) amount of injected MoF$_6$, recorded as pressure drop at the calibrated volume.
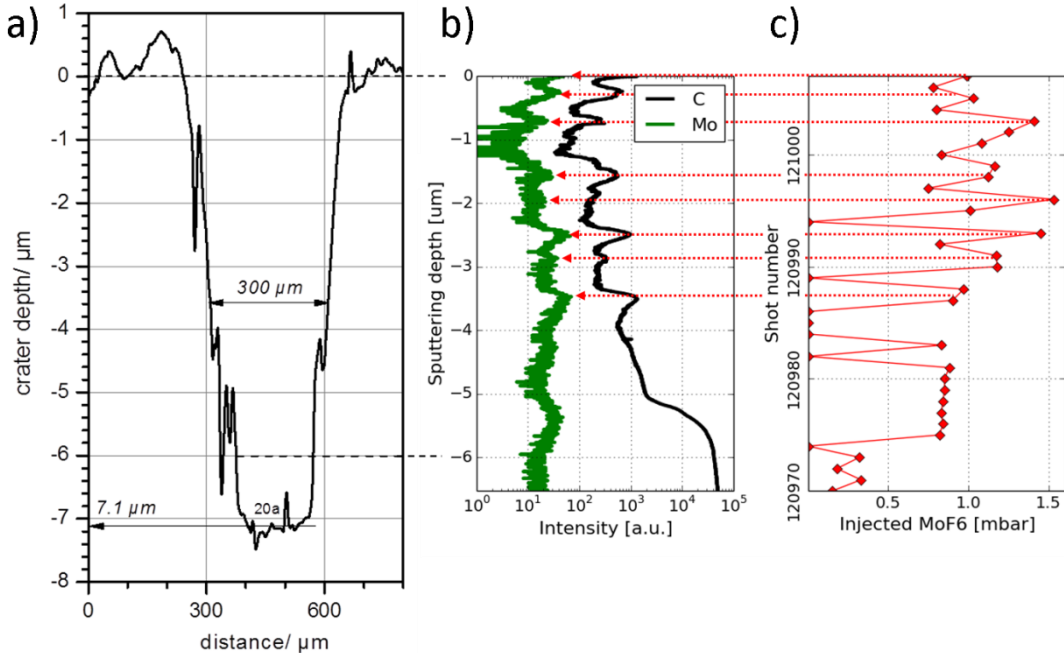
Figure 14: Local tungsten deposition on the collector plate from the experiment described in [27]. Again a Cauchy distribution can be seen along the toroidal direction, while a Gaussian does not represent the data as well. Measurements were conducted along the yellow arrow while the WF_6 injection point is encircled red.
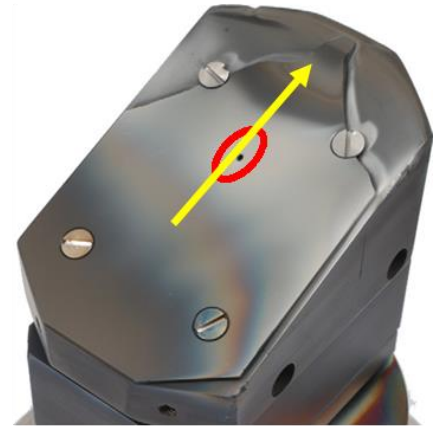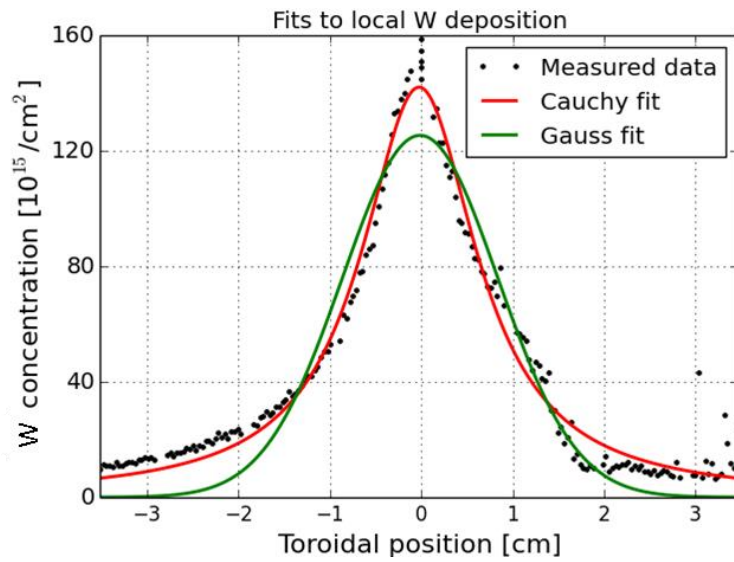
Figure 15: a) measurement points for RBS on ALT-II and IBL, in total 571; b) molybdenum deposition pattern of the topmost 50-150 nm, i.e. excluding data from a disruption happening 11 shots before the end of the experiment. The IBL is the inner closed ring with the top towards the centre and the bottom towards the ALT-II. The black dot and cone denote the point of view for Fig. 16.
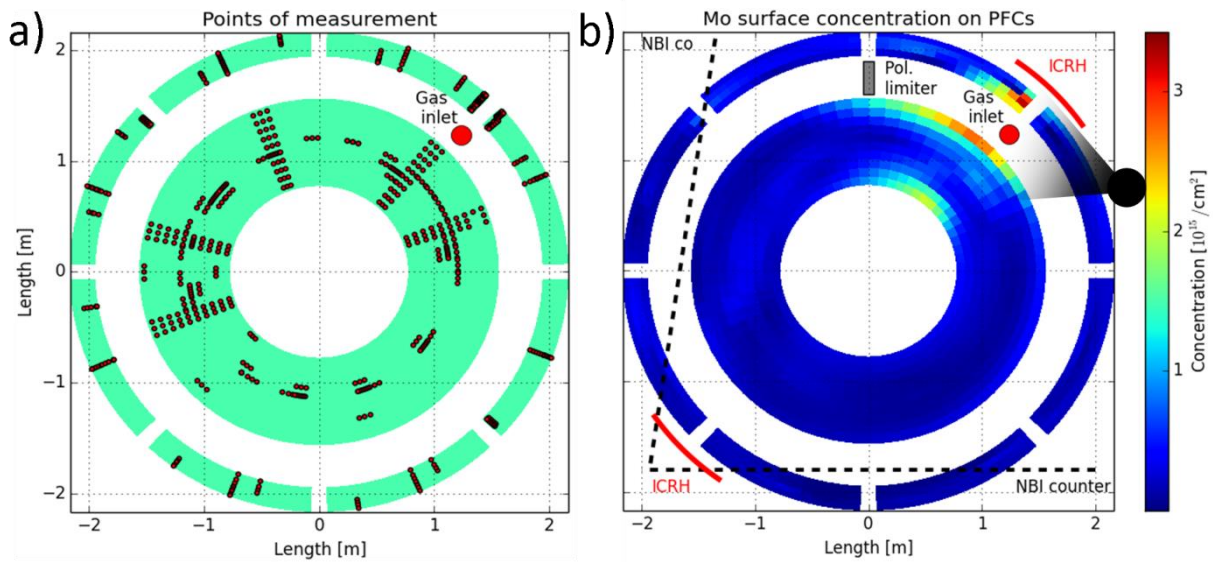
Figure 16: molybdenum transport along poloidal flows (black solid arrows) from the point of injection (0) to the lower part of the IBL (1) and towards ALT-II (2), with flow reversal at the LCFS. Deposition at the IBL top (3) may be due to re-erosion from points (1) and (2), and due to particles which do not get deposited at those points but simply continue further along the poloidal flow (black dashed arrows). Sub-systems except the test limiter (red) have been omitted for clarity. The point of view is illustrated in Fig. 15.
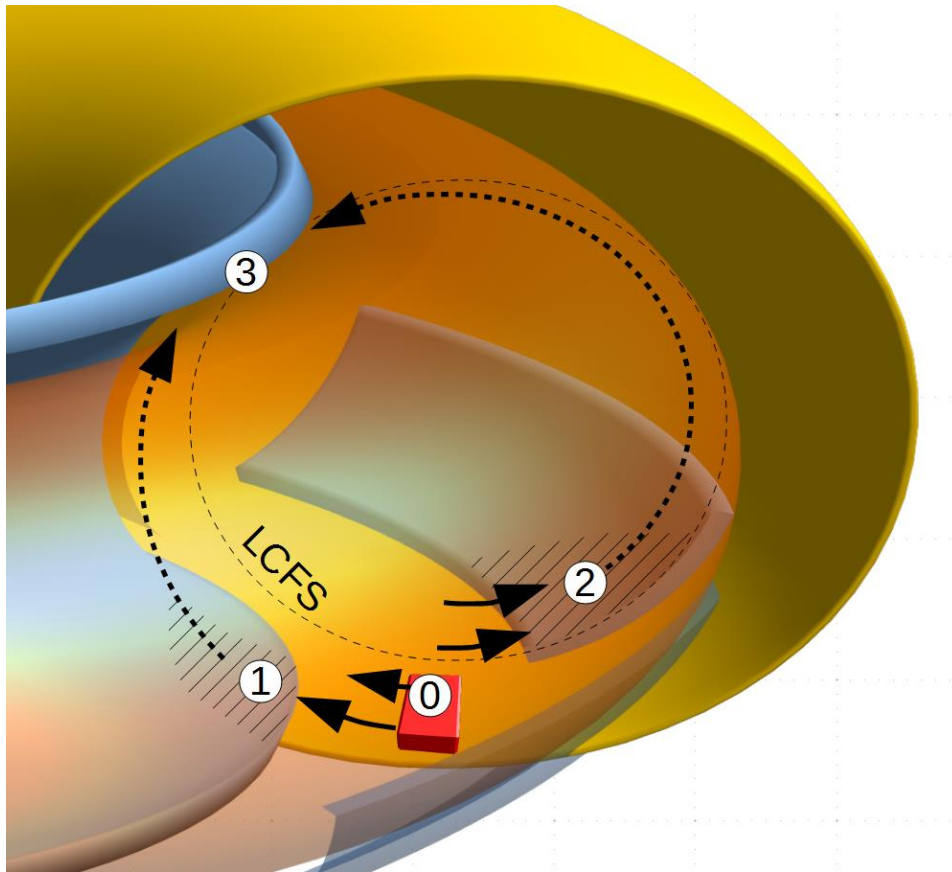
Figure 17: a) detailed geometry of a poloidal TEXTOR cross-section, showing the relation between distance from the plasma centre and distance from the IBL curvature centre; b) the impact angle α for impurities and positive Δ (plasma centre shifted towards HFS) and c) negative Δ (plasma centre shifted towards LFS).
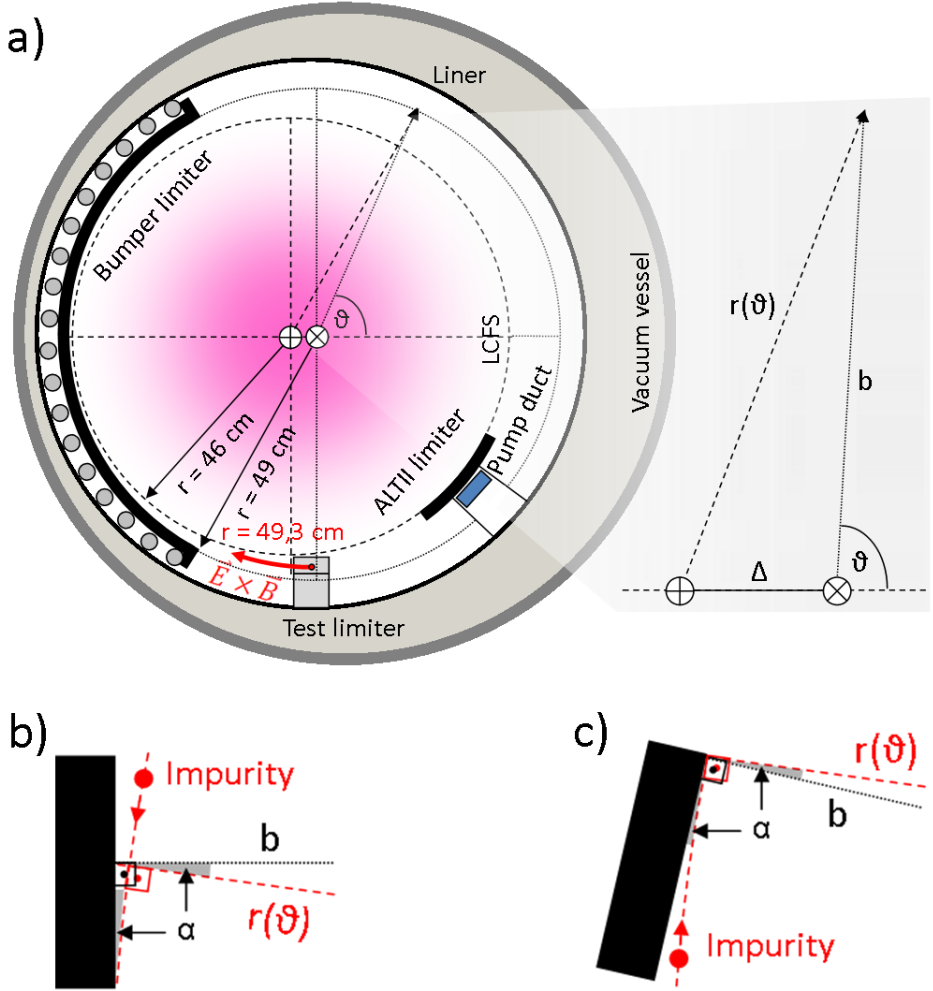
Figure 18: measurements at the toroidal position of the gas inlet, both plasma-facing tiles sides (green stars) and lower part of the bottom tile (yellow stars). The $\vec{E} \times \vec{B}$ drift carried the Cauchy distributed molybdenum towards the HFS where it was smeared across the different sides of the tiles (green and yellow zones). However, the distribution was distorted during the "travel" towards the HFS from a Cauchy distribution (blue) to a Cauchy distribution times an exponential function (red).
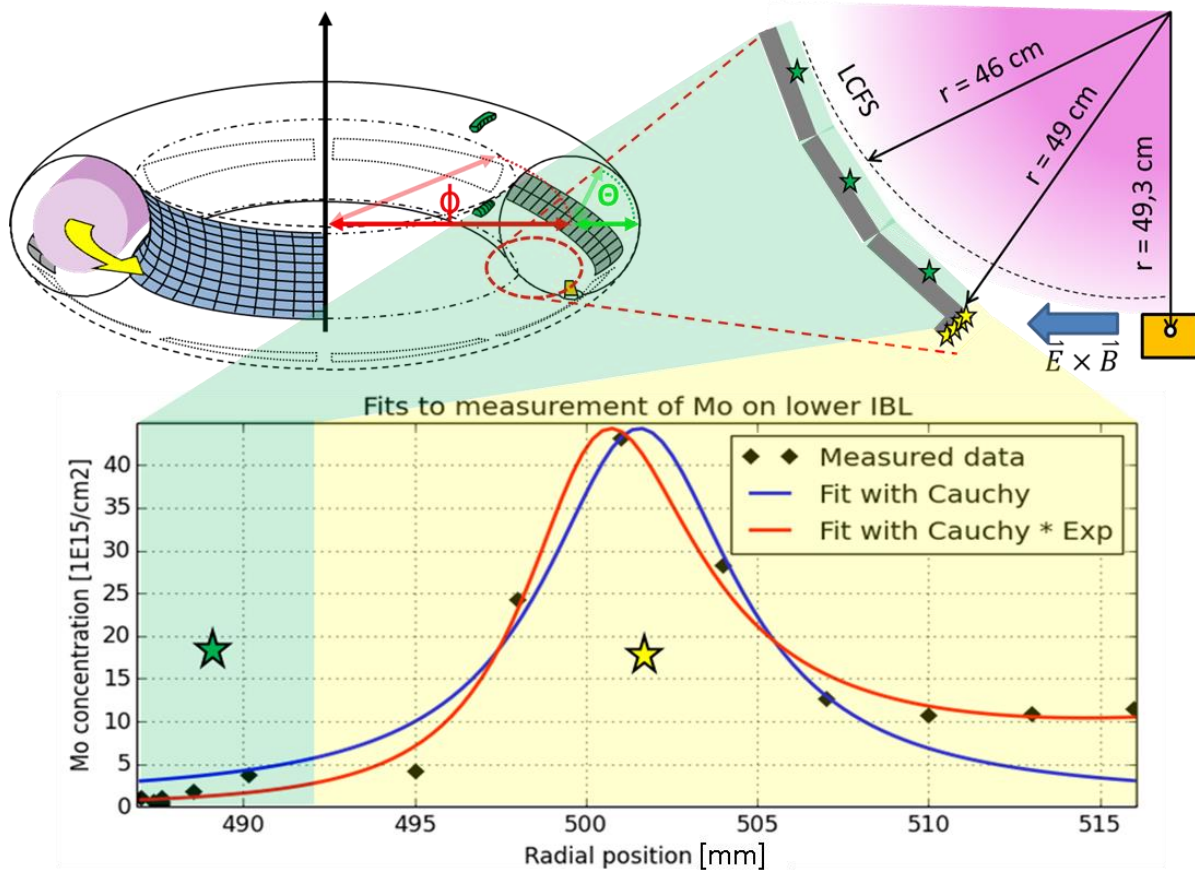
Figure 19: a) comparison of exponential and Cauchy distribution shows no qualitative difference in the profile; b) Equation 5 solved for different offsets between plasma column and IBL curvature centres.
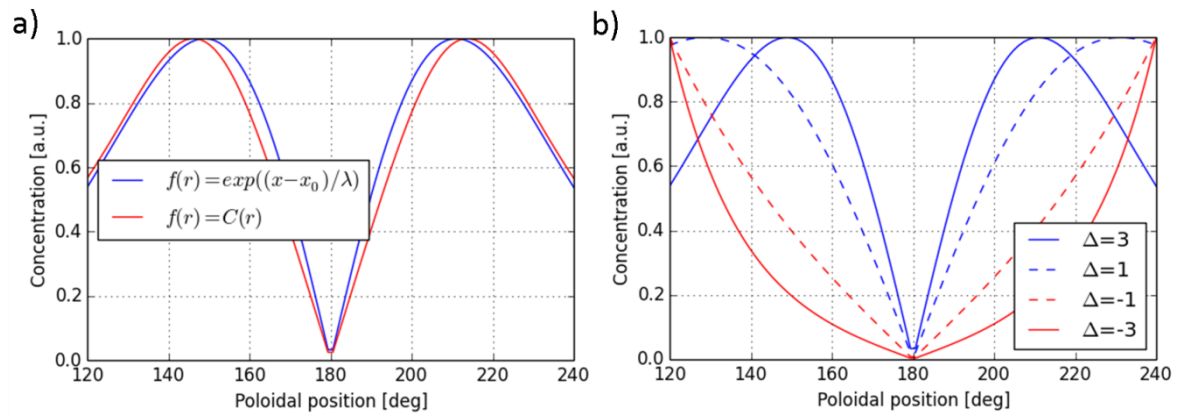
Figure 20: comparison between measured molybdenum concentration on the plasma-facing IBL tile sides, toroidally at the test limiter position, with Equation 5. Each tile was analysed at three different positions. The curves represent Equation 5 with Cauchy distribution (blue), Cauchy distribution and impact angle $\alpha \geq 1°$ (red) and exponential function and impact angle $\alpha \geq 1°$ (green).
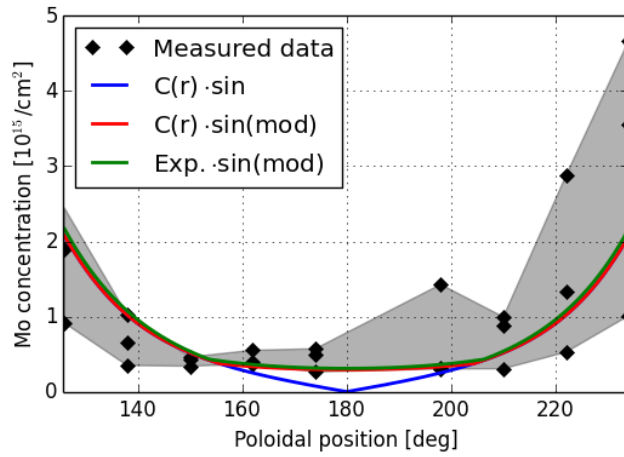
Figure 21: a) poloidal limiter geometry with the impact angle α at position r, furthermore with $\kappa = 6{,}5\ cm$ and $a = 48\ cm$; b) fit of Equation (6) to all poloidal limiter data from six stones, plotted over minor radius r with two different radial molybdenum distribution functions f(r). f(r)=C(r) yields better agreement with the data.
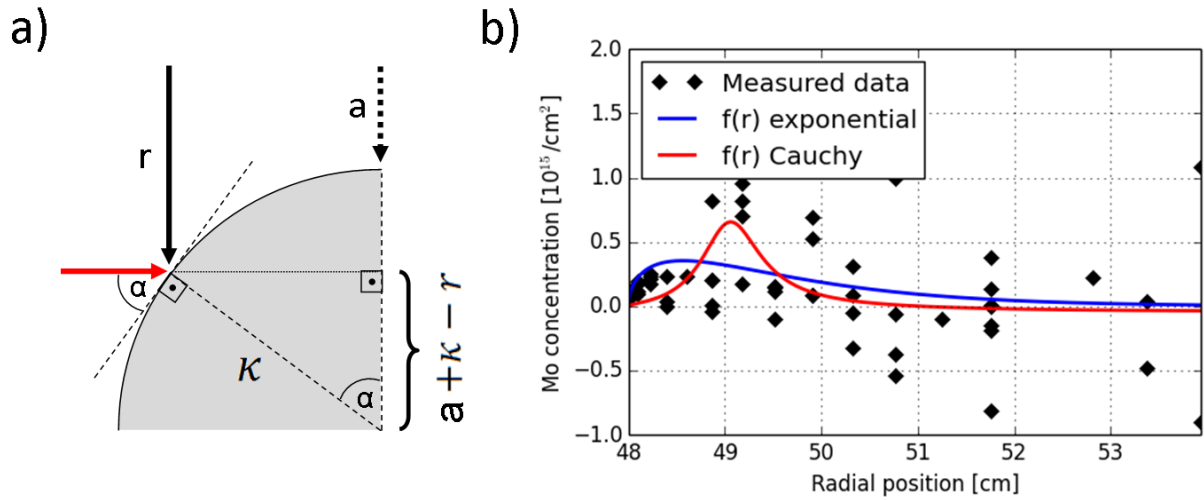
Figure 22: global tungsten deposition pattern. The IBL is the inner closed ring with the top towards the centre and the bottom towards the ALT-II. The black dot and cone denote the point of view for Fig. 23.
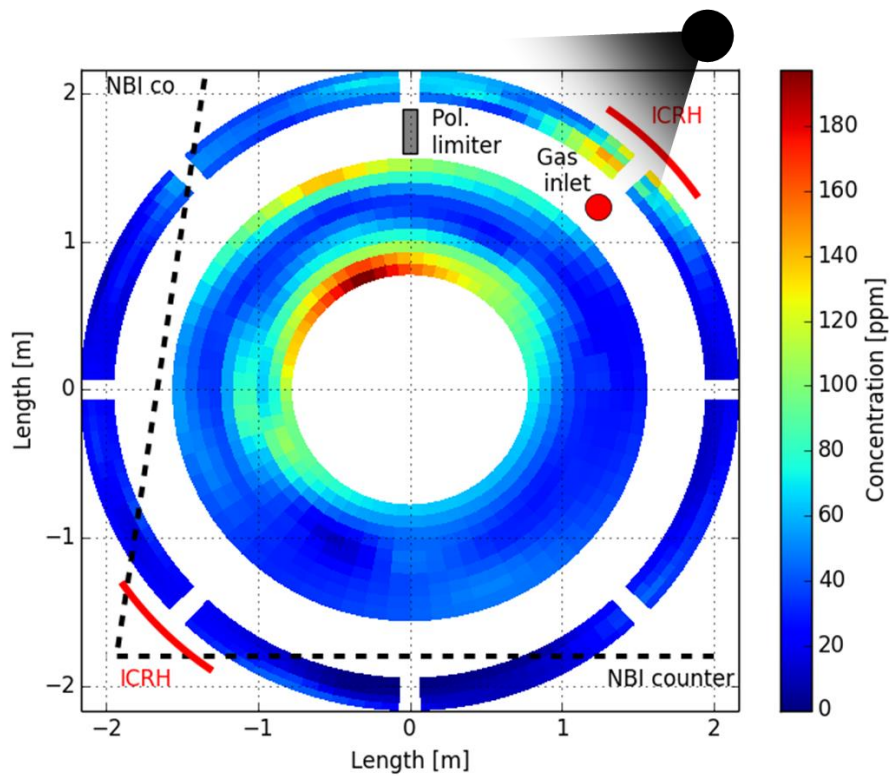
Figure 23: tungsten transport along poloidal flows (black solid arrows) from the poloidal limiter top (A), with minor contributions from the bottom (B), and from the test limiter (C). These PFCs were only covered in tungsten for dedicated experiments (see text and Table 3). Transport mostly took place along the solid arrow lines, with possible contributions from transport along the dashed arrow lines, towards the IBL top (1) and bottom (2), and from the test limiter mainly towards the ALT-II limiter (3). Sub-systems except the test limiter (red) and the poloidal limiter (blue) have been omitted for clarity. The point of view is illustrated in Fig. 22.
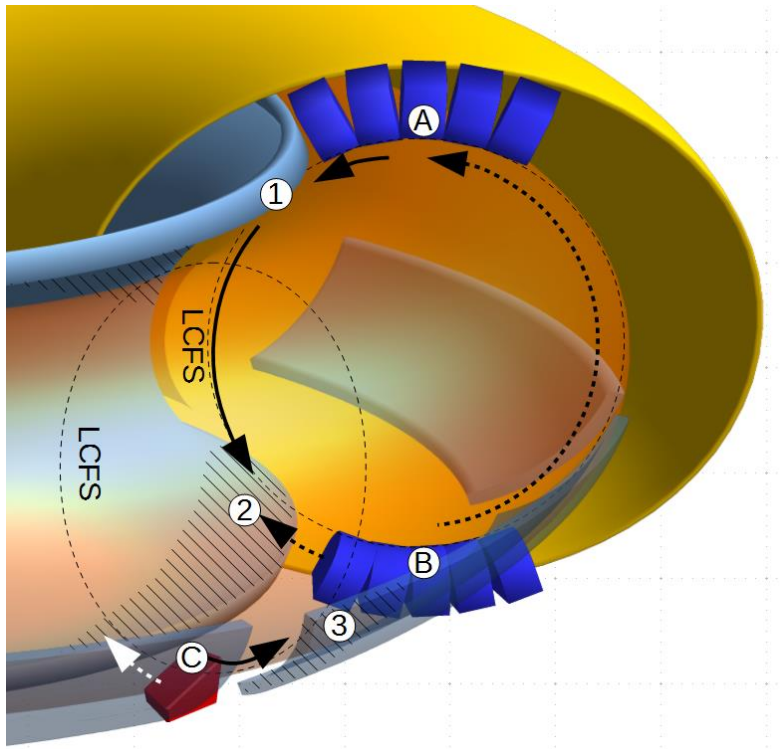
Figure 24: a) global medium-Z deposition pattern. The IBL is the inner closed ring with the top towards the centre and the bottom towards the ALT-II; b) metal deposition on the previous IBL (1994-2003) from [59] (rearranged and oriented), as obtained with beta backscattering. The white dashed lines indicate the directions of the neutral beams.
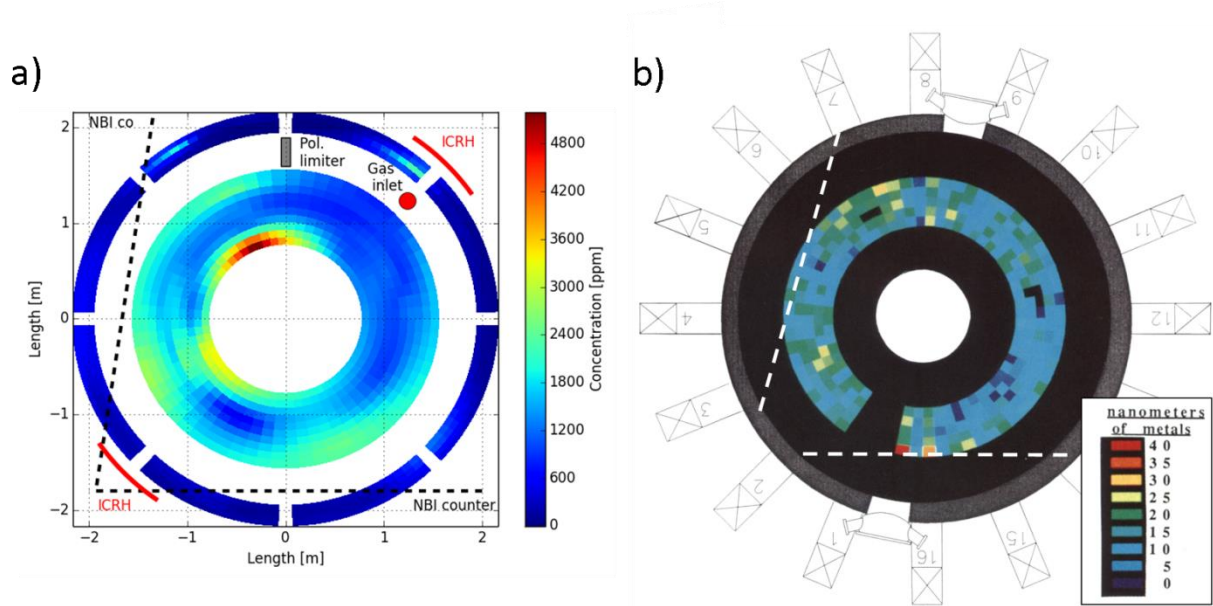
Figure 25: deposition of ^{15}N and F in toroidal direction on a) the ALT-II limiter and b) the IBL. Arrows indicate the toroidal position of the respective sources. The coloured areas are guides to the eye, giving an impression of the large scatter between measurements at same toroidal position, but different poloidal position.
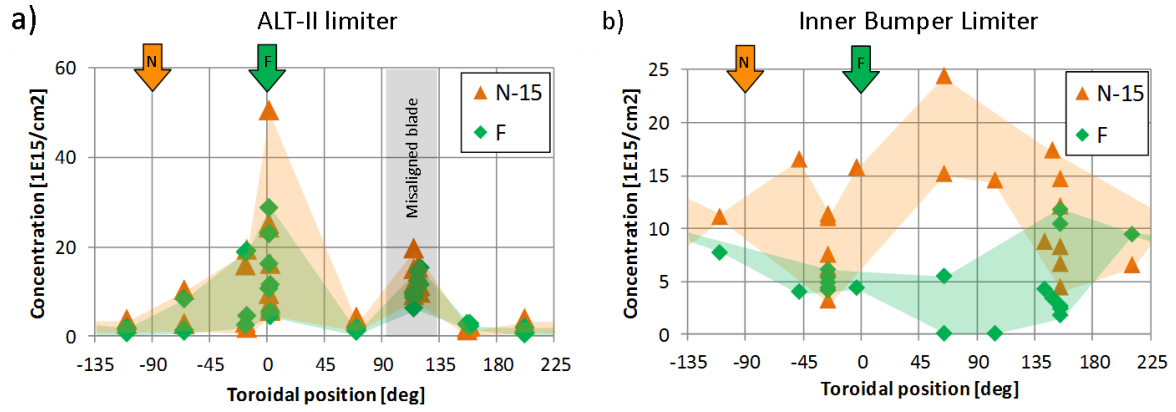
Figure 26: fuel retention – a) position of measured points, b) fuel retention pattern. The IBL is the inner closed ring with the top towards the centre and the bottom towards the ALT-II.
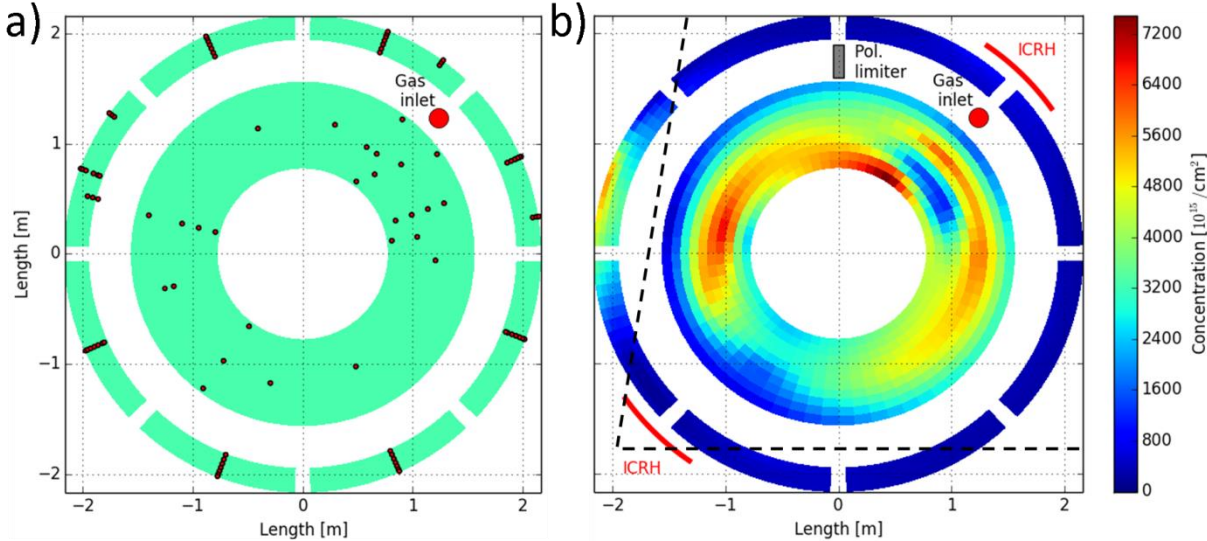
Figure 27: depth profiles and details on fuel retention on the ALT-II main limiter – a) depth
profiles from each blade, showing little qualitative variation except for one position with
metallic debris; b) fuel retention on Tile 21 of Blade 6 where the amount of debris was
highest, together with measurement positions; c) poloidal distribution of fuel retention on
each blade (except from Blade 3 and measured points at the debris of Blade 6), indicating flat
profiles apart from one outliner; d) modified Fig. 4e from [23], showing the flux onto the tiles
measured from each blade in Fig. 25c (red) with the line of analysis (yellow dashed).
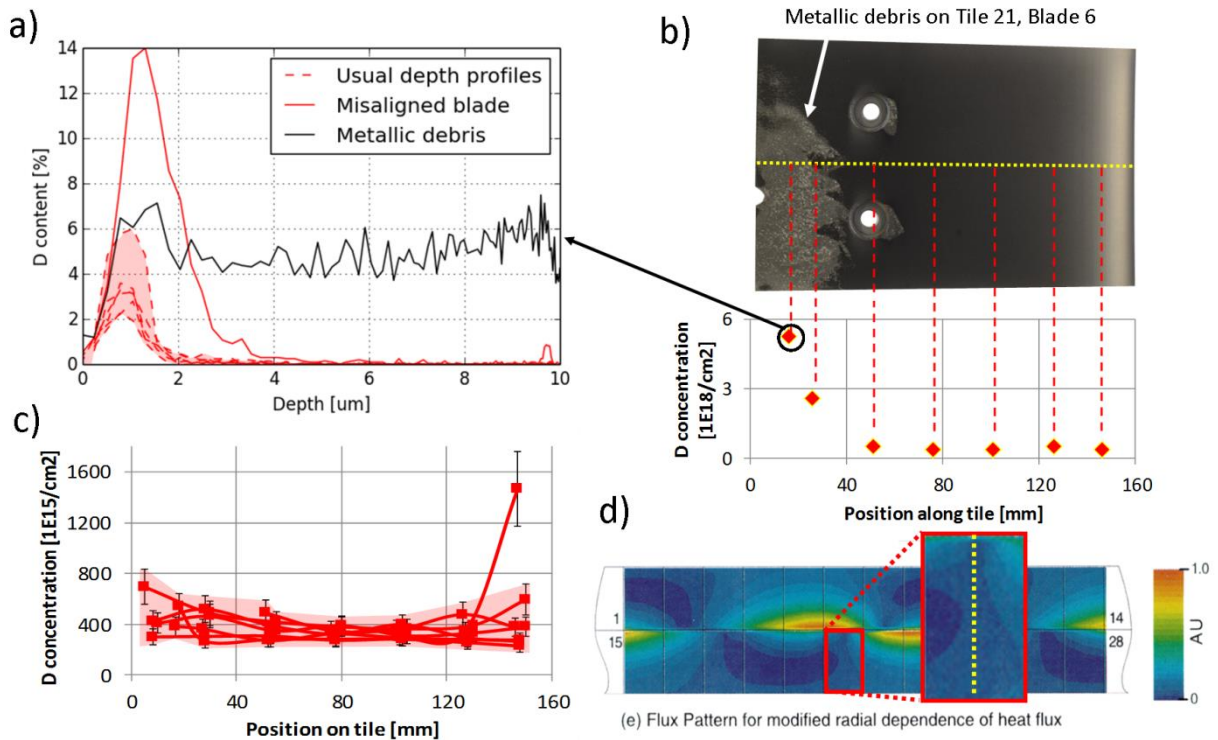
Figure 28: fuel retention on the IBL – a) depth profiles from different positions, showing large variation in the amount of retained fuel with respect to tile position and layer depth. Tiles 444 and 446 (black) are separated only by ca. 15 cm, yet showing large difference in fuel retention (black shaded area). The difference in fuel retention is smaller on the far side of the torus on tiles 71 and 76 (blue, blue shaded area). – b) width of surface concentration peaks may indicate the particle flux to different IBL areas, indicating large variation in particle flux to the walls. The peak widths at different poloidal positions (lines as guides for the eye) seem to follow the fuel retention in c) (arrows).
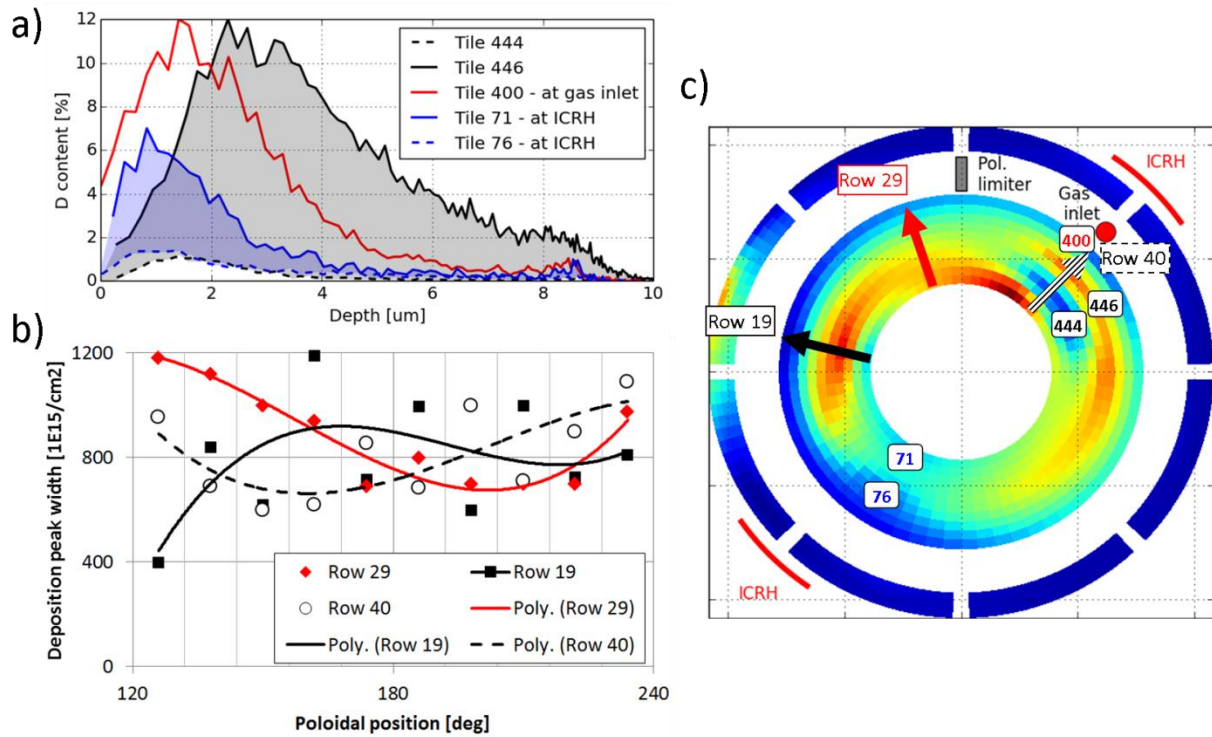
Figure 29: a) ERO simulation of molybdenum deposition on the test limiter with tenfold re-erosion yield (rearranged from Fig. 4 in [76]); b) experimental deposition as displayed in Fig. 10; c) ERO simulation without increased re-erosion yield, showing both quantitative and qualitative difference from experimental deposition (rearranged from Fig. 4 in [76]); d) comparison between ERO and experiment for the WF6 transport study in [27] (rearranged from Fig. 6 in [76]).
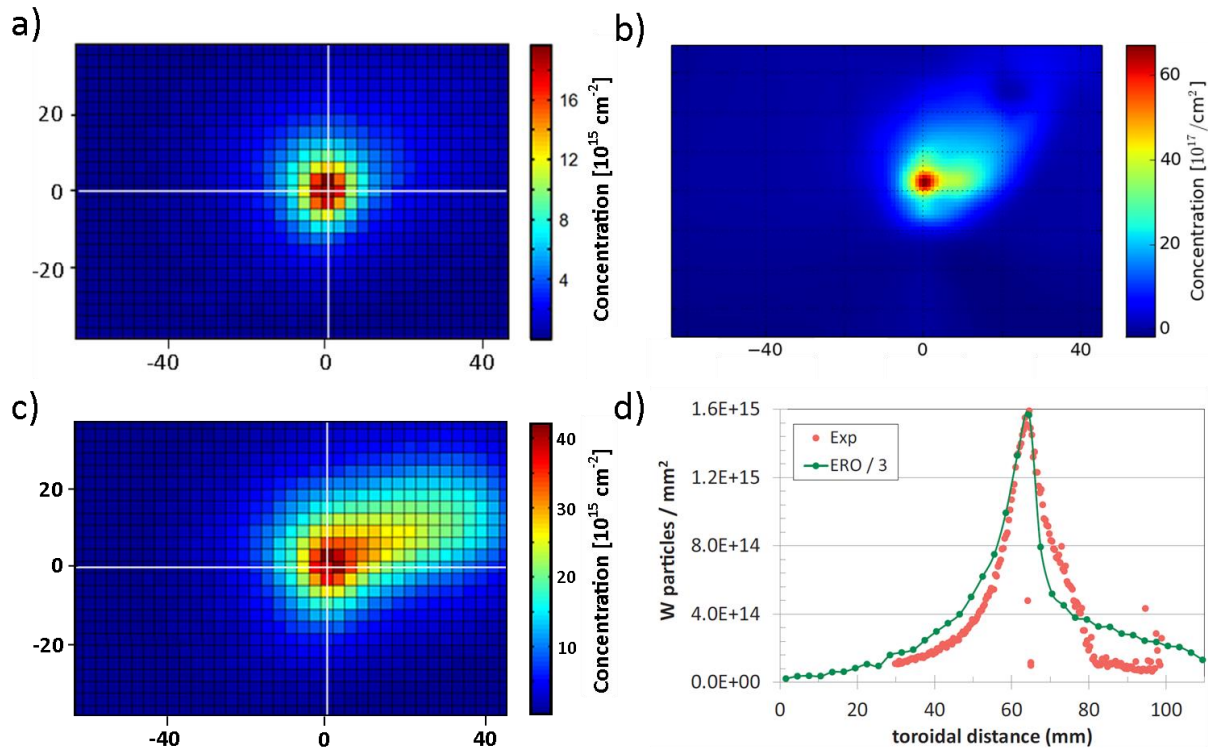
Figure 30: global ERO simulation to investigate the impact of diffusion on molybdenum deposition profiles – a) simulation environment with large extent in toroidal direction but very limited thickness in order to keep the simulation volume feasible for the local transport code ERO; b) resulting profiles for the two investigated diffusion constants D = 0,2 m²/s (realistic case, red) and D = 0,02 m²/s (reduced diffusion, black), yielding exponential decay with e-folding lengths of 15 and 130 cm, respectively.
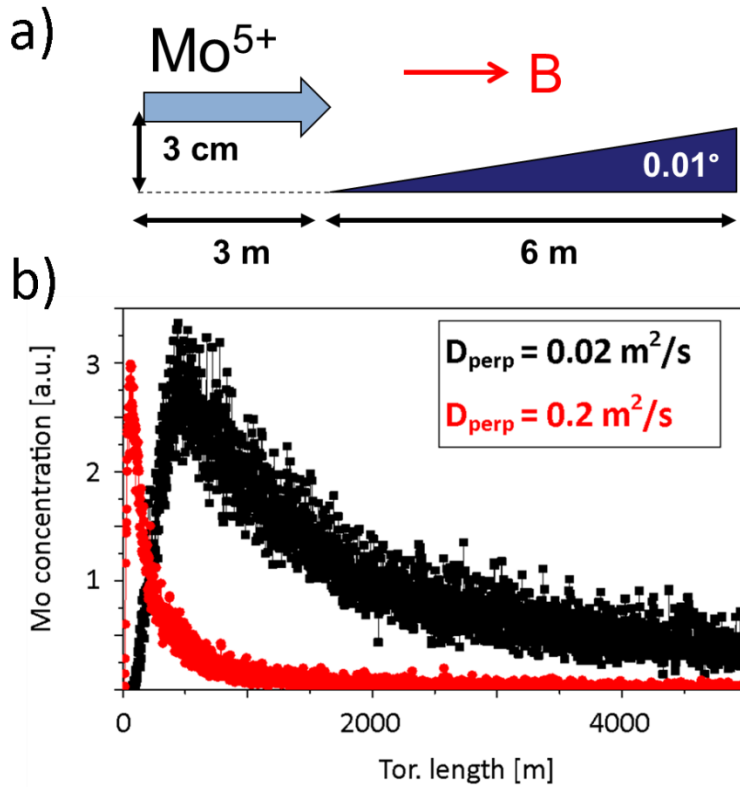
Figure 31: ASCOT input profiles (blue solid line), obtained by parabolic and polynomial fits to experimental data from various sources. Kreter *et al.* (2006) - [82], Kirschner *et al.* (2016) - [76], Moseev *et al.* (2011) - [83], Tammen Thesis - [43], Schweer *et al.* (1995) - [84], Koslowski, Soltwisch (1997) - [85], Coenen *et al.* (2010) - [44].
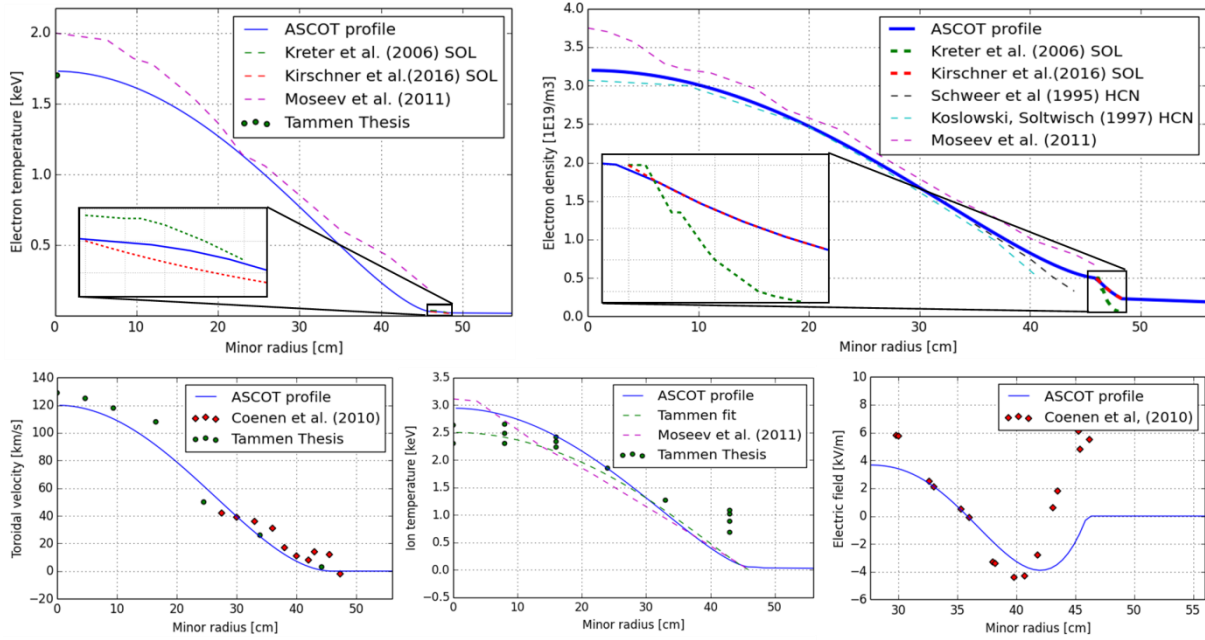
Figure 32: ASCOT simulation environment, fabricated with the help of CAD drawings, and with simulated molybdenum marker deposition: test Case (iv), see text and Figures 32d and 33. The test limiter with collector plate exhibits highest deposition (A), while only a few markers go to the liner (B). Furthermore, the HFS with IBL (C) and ALT-II (D) are visible. The poloidal limiter was not simulated.
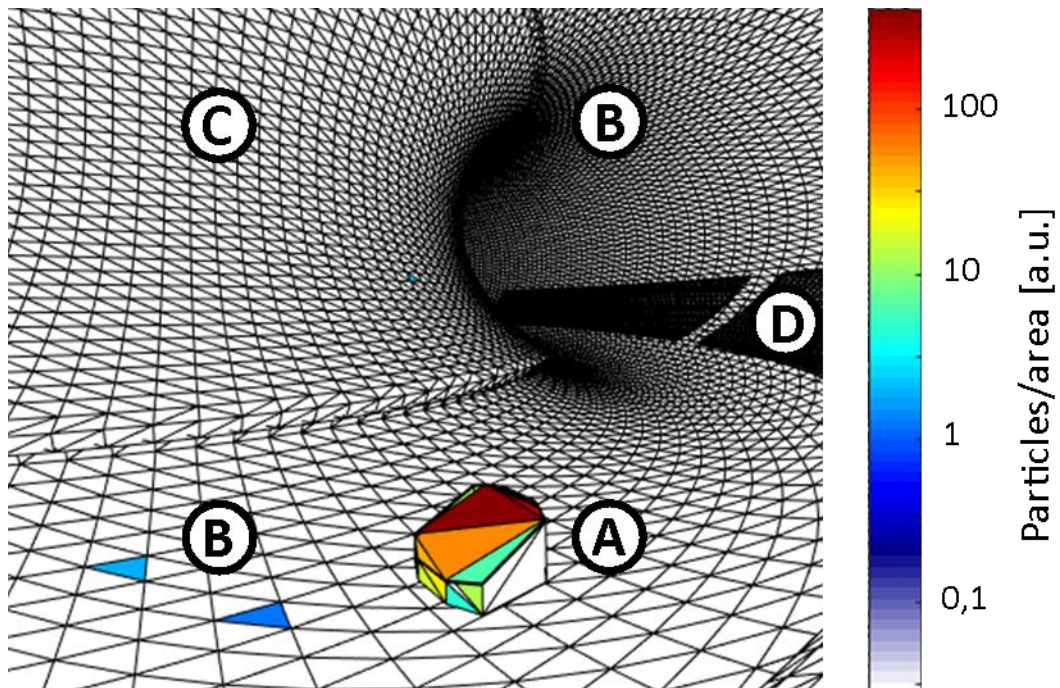
Figure 33: ASCOT deposition profiles projected in the poloidal plane (R, z – left, corresponds to point of view in plasma current direction) and locally on the collector plate as seen from the top (toroidal, poloidal – right, corresponds to top view) for the following cases: a) no interaction, just gyro motion; b) atomic interactions; c) Coulomb collisions; d) atomic and Coulomb collisions. On the left, the red diamond indicates the point source, while the grey shade in the two lower pictures indicates simulated structures. On the right pictures, the point source is at (0|0).
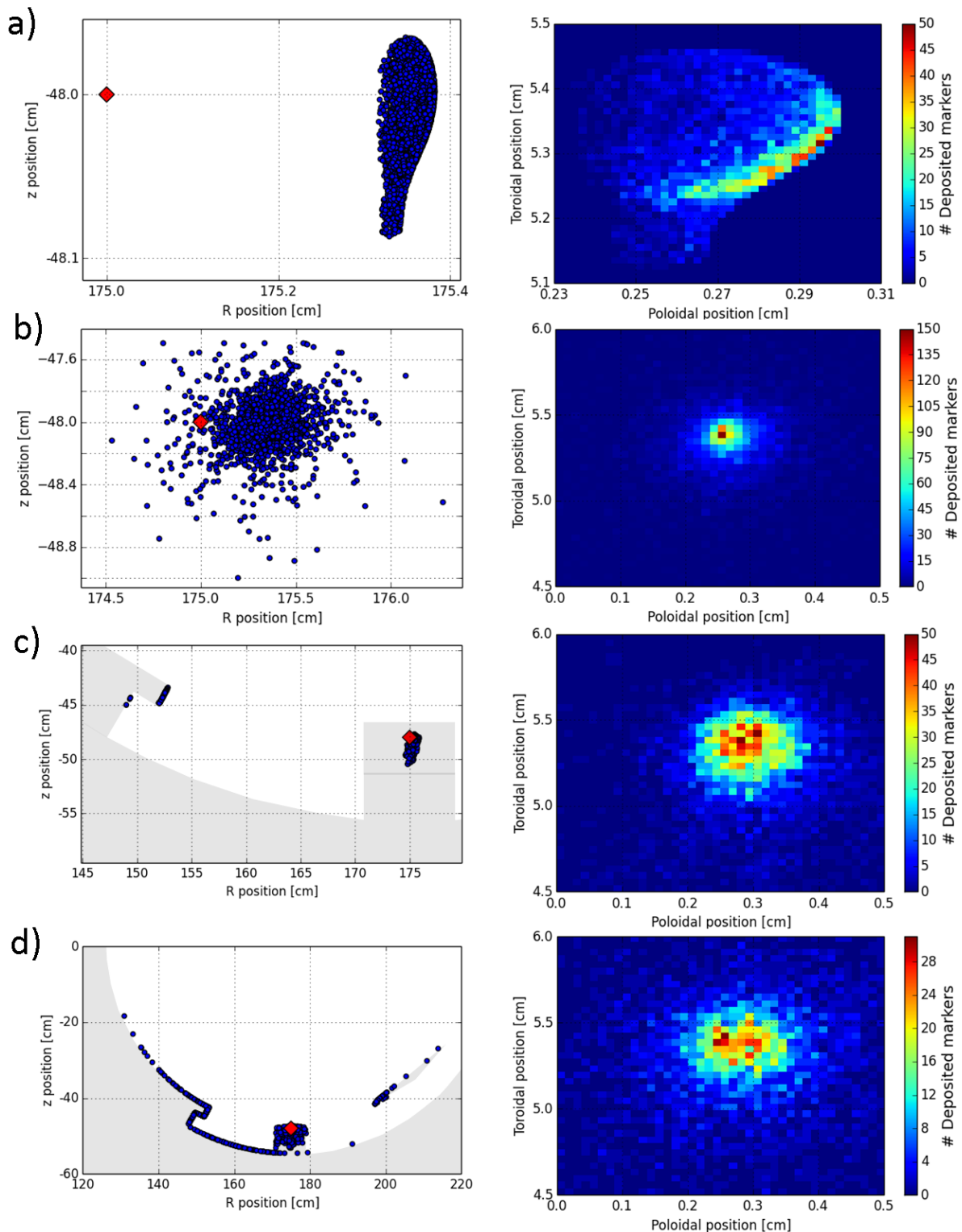
Figure 34: 3D plot of Case (iv) with both atomic and Coulomb collisions enabled (angled top view). The markers (blue dots) still follow the field line from their starting point (red) very closely until being deposited on the different limiters (black grid) and liner. Outside numbers are the ALT blade numbers while inside numbers denote the IBL column numbers. Marker starting point is between ALT blades 5 and 6 (lower right). Grid size: 1m×1m×1m.
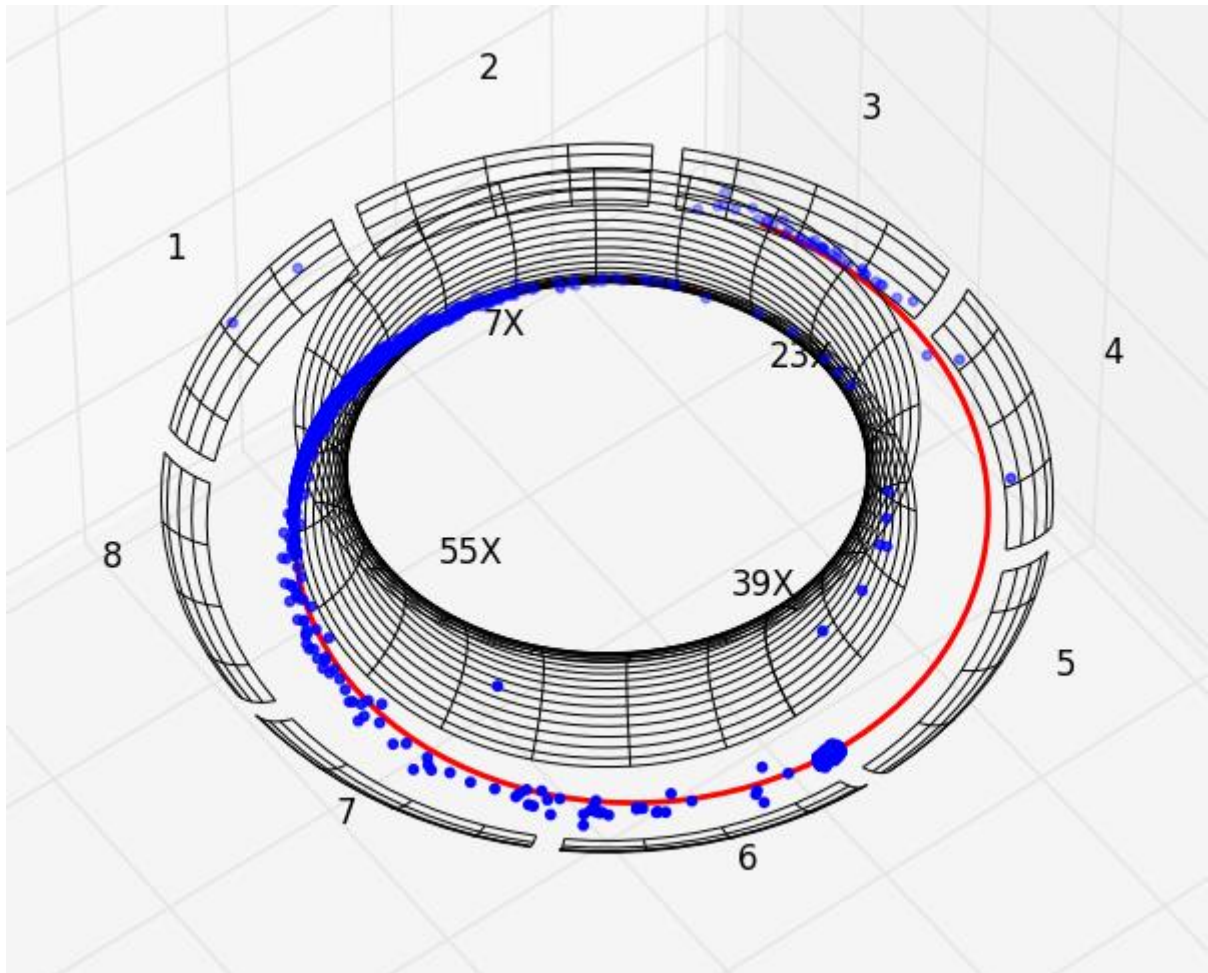
Figure 35: Full simulation cases with marker positions in blue as seen diagonally from the top (left) and with resulting deposition profile in arbitrary units (right) – a) without toroidal flow or radial electric field (Case I in Table 5), b) with both toroidal flow and radial electric field (Case IV), c) with all previously named physics plus extended source (Case V). Case I and II are qualitatively similar, Case III and IV as well as V and VI are almost identical.
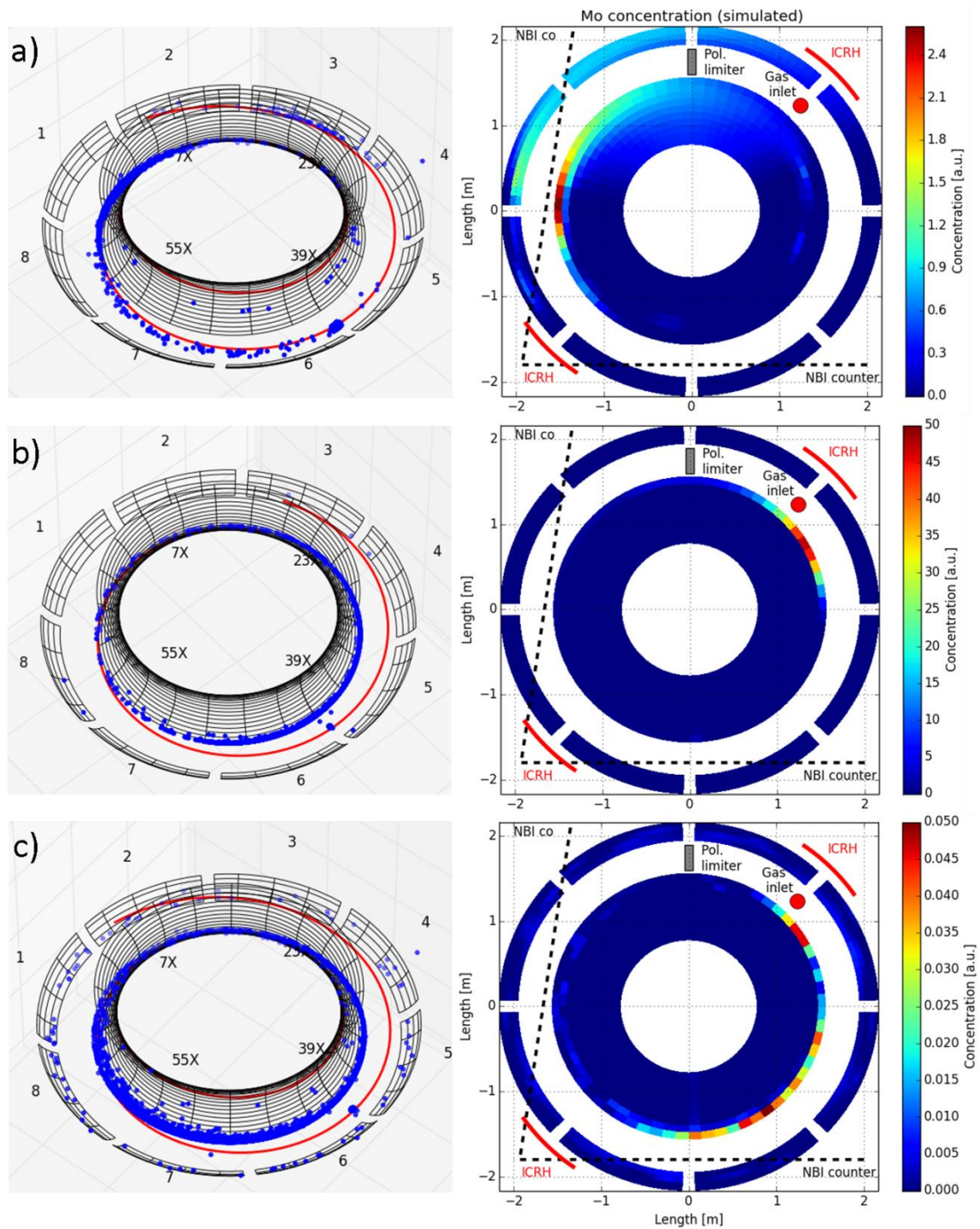
Figure 36: comparison between the interpolation of experimental (blue) and simulated (red, Case IV) deposition profiles on the bottom of the IBL. The form of the curve could be reproduced, quantitative agreement was not achieved, see text.
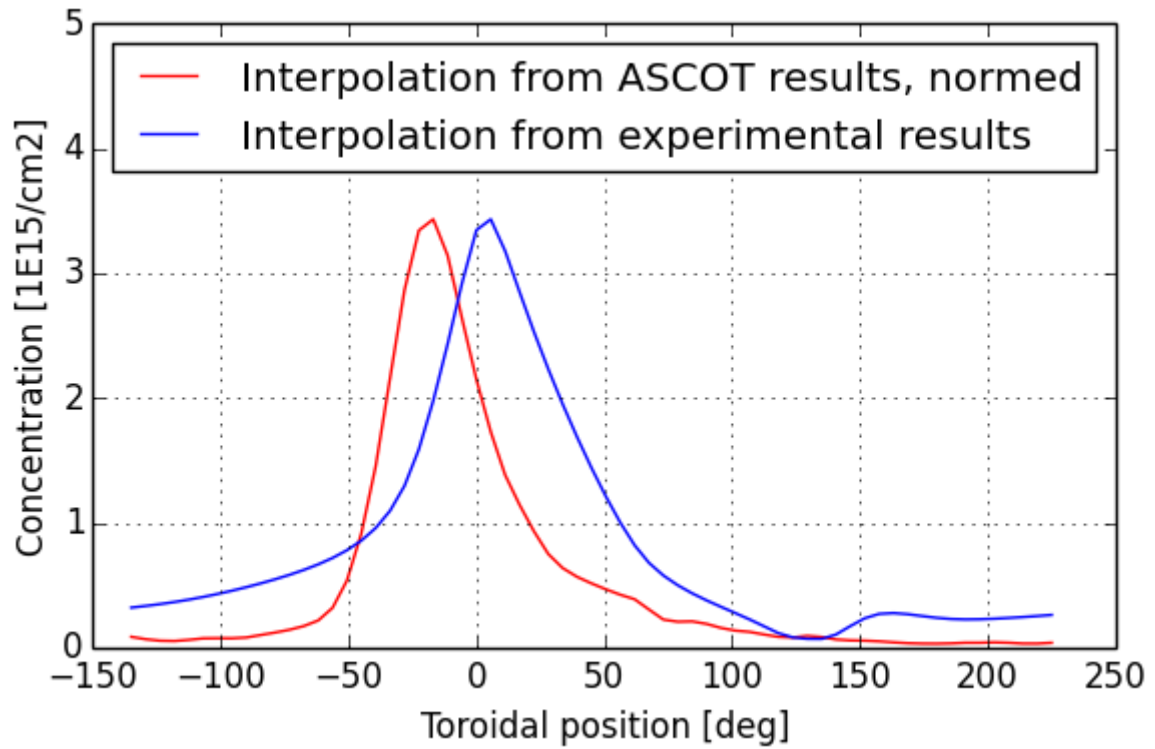
Table 1: Set of machine parameters of TEXTOR.

Type	Tokamak with carbon limiters
Operation period	1983 – 2013
Plasma size	R=1,75m; r=0,46m; V=7,3m^3
Magnetic field	Max. 3 T
Plasma current	Max. 800 kA
Discharge duration	Max. 10 s
Auxiliary heating	2×1,7 MW (co and counter NBI) 2×2 MW (ICRH antennae)

Table 2: Composition of Inconel 625 in weight and atomic %, according to [86]. Nickel serves as balance.

Element	Wt%	At%
Ni	Min. 58	Min. 58
Cr	20-23	Ca. 20,5
Fe	Max. 5	Max. 4,5
Mo	8-10	Ca. 4,7
Nb (+Ta)	3,15-5,15	Ca. 2
Co	Max. 1	0,8
Mn	Max. 0,5	0,5
Al	Max. 0,4	0,7
Ti	Max. 0,4	0,4
Si	Max. 0,5	0,9
C	Max. 0,1	0,4

Table 3: List of elements and isotopes in TEXTOR, their origin, literature (if available), and whether they were found during PFC analysis in this study. The list focuses on injections after the last major refurbishment in 1994 where the DED was installed together with the IBL which was investigated in this study.

Species	Origin	Literature	Found?
D	Plasma (homogeneous) GD cleaning Ion cyclotron wall conditioning Boronisation/siliconisation	[87] [88] [87]	Yes Yes[1] Yes[1] Yes[1]
He	GD cleaning Ion cyclotron wall conditioning (Rutherford Scattering beam)	[87] [89], [88] [43]	Yes[2]
Li	Li beam	[90]	Yes[3]
B	Boronisation	[87]	Yes
C	Limiters		Yes
N	Air, plasma edge cooling experiments	[30]	Yes
^{15}N	Plasma edge cooling experiments	[27], [91], this paper	Yes
O	Air, water		Yes
^{18}O	Ion cyclotron wall conditioning	[88]	No
F	Hexafluoride injection	[27], [92], this paper	Yes

Ne	Plasma edge cooling experiments	[30], [93], [94]	Unclear
Na	Shutdown work?		Yes
Al	Cover during test limiter experiments	[95]	Unclear
Si	Siliconsiation	[87]	Yes
	Si_4D injection through test limiter	[42]	No
Cl	Shutdown work?		Yes
Ar	Plasma edge cooling experiments	[96], [97], [98]	Yes
Inconel, stainless steel	Liner, struct. components of ALT-II, ICRH Faraday shields,	[18]	Yes Unclear
	Test limiter experiments (LL1)	[42]	Unclear
	Test limiter experiments (LL3)	[99]	Unclear
Cu	NBI scraper	[16]	Unclear
	Poloidal limiter experiments for W7X	[57]	Yes
	Test limiter experiments	[42]	Unclear
Mo	Mo test limiter experiments	[41], [53], [41]	Yes
	Inconel components		Yes
	MoF_6 injection through test limiter	This paper	Yes
Ta	Collector probe cap (see Fig. 1a)	[12]	No
W	W poloidal limiter experiments	[52], [55]	Yes
	W test limiter experiments	[41], [53], [55], [56], [92], [100]	Yes
	WF_6 injection through test limiter	[27]	Unclear
	WF_6 for calibration	[92]	Unclear
Re	Layer erosion at test limiters	[95]	No
	Interlayer on poloidal limiters	[52]	Unclear

[1] D from the respective sources cannot be distinguished from other sources, but both GD and ICRH antennae have an impact on the deuterium deposition profile, as will be seen later.

[2] He was found all around the vessel, but no link to the actual source can be drawn, neither to the impact of sub-systems, contrary to deuterium.

[3] See [34].

Table 4: e-folding lengths of exponential concentration decay in toroidal direction for molybdenum and tungsten (first published in [50]). The e-folding lengths in co- and counter-direction (i.e. with or against the plasma current direction under normal configuration) have different values and are given separately. Errors for e-folding length estimations are given in parentheses.

PFC	Mo (co) [cm]	Mo (counter) [cm]	W (co) [cm]	W (counter) [cm]
ALT-II limiter	12(5)	26(7)	52(12)	35(9)
IBL (top)	103(21)	66(14)	179(40)	155(34)
IBL (bottom)	105(21)	84(18)	124(28)	166(37)

Table 5: full ASCOT simulation cases, with the included physics listed.

	Kind of source	Electric field?	Tor. rotation?	Starting energy
Case I	Point	No	No	1 eV
Case II	Point	No	Yes	1 eV

Case III	Point	Yes	No	1 eV
Case IV	Point	Yes	Yes	1 eV
Case V	Radial Cauchy (Fig. 10b)	Yes	Yes	1 eV
Case VI	Radial Cauchy (Fig. 10b)	Yes	Yes	10 eV

Bibliography

[1] G. Federici, C. H. Skinner, J. N. Brooks, J. P. Coad, C. Grisolia, A. A. Haasz, A. Hassanein, V. Philipps, C. S. Pitcher, J. Roth, W. R. Wampler and D. G. Whyte, "Plasma-material interactions in current tokamaks and their implications for next step fusion reactors," *Nuclear Fusion,* vol. 41, no. 12R, pp. 1967-2137, 2001.

[2] D. Naujoks, Plasma-Material Interaction in Controlled Fusion, Springer Verlag Berlin Heidelberg, 2006.

[3] J. Roth and e. al., "Recent analysis of key plasma wall interactions issues for ITER," *Journal of Nuclear Materials,* Vols. 390-391, pp. 1-9, 2009.

[4] D. Naujoks and R. Behrisch, "Erosion and redeposition at the vessel walls in fusion devices," *Journal of Nuclear Materials,* Vols. 220-222, pp. 227-230, 1995.

[5] A. Raffray, R. Nygren, D. Whyte, S. Abdel-Khalik, R. Doerner, F. Escourbiac, T. Evans, R. Goldston, D. Hoelzer, S. Konishi, P. Lorenzetto, M. Merola, R. Neu, P. Norajitra, R. Pitts, M. Rieth, M. Roedig, T. Rognlien, S. Suzuki, M. Tillack and C. Wong, "High heat flux components - Readiness to proceed from near term fusion systems to power plants," *Fusion Engineering and Design,* vol. 85, pp. 93-108, 2010.

[6] J. Wesson, "Impurity radiation," in *Tokamaks*, Oxford, Oxford University Press, 2004, pp. 229-231.

[7] T. Pütterich, R. Neu, R. Dux, A. Whiteford, M. O'Mullane, H. Summers and A. U. Team, "Calculation and experimental test of the cooling factor of tungsten," *Nuclear Fusion,* vol. 50, p. 025012, 2010.

[8] M. Z. Tokar, J. Rapp, G. Bertschinger, L. Könen, H. R. Koslowski, A. Krämer-Flecken, V. Philipps, U. Samm and B. Unterberg, "Nature of high-Z impurity accumulation in tokamaks," *Nuclear Fusion,* vol. 37, no. 12, pp. 1691-1708, 1997.

[9] B. Schweer, S. Brezinsek, H. G. Esser, A. Huber, P. Mertens, S. Musso, V. Philipps, A. Pospieszczyk, U. Samm, G. Sergienko and P. Wienhold, "Limiter Lock systems at TEXTOR: Flexible tools for plasma-wall investigation," *Fusion Science and Technology,* vol. 47, pp. 138-145, 2005.

[10] S. Brezinsek, G. Sergienko, A. Pospieszczyk, P. Mertens, U. Samm and P. T. Greenland, "Characterization of the deuterium recycling flux in front of a graphite surface in the TEXTOR

tokamak," *Plasma Physics and Controlled Fusion,* vol. 47, pp. 615-634, 2005.

[11] D. Larsson and M. Rubel, "Ion flux measurements with the improved collector probe system at the TEXTOR-94 tokamak," *Review of Scientific Instruments,* vol. 69, no. 7, pp. 2671-2674, 1998.

[12] B. Schweer, P. Wienhold, M. Rubel, B. Emmoth and R. Zagórski, "Fast reciprocating probe system for plasma edge characterisation: construction and applications," in *1st German-Polish Euro-Conference on Plasma Diagnostics for Fusion and Applications (GPPD)*, Greifswald, Germany, 2002.

[13] R. W. Conn, K. H. Dippel, W. B. Gauster and A. Miyahara, "The toroidal belt pump limiter, ALT-II, in the TEXTOR tokamak," *Fusion Engineering and Design,* vol. 13, pp. 251-259, 1990.

[14] M. Rubel, S. Brezinsek, J. W. Coenen, A. Huber, A. Kirschner, A. Kreter, P. Petersson, V. Philipps, A. Pospieszczyk, B. Schweer, G. Sergienko, T. Tanabe, Y. Ueda and P. Wienhold, "Overview of wall probes for erosion and deposition studies in the TEXTOR tokamak," *Matter and Radiation at Extremes,* vol. 2, pp. 87-104, 2017.

[15] O. Neubauer, G. Cyzmek, B. Giesen, P. W. Hüttemann, M. Sauer, W. Schalt and J. Schruff, "Design features of the tokamak TEXTOR," *Fusion Science and Technology,* vol. 47, no. 2, pp. 76-86, 2005.

[16] U. Pfister, "TEXTOR neutral beam injection system (NBI)," in *Fusion Technology 1986, Proceedings of the Fourteenth Symposium*, Avignon, 1986.

[17] H. Euringer, M. Lochter, U. Pfister and R. Uhlemann, "Neutral injection for TEXTOR," in *IEEE Thirteenth Symposium on Fusion Engineering*, Knoxville, 1989.

[18] W. Kohlhaas, C. Stickelmann, B. Brandt and F. Durodié, "New liner and ICRH antennae; Integration of ALT-II in TEXTOR," *Fusion Engineering and Design,* vol. 13, pp. 321-336, 1990.

[19] E. Westerhof and e. al., "Electron cyclotron resonance heating on TEXTOR," *Fusion Science and Technology,* vol. 47, pp. 108-118, 2005.

[20] B. Giesen, H. Bohn, W. Huettemann, O. Neubauer, M. Poier and W. Schalt, "Technical lay-out of the dynamic ergodic divertor," *Fusion Engineering and Design,* vol. 37, pp. 341-346, 1997.

[21] B. Emmoth, P. Wienhold, M. Rubel, B. Schweer and R. Zagórski, "Particle collection at the plasma edge by a fast reciprocating probe at the TEXTOR tokamak," *Journal of Nuclear Material,* Vols. 313-316, pp. 729-733, 2003.

[22] D. M. Goebel, R. W. Conn, W. J. Corbett, K. H. Dippel, K. H. Finken, W. B. Gauster, A. Hardtke, J. A. Koski, W. Kohlhaas, R. T. McGrath, M. E. Malinowski, A. Miyahara, R. Moyer, A. Sagara, J. G. Watkins and G. Wolf, "ALT-II toroidal belt pump limiter performance in TEXTOR," *Journal of Nuclear Materials,* Vols. 162-164, pp. 115-127, 1989.

[23] T. Denner, K. H. Finken, G. Mank and N. Noda, "Thermal load distribution near the tips of the

ALT-II limiter roof on TEXTOR-94," *Nuclear Fusion,* vol. 39, no. 1, pp. 83-94, 1999.

[24] J. A. Koski and R. D. Watson, "Engineering design and analyses of the ALT-II particle collection scoops and deflector plates," *Fusion Engineering and Design,* vol. 13, pp. 291-298, 1990.

[25] M. J. Rubel, E. Fortuna, A. Kreter, E. Wessel, V. Philipps and K. J. Kurzydlowski, "Overview of comprehensive characterisation of erosion zones on plasma facing components," *Fusion Engineering and Design,* vol. 81, pp. 211-219, 2006.

[26] A. Weckmann, P. Petersson, M. Rubel, P. Wienhold, S. Brezinsek, J. W. Coenen, A. Kirschner, A. Kreter and A. Pospieszczyk, "Local migration studies of high-Z metals in the TEXTOR tokamak," *Physica Scripta,* vol. T167, p. 014058, 2016.

[27] M. Rubel, J. Coenen, D. Ivanova, S. Möller, P. Petersson, S. Brezinsek, A. Kreter, V. Philipps, A. Pospieszczyk and B. Schweer, "Tungsten migration studies by controlled injection of volatile compounds," *Journal of Nuclear Materials,* vol. 438, pp. 170-174, 2013.

[28] M. Rubel, A. Weckmann, P. Ström, P. Petersson, A. Garcia-Carrasco, S. Brezinsek, J. Coenen, A. Kreter, S. Möller, P. Wienhold and E. F.-Z. T. Wauters, "Tracer techniques for the assessment of material migration and surface modification of plasma-facing components," *Journal of Nuclear Materials,* vol. 463, pp. 280-284, 2015.

[29] A. Pospieszczyk, D. Borodin, S. Brezinsek, A. Huber, A. Kirschner, P. Mertens, G. Sergienko, B. Schweer, I. L. Beigman and L. Vainshtein, "Determination of rate coefficients for fusion-relevant atoms and molecules by modelling and measurement in the buondary layer of TEXTOR," *Journal of Physics B: Atomic, Molecular and Optical Physics,* vol. 43, no. 14, 2010.

[30] M. Rubel, V. Philipps, L. Marot, P. Petersson, A. Pospieszczyk and B. Schweer, "Nitrogen and neon retention in plasma-facing materials," *Journal of Nuclear Materials,* vol. 415, pp. 223-226, 2011.

[31] S. Brezinsek, T. Loarer, K. Krieger, S. Jachmich, M. Tsalas, I. Coffey, H. Esser, T. Eich, W. Fundamenski, C. Giroud, S. Grünhagen, A. Huber, U. Kruezi, S. Knipe, G. Maddison, K. McCormick, A. Meigs, P. Morgan, V. Philipps, G. Sergienko and R. Stagg, "Fuel retention in impurity seeded discharges in JET after Be evaporation," *Nuclear Fusion,* vol. 51, p. 073007, 2011.

[32] M. Oberkofler, D. Douai, S. Brezinsek, J. Coenen, T. Dittmar, A. Drenik, S. Romanelli, E. Joffrin, K. McCormick, M. Brix, G. Calabro, M. Clever, C. Giroud, U. Kruezi, K. Lawson, C. Linsmeier, A. M. Rojo, A. Meigs, S. Marsen, R. Neu and M. Reinelt, "First nitrogen-seeding experiments in JET with ITER-like Wall," *Journal of Nuclear Materials,* vol. 438, pp. 258-261, 2013.

[33] E. Fortuna-Zalesna, A. Weckmann, J. Grzonga, M. Rubel, H. G. Esser, M. Freisinger, A. Kreter, G. Sergienko and P. Ström, "Dust survey following the final shutdown of TEXTOR: metal particles and fuel retention," *Physica Scripta,* vol. T167, p. 014059, 2016.

[34] A. Weckmann, P. Petersson, M. Rubel, E. Fortuna-Zalesna, W. Zielinski, B. Romelczyk-Baishya,

E. Grigore, C. Ruset and A. Kreter, "Ageing of structural materials in tokamaks: TEXTOR liner study," *Physica Scripta,* vol. T170, p. 014053, 2017.

[35]   M. Mayer, "SIMNRA," Max-Planck-Institut für Plasmaphysik, August 2017. [Online]. Available: http://home.mpcdf.mpg.de/~mam/. [Accessed 9 October 2017].

[36]   H. J. Whitlow, G. Possnert and C. S. Petersson, "Quantitative mass and energy dispersive elastic recoil spectrometry: Resolution and efficiency considerations," *Nuclear Instruments and Methods in Physics Research,* vol. B27, pp. 448-457, 1987.

[37]   P. Ström, P. Petersson, M. Rubel and G. Possnert, "A combined segmented anode gas ionization chamber and time-of-flight detector for heavy ion elastic recoil detection analysis," *Review of Scientific Instruments,* vol. 87, p. 103303, 2016.

[38]   M. Adel, O. Amir, R. Kalish and L. Feldman, "Ion-beam-induced hydrogen release from a-C:H: A bulk molecular recombination model," *Journal of Applied Physics,* vol. 66, no. 7, pp. 3248-3251, 1989.

[39]   B. J. C. Baxter, "The interpolation theory of radial basis functions," Cambridge University, Cambridge, 1992.

[40]   L. Råde and B. Westergren, Mathematics Handbook for Science and Engineering, Berlin, Heidelberg: Springer, 1999.

[41]   A. Kreter, P. Wienhold, D. Borodin, S. Brezinsek, S. Droste, T. Hirai, A. Kirschner, V. P. A. P. A. Litnovsky, U. Samm, O. Schmitz, G. Sergienko and T. Team, "Study of local carbon transport on graphite, tungsten and molybdenum test limiters in TEXTOR by (CH4)-C-13 tracer injection," *Journal of Nuclear Materials,* vol. 363, pp. 179-183, 2007.

[42]   J. W. F. Weschenfelder, U. Kögler, H. Esser, V. Philipps, A. Pospieszczyk, B. Schweer, J. Seggern, M. Tokar and P. Wienhold, "Investigation of transport processes close to limiter surfaces in TEXTOR-94," *Plasma Physics and Controlled Fusion,* vol. 38, pp. A311-A323, 1996.

[43]   H. F. Tammen, *The ion velocity distribution of tokamak plasmas: Rutherford Scattering at TEXTOR,* Utrecht, 1995.

[44]   J. Coenen, B. Schweer, M. Clever, S. Freutel, O. Schmitz, H. Stoschus, U. Samm, B. Unterberg and T. team, "Charge exchange recombination spectroscopy on a diagnostic hydrogen beam - measuring impurity rotation and radial electric field at the tokamak TEXTOR," *Journal of Physics B: Atomic, Molecular and Optical Physics,* vol. 43, p. 144015, 2010.

[45]   J. Coenen, O. Schmitz, B. Unterberg, M. Clever, M. Jakubowski, U. Samm, B. Schweer, H. Stoschus, M. Tokar and T. Team, "Rotation and radial electric field in the plasma edge with resonant magnetic perturbation at TEXTOR," *Nuclear Fusion,* vol. 51, p. 063030, 2011.

[46]   M. Lehnen, M. Brix, H. Gerhauser, B. Schweer and R. Zagórski, "Investigations on density and temperature asymmetries due to drift motions in the boundary layer of TEXTOR-94," *Journal of*

Nuclear Materials, Vols. 290-293, pp. 663-667, 2001.

[47] M. Mayer, V. Philipps, P. Wienhold, H. G. Esser, J. v. Seggern and M. Rubel, "Hydrogen inventories in nuclear fusion devices," *Journal of Nuclear Materials,* Vols. 290-293, pp. 381-388, 2001.

[48] M. Rubel, P. Wienhold and D. Hildebrandt, "Fuel accumulation in co-deposited layers on plasma facing components," *Journal of Nuclear Materials,* Vols. 290-293, pp. 473-477, 2001.

[49] M. Lehnen, M. Brix, U. Samm, B. Schweer and B. Unterberg, "Plasma edge transport phenomena caused by particle drifts and sources in TEXTOR," *Nuclear Fusion,* vol. 43, no. 3, pp. 168-178, 2003.

[50] A. Weckmann, P. Petersson, A. Kirschner, P. Wienhold, S. Brezinsek, A. Kreter, A. Pospieszczyk and M. Rubel, "Whole-machine material migration studies in the TEXTOR tokamak with molybdenum," *Nuclear Materials and Energy,* vol. 12, pp. 518-523, 2017.

[51] P. C. Stangeby, The Plasma Boundary of Magnetic Fusion Devices, Bristol: IOP Publishing, 2000.

[52] A. Pospieszczyk, T. Tanabe, V. Philipps, G. Sergienko, T. Ohgo, K. Kondo, M. Wada, M. Rubel, W. Biel, A. Huber, A. Kirschner, J. Rapp and N. Noda, "Operation of TEXTOR-94 with tungsten poloidal main limiters," *Journal of Nuclear Materials,* Vols. 290-293, pp. 947-952, 2001.

[53] M. Rubel, V. Philipps, U. Kögler, T. Tanabe, D. Larsson, B. Unterberg, A. Pospieszczyk, Y. Ueda and P. Wienhold, "Impact of molybdenum and tungsten test limiters on ion fluxes in the plasma edge of TEXTOR," *Journal of Nuclear Materials,* vol. 249, no. 2-3, pp. 116-120, 1997.

[54] G. Sergienko, B. Bazylev, T. Hirai, A. Huber, A. Kreter, P. Mertens, A. Nedospasov, V. Philipps, A. Pospieszczyk, M. Rubel, U. Samm, B. Schweer, P. Sundelin, M. Tokar, W. Wessel and T. team, "Experience with bulk tungsten test-limiters under high heat loads: melting and melt layer propagation," *Physica Scripta,* vol. T128, pp. 81-86, 2007.

[55] M. Wada, T. Tanabe, V. Philipps, B. Unterberg, A. Pospieszczyk, B. Schweer, J. Rapp, Y. Ueda, K. Ohya, T. Ohgo and N. Noda, "High-heat-flux-exposure-experiments of a tungsten-test-limiter at TEXTOR-94," *Journal of Nuclear Materials,* Vols. 258-263, pp. 853-857, 1998.

[56] M. Wada, T. Ohgo, A. Pospieszczyk, A. Huber, G. Sergienko, T. Tanabe, W. Biel, K. Kondo, K. Ohya, V. Philipps, G. Bertschinger, J. Rapp, B. Schweer and N. Noda, "Local emission and core concentration of tungsten in TEXTOR-94 plasmas operated with tungsten test and poloidal limiters," *Journal of Nuclear Materials,* Vols. 290-293, pp. 768-772, 2001.

[57] A. Pospieszczyk, B. Schweer, V. Philipps, A. Huber, G. Sergienko, U. Samm, H. Reimer, M. Freisinger, M. Rubel, A. Herrmann, S. Kötterl, M. Laux, H. Renner and H. Bolt, "B4C-limiter experiments at TEXTOR," *Journal of Nuclear Materials,* Vols. 313-316, pp. 223-229, 2003.

[58] M. Laux, W. Schneider, P. Wienhold, B. Jüttner, A. Huber, M. Balden, J. Linke, H. Kostial, M. Mayer, M. Rubel, A. Herrmann, A. Pospieszczyk, S. Jachmich, B. Schweer, D. Hildebrandt and H.

Bolt, "Arcing at B4C-covered limiters exposed to a SOL-plasma," *Journal of Nuclear Materials,* Vols. 313-316, pp. 62-66, 2003.

[59] R. Doerner, B. E. Mills, E. Wallura, D. S. Walsh, G. Chevalier, R. W. Conn, K. H. Dippel, B. L. Doyle, H. G. Esser, K. H. Finken, D. Gray, Y. Hirooka, K. Koizlik, A. Miyahara, R. A. Moyer, J. G. Watkins and J. Winter, "Materials analysis of TEXTOR limiter tiles," *Journal of Nuclear Materials,* vol. 176&177, pp. 954-961, 1990.

[60] G. v. Oost, R. v. Nieuwenhoven, R. Koch, A. Messiaen, P. Vandenplas, R. Weynants, K. Dippel, K. Finken, Y. Lie, A. Pospieszczyk, U. Samm, B. Schweer, R. Conn, W. Corbett, D. Goebel and R. Moyer, "ICRF/Edge physics research on TEXTOR," *Fusion Engineering and Design,* vol. 12, pp. 149-170, 1990.

[61] E. Fortuna, M. J. Rubel, V. Philipps, K. J. Kurzydlowski, P. Mertens, M. Miskiewicz, M. Pisarek, G. v. Oost and W. Zielinski, "Properties of co-deposited layers on graphite high heat flux components at the TEXTOR tokamak," *Journal of Nuclear Materials,* Vols. 367-370, pp. 1507-1511, 2007.

[62] Y. Ueda, M. Fukumoto, J. Watanabe, Y. Ohtsuka, T. Arai, N. Asakura, Y. Nobuta, M. Sato, T. Nakano, J. Yagyu, K. Ochiai, K. Takakura, T. Tanabe and J.-6. Team, "Localized tungsten deposition in the divertor region in JT-60U," *Nuclear Fusion,* vol. 49, p. 065027, 2009.

[63] V. Rozhansky, E. Kaveeva, S. Voskoboynikov, A. Bekheit, D. Coster, X. Bonnin and R. Schneider, "Impact of ExB drifts on the distribution of impurities in the Tokamak plasma edge," *Journal of Nuclear Materials,* Vols. 313-316, pp. 1141-1149, 2003.

[64] B. Mills, D. Buchenauer, A. Pontau and M. Ulrickson, "Characterization of deposition and erosion of the TFTR bumper limiter and wall," *Journal of Nuclear Materials,* Vols. 162-164, pp. 343-349, 1989.

[65] R. McGrath and J. Brooks, "Transport of sputtered impuirities in the vicinity of the TFTR inner bumper limiter," *Journal of Nuclear Materials,* Vols. 162-164, pp. 350-355, 1989.

[66] K. Krieger, A. Geier, X. Gong, H. Maier, R. Neu, V. Rohde and A. U. Team, "Erosion and migration of tungsten employed at the main chamber first wall of ASDEX Upgrade," *Journal of Nuclear Materials,* Vols. 327-332, pp. 313-316, 2003.

[67] P. Petersson, A. Hakola, J. Likonen, M. Mayer, J. Miettunen, R. Neu, V. Rohde, M. Rubel and A.-U. Team, "Injection of nitrogen-15 tracer into ASDEX-Upgrade: New technique in material migration studies," *Journal of Nuclear Materials,* vol. 438, pp. 616-619, 2013.

[68] R. Doerner, M. Baldwin, G. D. Temmerman, J. Hanna, D. Nishijima, J. Roth, K. Schmid, G. Tynan and K. Umstadter, "Codeposition of deuterium with ITER materials," *Nuclear Fusion,* vol. 49, p. 035002, 2009.

[69] D. Gray, K. Dippel, K. Finken, R. Moyer, M. Ciotti, R. Conn, D. Hillis, P. Mioduszewski, D. Reiter, S. Sengoku, G. Wolf, T. team and N. Team, "Particle exhaust during neutral injection by the ALT-

II pump limiter in TEXTOR," *Journal of Nuclear Materials,* Vols. 176-177, pp. 810-815, 1990.

[70] J. Winter, "Wall conditioning of fusion devices by reactive plasmas," *Journal of Nuclear Materials,* vol. 161, pp. 265-330, 1989.

[71] J. v. Seggern, H. Peters, H. Esser, P. Wienhold and J. Winter, "Composition of a-C/B:H films and of redeposited layers in the boronized TEXTOR tokamak," *Vacuum,* vol. 41, no. 4-6, pp. 1486-1488, 1990.

[72] W. Wampler, B. Doyle, S. Lee, A. Pontau, B. Mills, R. Causey, D. Buchenauer, H. Dylla, M. Ulrickson and P. LaMarche, "Deposition of carbon, deuterium, and metals on the wall and limiters of the Tokamak Fusion Test Reactor," *Journal of Vacuum Science & Technology A. Vacum, Surfaces, and Films,* vol. 6, pp. 2111-2115, 1988.

[73] Y. Hirohata, T. Tanabe, T. Shibahara, M. Oyaidzu, K. Sugiyama, Y. Oya, A. Yoshikawa, Y. Onishi, T. Arai, M. Masaki, Y. Ishimoto, K. Okuno and N.Miya, "Distribution of hydrogen isotopes retained in the divertor tiles used in JT-60U," *Journal of Nuclear Materials,* Vols. 367-370, pp. 1260-1265, 2007.

[74] B. Pégourié and e. al., "Deuterium inventory in Tore Supra: Coupled carbon-deuterium balance," *Journal of Nuclear Materials,* vol. 438, pp. 120-125, 2013.

[75] A. Kirschner, V. Philipps, J. Winter and U. Kögler, "Simulation of the plasma-wall interaction in a tokamak with the Monte Carlo code ERO-TEXTOR," *Nuclear Fusion,* vol. 40, no. 5, pp. 989-1001, 2000.

[76] A. Kirschner, A. Kreter, P. Wienhold, A. Weckmann, A. Pospieszczyk, R. Ding, D. Borodin, S. Brezinsek, G. Sergienko, M. Rubel, C. Linsmeier and T. Team, "Modelling of deposition and erosion of injected WF6 and MoF6 in TEXTOR," *Nuclear Materials and Energy,* vol. 12, pp. 564-568, 2017.

[77] M. Taniguchi, K. Sato, K. Ezato, K. Yokoyama, M. Dairaku and M. Akiba, "Sputtering of carbon-tungsten mixed materials by low energy deuterium," *Journal of Nuclear Materials,* Vols. 313-316, pp. 360-363, 2003.

[78] S. Droste, A. Kirschner, D. Borodin, A. Kreter, S. Brezinsek, V. Philipps, U. Samm, O. Schmitz and T. team, "Modelling of 13CH4 injection experiments with graphite and tungsten test limiters in TEXTOR using the coupled code ERO-SDTrimSP," *Plasma Physics and Controlled Fusion,* vol. 50, 2008.

[79] A. Kirschner, A. Kreter, P. Wienhold, S. Brezinsek, J. W. Coenen, H. Esser, A. Pospieszczyk, C. Schulz, U. Breuer, D. Borodin, M. Clever, R. Ding, A. Galonska, A. Huber, A. Litnovsky, D. Matveev, K. Ohya, V. Philipps, U. Samm, O. Schmitz and B. Schweer, "Deposition and re-erosion studies by means of local impurity injection in TEXTOR," *Journal of Nuclear Materials,* vol. 415, pp. 239-245, 2011.

[80] W. Biel and T. Team, "Vacuum ultraviolet spectroscopy at TEXTOR," *Fusion Science and*

Technology, vol. 47, pp. 246-252, 2005.

[81] J. A. Heikkinen, S. K. Sipilä and T. J. H. Pättikangas, "Monte Carlo simulation of runaway electrons in a toroidal geometry," *Computer Physics Communications,* vol. 76, no. 2, pp. 215-230, 1993.

[82] A. Kreter, D. Borodin, S. Brezinsek, S. Droste, T. Hirai, A. Kirschner, A. Litnovsky, M. Mayer, V. Philipps, A. Pospieszczyk, Y. Sakawa, U. Samm, O. Schmitz, G. Sergienko, T. Tanabe, Y. Ueda, P. Wienhold and T. team, "Investigation of carbon transport by 13CH4 injection through graphite and tungsten test limiters in TEXTOR," *Plasma Physics and Controlled Fusion,* vol. 48, pp. 1401-1412, 2006.

[83] D. Moseev, F. Meo, S. Korsholm, T. Koskela, M. Albergante, O. Asunta, H. Bindslev, A. Bürger, V. Furtula, M. Y. Kantor, F. Leipold, P. Michelsen, S. Nielsen, M. Salewski, O. Schmitz, M. Stejner, E. Westerhof and T. team, "Comparison of measured and simulated fast ion velocity distributions in the TEXTOR tokamak," *Plasma Physics and Controlled Fusion,* vol. 53, p. 105004, 2011.

[84] E. Hintz and B. Schweer, "Plasma Edge Diagnostics by Atomic Beam Supported Emission Spectroscopy - Status and Perspectives," *Plasma Physics and Controlled Fusion,* vol. 37, pp. 87-101, 1995.

[85] H. Koslowski and H. Soltwisch, "Electron density and q profile measurements with the far-IR interferometer-polarimeter on the TEXTOR tokamak," *Fusion Engineering and Design,* Vols. 34-35, pp. 143-150, 1997.

[86] Special Metals Corporation, "http://www.specialmetals.com," Special Metals Corporation, August 2013. [Online]. Available: http://www.specialmetals.com/assets/smc/documents/alloys/inconel/inconel-alloy-625.pdf. [Accessed 2016].

[87] V. Philipps, "Wall conditioning on TEXTOR," *Fusion Science and Technology,* vol. 47, pp. 119-125, 2005.

[88] T. Wauters, S. Möller, A. Kreter, M. Rubel, A. G. Carrasco, K. Crombé, D. Douai, M. Freisinger, D. Ivanova, D. Kogut, R. Koslowski, A. Lyssoivan, D. Nicolai, P. Petersson, V. Philipps, M. Rack, H. Reimer, G. Sergienko and M. Vervier, "Self-consistent application of ion cyclotron wall conditioning for co-deposited layer removal and recovery of tokamak operation on TEXTOR," *Nuclear Fusion,* vol. 53, p. 123001, 2013.

[89] A. G. Carrasco, S. Möller, P. Petersson, D. Ivanova, A. Kreter, M. Rubel and T. Wauters, "Impact of ion cyclotron wall conditioning on fuel removal from plasma-facing components at TEXTOR," *Physica Scripta,* vol. T159, p. 014017, 2014.

[90] G. Anda, D. Dunai, G. Petravich, J. Sárközi, S. Zoletnik, B. Schweer, T. Baross, I. G. Kiss and B. Mészáros, "First Measurements with the re-installed accelerated Lithium beam diagnostics on

TEXTOR," in *35th EPS Conference on Plasma Physics*, Hersonissos, 2008.

[91] A. G. Carrasco, P. P. T. Wauters, A. Drenik, M. Rubel, K. Crombé, D. Douai, E. Fortuna, D. Kogut, A. Kreter, A. Lyssoivan, S. Möller, M. Pisarek and M. Vervier, "Nitrogen removal from plasma-facing components by ion cyclotron wall conditioning in TEXTOR," *Journal of Nuclear Materials,* vol. 463, pp. 688-692, 2015.

[92] S. Brezinsek, D. Borodin, J. W. Coenen, D. Kondratjew, M. Laengner, A. Pospieszczyk, U. Samm and T. team, "Quantification of tungsten sputtering at W/C twin limiters in TEXTOR with the aid of local WF6 injection," *Physica Scripta,* vol. T145, 2011.

[93] Y. M. Kim, V. Philipps, M. Rubel, E. Vietzke, A. Pospieszczyk, B. Unterberg and R. Jaspers, "Retention of neon in graphite after ion beam implantation or exposures to the scrape-off layer plasma in the TEXTOR tokamak," *Journal of Vacuum Science and Technology A,* vol. 20, pp. 138-145, 2002.

[94] P. Lindner, M. Brix, P. Mertens, A. Pospieszczyk, U. Samm, B. Schweer and B. Unterberg, "Velocity distribution of helium and neon atoms released from graphite and tungsten limiters in TEXTOR," *Journal of Nuclear Materials,* vol. 348, pp. 283-293, 2006.

[95] P. Wienhold, V. Philipps, A. Kirschner, A. Huber, J. v. Seggern, H. Esser, D. Hildebrandt, M. Mayer, M. Rubel and W. Schneider, "Short and long range transport of materials eroded from wall components in fusion devices," *Journal of Nuclear Materials,* Vols. 313-316, pp. 311-320, 2003.

[96] G. Bertschinger, T.-9. T. W. Biel, O. Herzog, J. Weinheimer, H.-J. Kunze and M. Bitter, "X-Ray Spectroscopy at the TEXTOR-94 Tokamak," *Physica Scripta,* vol. T83, pp. 132-141, 1999.

[97] O. Marchuk, M. Tokar, G. Bertschinger, A. Urnov, H.-J. Kunze, D. Pilipenko, X. Loozen, D. Kalupin, D. Reiter, A. Pospieszczyk, W. Biel, M. Goto and F. Goryaev, "Comparison of impurity transport model with measurements of He-like spectra of argon at the tokamak TEXTOR," *Plasma Physics and Controlled Fusion,* vol. 48, pp. 1633-1646, 2006.

[98] A. Greiche, Y. Liang, O. Marchuk, G. Bertschinger, W. Biel, R. Burhenn, R. Dux, H. Koslowski, A. Krämer-Flecken, K. Löwenbrück, O. Schmitz, G. Spakman, R. Wolf and T. team, "Transport of argon and iron during a resonant magnetic perturbation at TEXTOR-DED," *Plasma Physics and Controlled Fusion,* vol. 51, p. 032001, 2009.

[99] K. Tsuzuki, T. Hirai, Y. Kusama, V. Phillips, A. Pospieszczyk, M. Sakamoto, Y. Sakawa, G. Sergienko, B. Schweer, T. Tanabe and Y. Ueda, "Exposure of reduced activation ferretic steel F82H to TEXTOR plasma," *Fusion Engineering and Design,* vol. 81, pp. 925-929, 2006.

[100] A. Kreter, S. Brezinsek, T. Hirai, A. Kirschner, K. Krieger, M. Mayer, V. Philipps, A. Pspieszczyk, U. Samm, O. Schmitz, B. Schweer, G. Sergienko, K. Sugiyama, T. Tanabe, Y. Ueda, P. Wienhold and T. team, "Effect of surface roughness and substrate material on carbon erosion and deposition in the TEXTOR tokamak," *Plasma Physics and Controlled Fusion,* vol. 50, no. 9, 2008.

[101] W. Kohlhaas, J. A. Koski and T. Uchikawa, "Engineering design concept of the Advanced Limiter TEST-II," *Fusion Engineering and Design,* vol. 13, pp. 261-265, 1990.

[102] J. Winter, "Wall conditioning in fusion devices and its influence on plasma performance," *Plasma Physics and Controlled Fusion,* vol. 38, pp. 1503-1542, 1996.

[103] J. Coad, M. Rubel and C. Wu, "The amount and distribution of deuterium retained in the jet divertor after the C and Be phases in 1994-1995," *Journal of Nuclear Materials,* Vols. 241-243, pp. 408-413, 1997.